SYNTHESIS AND CHARACTERIZATION OF BIMETALLIC NANOCATALYSTS FOR FISHER-TROPSCH SYNTHESIS

by

Furkan Işık

B.S., Chemistry, Boğaziçi University, 2016

Submitted to the Institute for Graduate Studies in
Science and Engineering in partial fulfillment of
the requirements for the degree of
Master of Science

Graduate Program in Chemistry
Boğaziçi University

2018

SYNTHESIS AND CHARACTERIZATION OF BIMETALLIC NANOCATALYSTS FOR FISCHER-TROPSCH SYNTHESIS

APPROVED BY:

Assist. Prof. Oktay DEMİRCAN (Thesis Supervisor)	……
Assist. Prof. Aligül BÜYÜKAKSOY	……
Prof. Amitav SANYAL	……

DATE OF APPROVAL: 29.08.2019

Dedicated to my family

ACKNOWLEDGEMENTS

In principle this thesis is an individual work, there are so many people that has a critical role in the process. Since I am not good with words my sentences of gratitude for each mentioned person is going to be short, but I would like to emphasize that it has nothing to do with their value at all, it is just an inability of mine to express my feelings. I apologize for that, in advance.

First of all, I would like to thank my thesis supervisor Assist. Prof. Oktay Demircan for his encouragement and support. I am grateful for the freedom he provided in my research.

I would like to express my gratitude to Prof. Amitav Sanyal for his valuable advices and letting me use the facilities in his lab.

As for almost every single academic task, this was a stressful marathon and I would like to thank my lab mates Ayşenur Eslem Kısa and Benazir Fazlıoğlu for making the process bearable.

I am also grateful to Yavuz Öz, for his advices and helps for my research.

I owe a dept of gratitude to Bektaş Karakelle, Deputy Director of Çekmece Nuclear Research and Training Center (TAEA), for letting me use the reseach facilities in TAEA; and also, Abdulhamit Saraç, Özgür Duygulu and Cem Berk for TEM and SEM characterizations in TUBİTAK MAM.

Finally, I would like to add a special thanks to my dear family members, who were supportive throughout my master life with ups and especially downs.

ABSTRACT

SYNTHESIS AND CHARACTERIZATION OF BIMETALLIC NANOCATALYSTS FOR FISHER-TROPSCH SYNTHESIS

Fischer-Tropsch Synthesis (FTS) enables conversion of syngas obtained from a wide variety of carbon feedstocks, to certain liquid fuels and chemicals. This synthesis is a heterogeneously catalyzed process, where cobalt (Co) and iron (Fe) are the main catalyst materials that are being used commercially. FTS is a combination of carbon monoxide (CO) reduction and a polymerization reaction. This nature of FTS causes the product spectrum to contain a wide variety of hydrocarbons and this requires post-processing to isolate desired products. As for all catalyst, FTS catalyst should have high activity, selectivity, and long operation life. To address these issues, nanocrystals with different composition, size, and geometry are being implemented as catalyst materials. The mentioned parameters play key roles in determining the type of surface sites, distribution of them and electronic structure of catalytically active atoms. This study focuses on creating a library of bimetallic core-shell nanoparticles with catalytically active shells (e.g. Fe, Co, and $Fe_{0.5}Co_{0.5}$) for FTS and tin (Sn) core. There are reasons for choosing tin as a core material: (i) tin can have oxidation states varying from +4 to -4. This property can change the behavior of shell material towards FTS since this process involves reversible oxidation steps of the catalyst. (ii) Through charge transfers between the tin core and the metal in the shell, the electronic structure of the surface would be modified. (iii) Since tin has relatively large lattice constant compared to Co and Fe, it will induce strain on the surface atoms and that would change the energetics of the surface. For the synthesis, a modified polyol process is implemented due to its simplicity, versatility, and relatively low cost. The characterizations of the synthesized nanoparticles were performed by High-Resolution Transmission Electron Microscopy (HRTEM), X-Ray Diffraction spectroscopy (XRD) and X-Ray Photoelectron Spectroscopy (XPS). At the end of the study, it is concluded that the desired nanoparticles can be synthesized by the employed synthesis method.

ÖZET

FISCHER-TROPSCH SENTEZİ İÇİN BİMETALİK NANO KATALİZÖRLERİN SENTEZ VE KARAKTERİZASYONLARI

Fischer-Tropsch sentezi (FTS) karbon esaslı herhangi karbon esaslı maddeden üretilen sentez gazının sıvı yakıta ve çeşitli kimyasallara dönüştürülmesini sağlayan bir teknolojidir. Bu sentez genellikle kobalt (Co) ve demir (Fe) esaslı heterojen katalizörler sayesinde gerçekleştirilmektedir. FTS reaksiyonları hem kabon monoksit (CO) hidrojenleştirme hem de polimerleşme tepkimeleridir. Bu sebeple FTS sonucundaki ürünler farklı uzunlukta hidrokarbonlardan oluşmaktadır ve istenilen ürünün elde edilmesi için ek süreçlere ihtiyaç duyulmaktadır. Her katalitik sistemde olduğu gibi, FTS katalizörlerinde de yüksek aktivite, seçicilik ve uzun ömür şartları aranmaktadır. Bu kriterlerin sağlanabilmesi için katalizör malzemesi olarak farklı içerikli, çeşitli şekil ve büyüklüklerde nano parçacıklar kullanılmaktadır. Bu sayılan özelliklerin değiştirilmesiyle katalitik olarak aktif olan yüzey yapılarının çeşitliliği ve oranı ayarlanabilmekte ve yüzey atomlarının elektronik yapıları ile oynanabilmektedir. Bu çalışma FTS için iki farklı metalden oluşan çekirdek-kabuk yapısında nano parçacıklardan oluşan bir kütüphane yaratmaktır. Çekirdekte olması planlanan kalay (Sn) elementinin seçilmesindeki etmenler şu şekilde sıralanabilir: (i) kalay, +4'ten -4'e kadar farklı oksidasyon numarasına sahip olabildiği için FTS'de meydana gelen tersinir oksitlenme tepkimelerinde rol alabilmektedir. (ii) Metaller arası yük transferi sayesinde yüzeydeki metalin elektronik yapısını değiştirebilmektedir. (iii) Yüksek kristal sabiti nedeniyle yüzey atomlarının diziliminde değişikliklere yol açabilmektedir. Bu parçacıkların sentezinde, basitliği, kullanım esnekliği ve düşük maddi gereksinimi sebeplerinden dolayı bir poliyol sentez yöntemi kullanılmıştır. Sentezlenen nano yapıların karakterizasyonları yüksek çözünürlüklü geçirimli electron mikroskobu (HRTEM), X-Işını Kırınımı (XRD) ve X-Işını Foto elektron Spektroskopi (XPS) yöntemleriyle yapılmıştır. Çalışmanın sonunda seçilen sentez yöntemiyle istenilen nano parçacıkların sentezlenebildiği görülmüştür.

TABLE OF CONTENTS

ACKNOWLEDGEMENTS.....iv
ABSTRACT.....v
ÖZET.....vi
LIST OF FIGURES.....ix
LIST OF TABLES.....xiii
LIST OF SYMBOLS.....xiv
LIST OF ACRONYMS/ABBREVIATIONS.....xv
1. INTRODUCTION.....1
1.1. Heterogeneous Catalysis.....1
1.1.1. Catalytic Cycle.....1
1.1.2. Metals.....8
1.1.2.1. Structure Sensitivity.....9
1.1.2.2. Support Effect.....11
1.2. Fischer-Tropsch Synthesis.....12
1.2.1. Iron-Based FTS.....18
1.2.2. Cobalt-Based FTS.....25
1.2.3. Mechanism and Kinetics.....32
1.3. Bimetallic Nano-Structures.....36
1.3.1. The Architecture of Bimetallic Nanocrystals.....37
1.3.1.1. Alloys and Bimetallic Compounds.....37
1.3.1.2. Core-Shell Nanoparticles.....38
1.3.1.3. Hollow Structures.....38
1.3.1.4. Core-Frame Structures.....38
1.3.1.5. Dendritic and Heterostructured Nanocrystals.....39
1.3.2. Synthetic Approaches.....39
1.3.2.1. Co-reduction.....39
1.3.2.2 Thermal Decomposition.....40
1.3.2.3. Seed-Mediated Growth.....41
1.3.2.4. Galvanic Replacement.....42
1.3.3. Catalytic Properties of Bimetallic Nanoparticles.....43

1.4. Aim of the Study.....44
2. EXPERIMENTAL.....46
2.1. Reagents.....46
2.2. Synthesis of Bimetallic Nanostructures.....46
2.2.1. Synthesis of Tin Seed Nanoparticles.....46
2.2.2. Synthesis of Sn@Co Nanoparticles.....47
2.2.3. Synthesis of Sn@Fe Nanoparticles.....48
2.2.4. Synthesis of $Sn@Co_{0.5}Fe_{0.5}$ Nanoparticles.....48
2.3. Characterization of Nanoparticles.....49
2.3.1. Transmission Electron Microscopy (TEM).....49
2.3.2. X-Ray Diffraction (XRD).....49
2.3.3. X-Ray Photoelectron Spectroscopy (XPS).....50
3. RESULTS AND DISCUSSION.....51
3.1. Transmission Electron Microscopy (TEM) Results.....51
3.2. X-Ray Photoelectron Spectroscopy (XPS) and X-Ray Diffraction (XRD) Results..58
4. CONCLUSIONS.....66
5. FUTURE WORK.....67
REFERENCES.....68

LIST OF FIGURES

Figure1.1. Catalytic cycle.....2

Figure 1.2. Adsorption sites of a metal: hydrogen atoms in fourfold hollow or bridged sites on an bcc (100) surface; CO in the top, bridge or threefold hollow sites on an fcc (111) surface.....3

Figure 1.3. Potential energy diagram for the interactions of a molecule A_2 and a metal surface.....4

Figure 1.4. Band structure and their density of states of a d-metal.....5

Figure 1.5. Atomic adsorption on d-metals. A metal with half-filled d-orbital on the left, and a metal with more than half-filled d-orbital on the right.....5

Figure 1.6. Molecular adsorption of a diatomic molecule on a d-metal.....6

Figure 1.7. Molecular orbital diagrams for the dissociative adsorption.....7

Figure 1.8. Figure 1.8. Potential energy diagram of a molecule and its dissociated atoms on two different surfaces (left). The relationship between the activation energy and the adsorption energies (right).....8

Figure 1.9. Trends in the periodic table towards dissociative adsorption.....9

Figure 1.10. Three types of surface sensitivity, type (1) reactions are surface insensitive type (2) reactions processes show lower activity as the particle size of the catalyst increases and type (3) reactions have an optimum particle size for the optimum reactivity.....10

Figure 1.11. The change in the weight of different sites and mean coordination Number as a function of the size.....10

Figure 1.12. Transition states of CO dissociation (on the left), and methane dissociation (on the right) on a stepped surface.....11

Figure 1.13. Product spectrum of FTS with varying chain growth probabilities.....14

Figure 1.14. FTS reactor types, slurry bubble reactors (top-left), multitubuluar fixed bed reactors (top-right), circulating fluid bed reactors (bottom-left) and fixed fluid bed reactos (bottom-right).....17

Figure 1.15. Process diagram of catalyst preparation by the fusion method.....19

Figure 1.16. Process diagram of catalyst preparation by the precipitation method.....20

Figure 1.17 Anderson-Schulz-Flory distribution of LTFT and HTFT synthesis with iron catalysts.....23

Figure 1.18. Deactivation mechanism of Ruhrchemie iron catalyst under LTFT conditions.....24

Figure 1.19. Composition of cobalt FTS catalyst prepared for the slurry phase Reactor.....26

Figure 1.20. TOF-size relationship at FTS.....31

Figure 1.21. Energy profile obtained by DFT calculations for methane formation reactions on various metal surfaces.....36

Figure 1.22. Possible architectures of bimetallic nanoparticles.....37

Figure 1.23. LaMer Diagram for the generation of nanoparticles.....41

Figure 1.24. Growth modes in the seed-mediated growth process.....42

Figure 3.1. TEM image of as-prepared Sn nanoparticles.....52

Figure 3.2. Size histogram of Sn nanoparticles. Numbers over the bars indicate the number of NPs with same size.....52

Figure 3.3. Lattice fringe of Sn nanoparticle.....53

Figure 3.4. TEM image of Sn@Fe core-shell nanoparticles.....53

Figure 3.5. Size histogram of Sn-Fe bimetallic nanoparticles. Numbers over the bars indicate the number of NPs with same size.....55

Figure 3.6. TEM image of Sn@Co core-shell nanoparticles.....56

Figure 3.7. Size histogram of Sn-Co bimetallic nanoparticles. Numbers over the bars indicate the number of NPs with same size.....56

Figure 3.8. TEM image of Sn@CoFe core-shell nanoparticles.....57

Figure 3.9. Size histogram of Sn-CoFe bimetallic nanoparticles. Numbers over the bars indicate the number of NPs with same size.....57

Figure 3.10. XPS survey analysis of as-prepared Sn nanoparticles.....58

Figure 3.11. The Sn3d core level XPS spectra of as-prepared Sn nanoparticles.....59

Figure 3.12. XRD results of all nanoparticles.....59

Figure 3.13. XPS survey analysis of Sn-Co nanoparticles.....60

Figure 3.14. The Sn3d core level XPS spectra of Sn-Co nanoparticles.....61

Figure 3.15. XPS survey analysis of Sn-Fe nanoparticles.....62

Figure 3.16. The Sn3d core level XPS spectra of Sn-Fe nanoparticles.....62

Figure 3.17. The Fe2p core level XPS spectra of Sn-Fe nanoparticles.....63

Figure 3.18. XPS survey analysis of Sn-CoFe nanoparticles.....63

Figure 3.19. The Sn3d core level XPS spectra of Sn-CoFe nanoparticles.....64

Figure 3.20. The Co2p core level XPS spectra of Sn-CoFe nanoparticles.....65

Figure 3.21. The Fe2p core level XPS spectra of Sn-CoFe nanoparticles.....65

LIST OF TABLES

Table 1.1. Most common reaction mechanisms that are proposed for FTS.....33

Table 3.1. Chemicals and materials used in this study.....46

LIST OF SYMBOLS

E_{act}	Activation Energy
E_F	Fermi Level
α	Chain Growth Probability
α_{BEP}	Brønsted-Evans-Polanyi Parameter
ρ	Partial Pressure
ΔE_{act}^{dis}	Activation Energy for Dissociation
ΔH	Change in Enthalpy
ΔH_{ads}^{atom}	Change in Enthalpy of Atomic Adsorption
ΔH_{ads}^{mol}	Change in Enthalpy of Molecular Adsorption
ΔH_{ads}^{phys}	Change in Enthalpy of Molecular Physisorption

LIST OF ACRONYMS/ABBREVIATIONS

ASF	Anderson-Schulz-Flory
ATR	Autothermal Reforming
BEP	Brønsted-Evans-Polanyi
BTL	Biomass to Liquid
CPOX	Catalytic Partial Oxidation
CTL	Coal to liquid
DFT	Density Functional Theory
fcc	Face Centered Cubic
FT	Fischer-Tropsch
FTS	Fischer-Tropsch Synthesis
GDP	Gross Domestic Product
GTL	Gas to liquid
hcp	Hexagona Closed Pack
HTFT	High-Temperature Fischer-Tropsch
LTFT	Low-Temperature Fischer-Tropsch
ML	Mono Layer
NP	Nano Particle
OA	Oleic Acid
OLA	Oleylamine
PEG	Polyethylene Glycol
POX	Partial Oxidation
PVP	Polyvinylpyrrolidone
TOF	Turnover Frequency
UHV	Ultra High Vacuum
WGS	Water-Gas-Shift
XRD	X-ray Diffraction
XTL	Any Carbon Feedstock to Liquid

1. INTRODUCTION

1.1. Heterogeneous Catalysis

Catalysts are the materials that enable the reactions to occur at lower activation energies and higher rates. Heterogeneous catalysis is the sub-discipline of the field catalysis, where the catalyst is in the solid state. This field is at the heart of the chemical industry for years. Around 90% of the industry that covers the 30-40% of world GDP, relies on heterogeneous catalysis.[1] Since this is a surface phenomenon, size and morphology, besides the composition of the material, plays a crucial role in the catalyst performance. As a common example, gold is known to be inert in the bulk form, whereas it becomes an active metal towards oxidation of carbon monoxide (CO) when the size reaches down to the nanometer scale. The science of heterogeneous catalysis exploits this fundamental of size-effect, besides the casual increase in surface area, which is always aimed to be maximized.

As the size of the particles becomes smaller, they become more prone to sintering and this causes loss of activity. Support materials are being implemented to stabilize catalyst particles. Most common support materials are alumina, silica, titania, zirconia, graphite. These materials should be chemically, mechanically and thermally stable in the reaction conditions. The strength of interaction between catalyst and support should be moderate, which is enough to stabilize the catalyst and not too strong to diminish the activity of the catalyst. Sometimes support also takes part in a step of the reaction, such systems are named as bifunctional catalysts. The physical properties of support materials (size, shape, pore size, volume, surface area, heat capacity, conductivity and melting point) have also a great influence on catalyst performance.

1.1.1. Catalytic Cycle

All heterogeneous processes follow the listed fundamental steps as seen in Figure 1.1:

(i) Transport of the reactants to the active site.
(ii) Adsorption of the reactants.

(iii) Surface reaction.

(iv) Desorption of the products.

(v) Transport of the products from active site [1].

The first step of the catalytic cycle is the adsorption of the reactants to the catalyst surface. This step falls into two occurrences: physisorption and chemisorption. In the physisorption, the interaction between the reactant and surface is mainly due to van der Waals forces, while it is chemical bonds in the case of chemisorption. The event of adsorption occurs to reduce surface free energy.

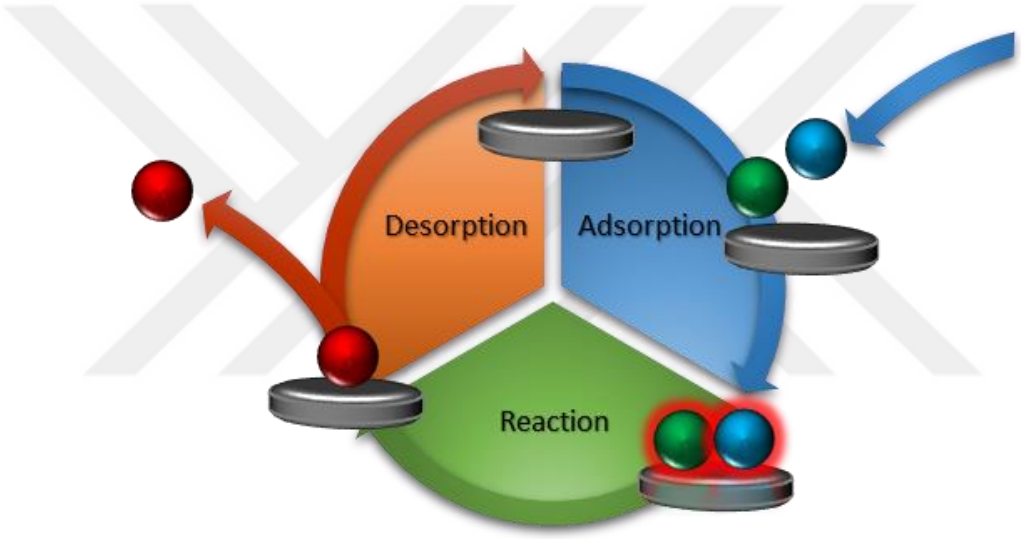


Figure 1.1. Catalytic cycle.

The short-range repulsion between the electrons of the molecule and the surface and the long-range attractions due to van der Waals forces present in the case of physisorption. It is the effective interactions between the surface and inert species such as N_2. Since these interactions also present between the molecules, there occur lateral orderings of molecules on the surface. That is why N_2 adsorption is used to determine the surface areas of the materials [1].

Since the interaction is weak (<30 kJ mol^{-1}) in physisorption, the properties of the adsorbent are not altered. But in the case of chemisorption, since new bonds are formed, the adsorbent becomes activated since new bonds change the distribution of electrons from their original states. Unlike to physisorption, chemisorption is selective to certain sites on

surfaces. The binding can occur between the adsorbent and a single atom of surface or multiple of them, which is defined by the aim of energy minimization. This feature is very important at determining of particle size, since the weight of certain sites differs as the size varies, so for good performance, a catalyst size with the highest weight of active site for that particular reactant should be optimized. For example, hydrogen atoms prefer fourfold or threefold hollow sites or bridged sites of two atoms (seen in Figure 1.2). As the coordination number decreases, so does the adsorption energy. And hydrogen atom is not stable on one atom sites.

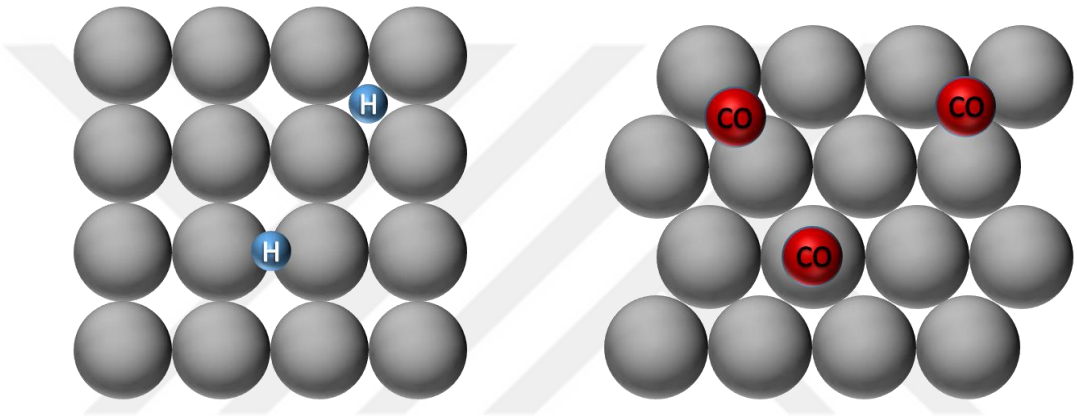


Figure 1.2. Adsorption sites of a metal: hydrogen atoms in fourfold hollow or bridged sites on an bcc (100) surface; CO in the top, bridge or threefold hollow sites on an fcc (111) surface. Reprinted from [1] with permission from John Wiley and Sons.

In a catalytic system, the reactant molecule first gets physisorbed, where the van der Waals interactions are dominant. As the molecule gets closer to the surface, new bonds between the molecule and surface are formed and it becomes chemisorbed. Since this means redistribution of electrons within the molecule, the bonds between the atoms of the reactant will weaken naturally. So, the bonds become more vulnerable for dissociation. That is how catalyst lowers the activation energy for the reactions (seen in Figure 1.3).

To understand the concept of bonding of adsorbates and metals, one should discuss it from the molecular orbital point of view. As a general knowledge, the overlap of atomic orbitals causes the formation of molecular orbitals seen in Figure 1.4. The stronger is the overlap, the greater becomes the splitting between the bonding and the antibonding orbitals of the molecule. Besides as the number of atoms in the system increases atomic orbitals

generate band structures. Since d-orbitals are strictly localized, their overlap is relatively small. This causes weak splitting and formation of narrow d-band as a consequence. Whereas s-orbitals are highly delocalized around the metal atoms, so they have strong overlap, strong splitting, and wide s-band. The lower half of the entire band is formed by bonding orbitals, where the orbitals at upper half are antibonding [2]. That is why the metals with half-filled d-orbitals have strong atomic interactions and higher melting points. When an atom is adsorbed on the metal surface, there will occur molecular orbitals between that atom and d-orbitals of metal seen in Figure 1.5. Since the electron of that atom has interactions with a bunch of d-orbitals, these new bonding, and antibonding orbitals will be broadened [3]. In any case, the orbitals below the Fermi level of the metal will be filled.

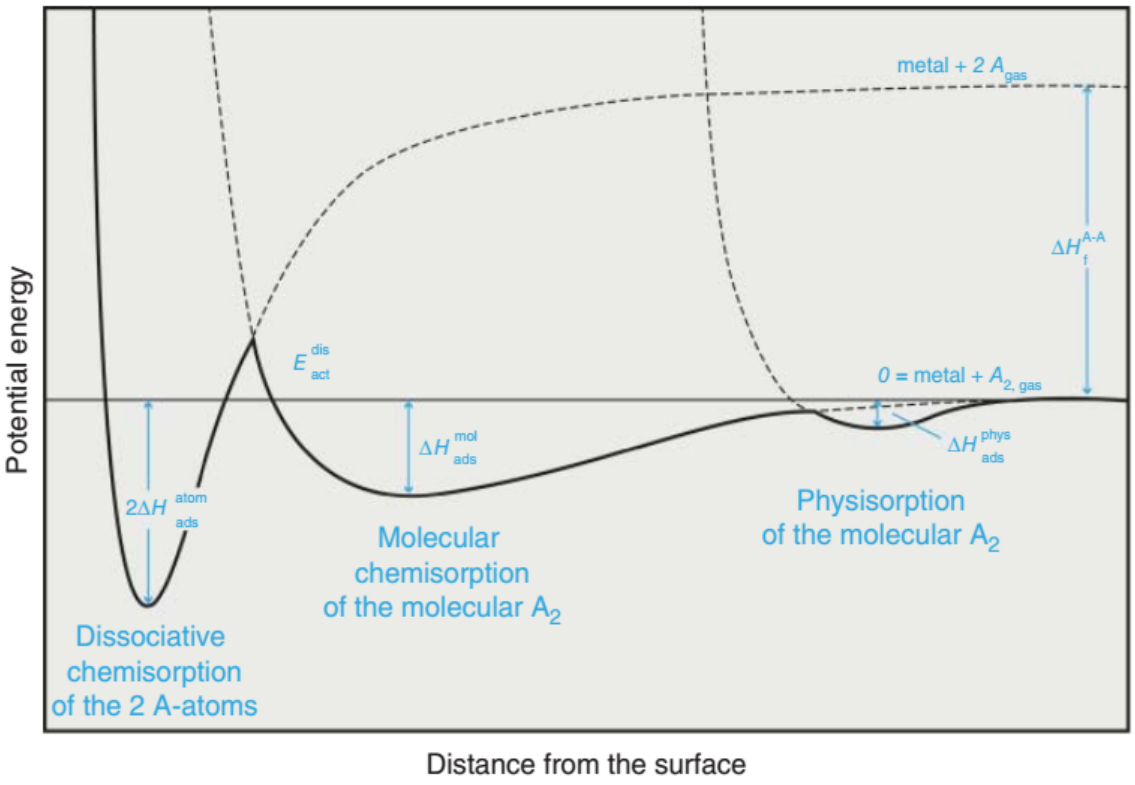


Figure 1.3. Potential energy diagram for the interactions of a molecule A_2 and a metal surface. Reprinted from [1] with permission from John Wiley and Sons.

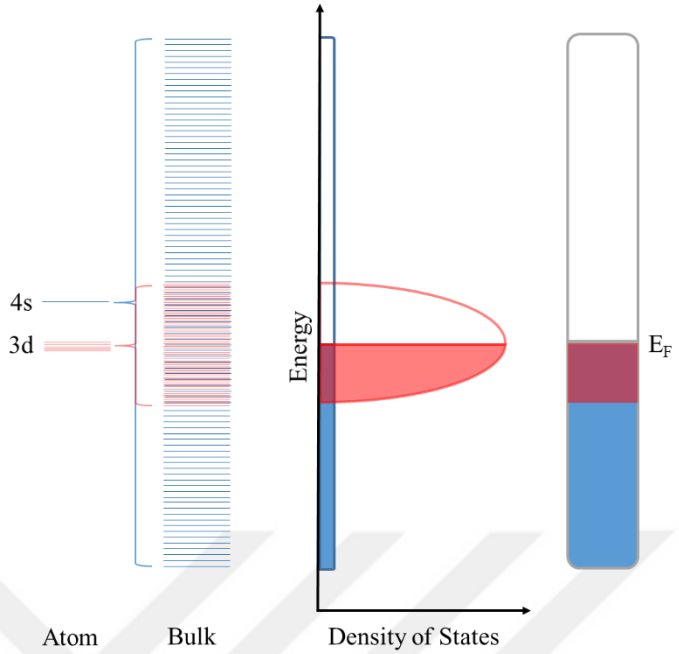


Figure 1.4. Band structure and their density of states of a d-metal. Reprinted from [1] with permission from John Wiley and Sons.

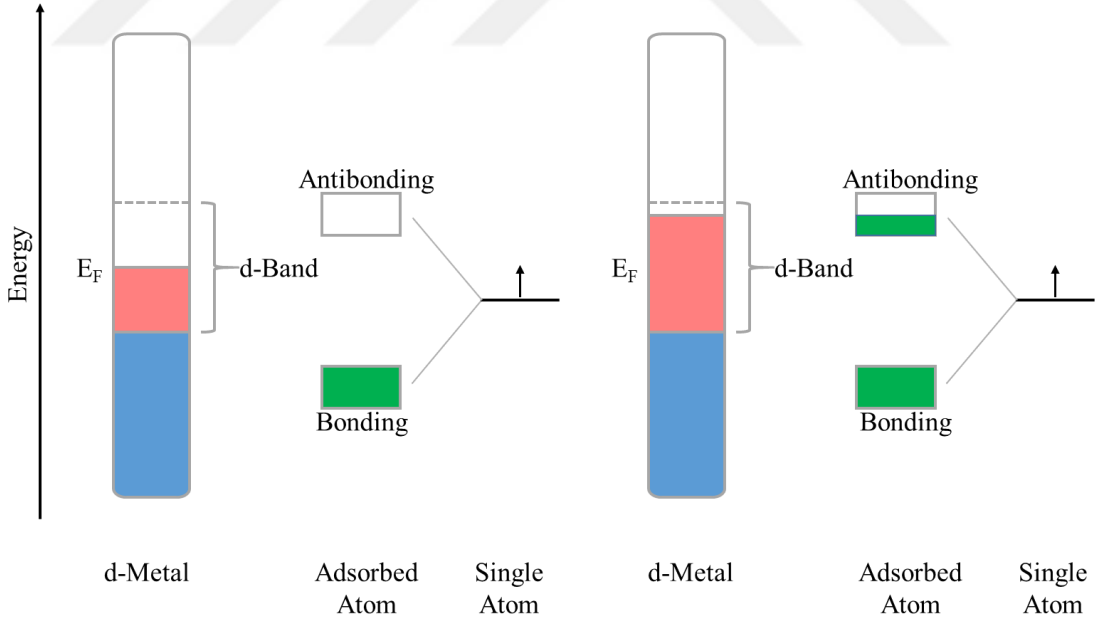


Figure 1.5. Atomic adsorption on d-metals. A metal with half-filled d-orbital on the left, and a metal with more than half-filled d-orbital on the right. Reprinted from [1] with permission from John Wiley and Sons.

In case of molecular adsorption, bonding and antibonding orbitals of the molecule will form broadened bonding and antibonding orbitals with the d-band of the metal seen in Figure 1.5. First, bonding orbitals of the molecule will form, broadened bonding and antibonding orbitals and the energy levels below the Fermi level of the metal will be filled. Since some part of the antibonding orbital in Figure 1.6 is filled, the bond strength is moderate.

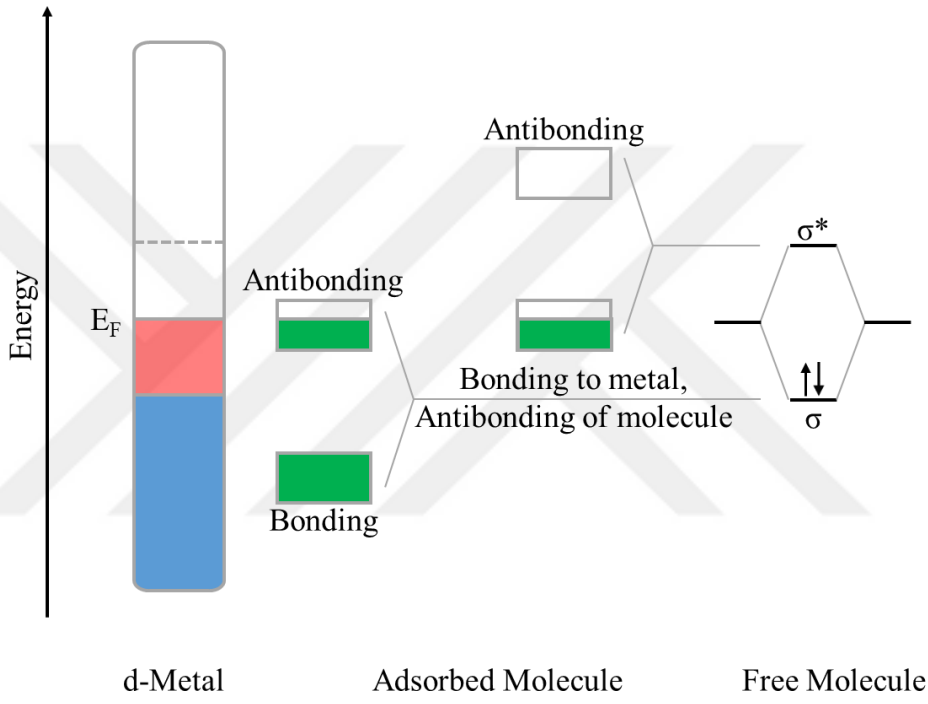


Figure 1.6. Molecular adsorption of a diatomic molecule on a d-metal. Reprinted from [1] with permission from John Wiley and Sons.

Secondly antibonding orbital of the molecule do the same with the metal and again the levels below the Fermi level will be filled displayed in Figure 1.7. Since some bonding part of these newly formed chemisorption orbitals is filled, the bond between the atoms of the molecule will weaken while the interaction of it with metal gets stronger. And this happening facilitates the dissociation of molecules on catalysts. Finally, the dissociated atoms form bonds with the surface.

The driving force of catalytic processes is the greater bond strength of the dissociated atoms to the surface, compared to the adsorption energy of the molecule. For this event to happen the adsorption energy of the molecule must be higher than the activation energy of

dissociation, otherwise, the molecule desorbs without dissociation. The energy level of the transition state is determined by the intersection of potential energies of the molecule and dissociated atoms.

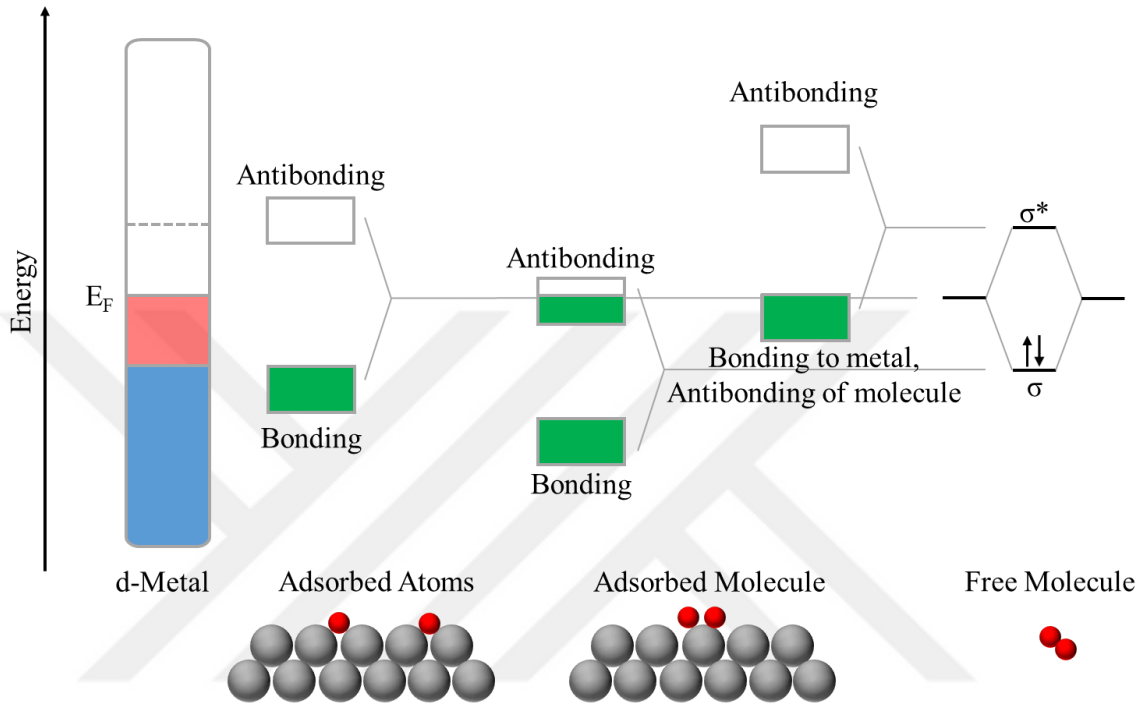


Figure 1.7. Molecular orbital diagrams for the dissociative adsorption. Reprinted from [1] with permission from John Wiley and Sons.

Generally, the difference of adsorption energies of molecules on different metals is negligible when compared to the difference of adsorption energies of dissociated atoms on different surfaces. So, one can claim that catalytic processes are governed by the adsorption energies of the generated atoms, as it increases the activation energy of dissociation decreases shown in Figure 1.8. This event can be explained by Brønsted-Evans-Polanyi (BEP) relation [4]:

$$\delta E_{act} = \alpha_1 \delta \Delta H_{ads}^{A+B} - \alpha_2 \delta \Delta H_{ads}^{AB} = \alpha_{BEP}(\Delta H_{ads}^{A+B} - \Delta H_{ads}^{AB}) = \alpha_{BEP} \Delta H_{ads}^{A+B-AB}$$

The BEP parameter (α_{BEP}) can have the values between one and zero. When it is close to one, the reaction shows late transition state and the molecule is nearly dissociated. For association reactions, this value should be close to zero [5].

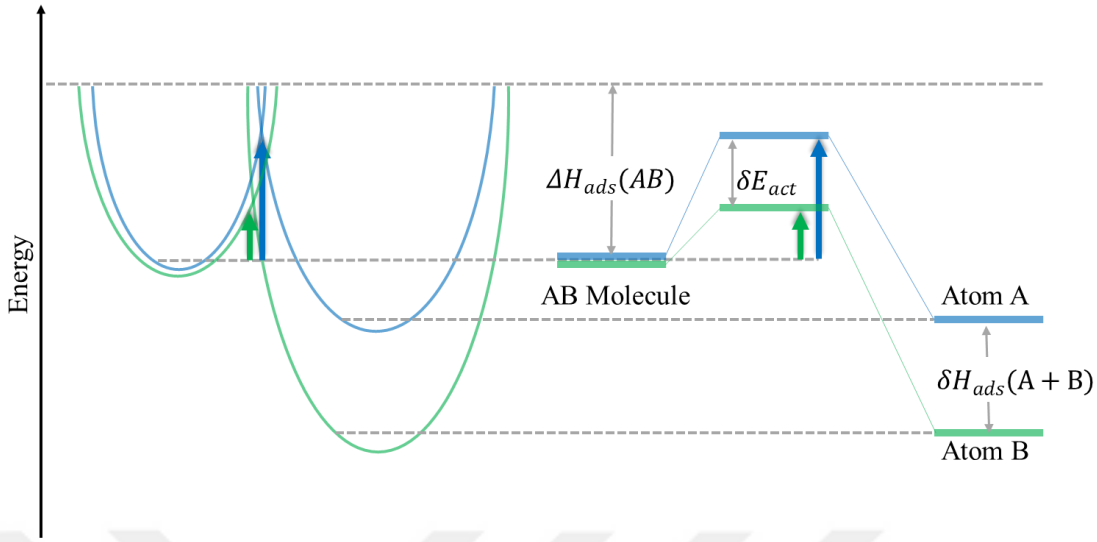


Figure 1.8. Potential energy diagram of a molecule and its dissociated atoms on two different surfaces (left). The relationship between the activation energy and the adsorption energies (right). Reprinted from [1] with permission from John Wiley and Sons.

1.1.2. Metals

In the periodic table, the adsorption energies of atoms increase from bottom-right to top-left seen in Figure 1.9, and the ability to facilitate dissociation of molecules, as a consequence. The reason for the trend from right to left is explained in Figure 1.5. The adsorption energy increases from bottom to top, since the size of metal decreases and orbital overlap between the surface and the atom increases. For instance, when CO and H_2 react on Cu, dissociation of CO cannot be accomplished, and final product becomes methanol, whereas Ni metal next to Cu has fewer electrons in its d-orbital and this leads to stronger adsorption of C and O. So, dissociation of CO is facilitated, and methane is formed. As an alternative example, CO oxidation requires dissociation of O_2 but not of CO. On the left side, for example in the case of Au, dissociation of O-O bond is not possible and at the other extreme, dissociated O atom adsorbs too strongly which diminishes the rate of reaction and more importantly C-O bond is broken. Whereas Pd and Pt meets the requirements for a successful CO oxidation [1].

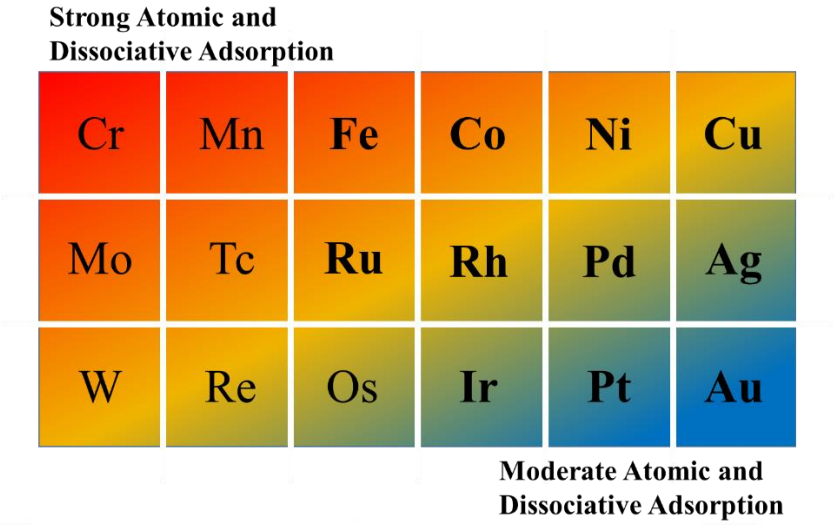


Figure 1.9. Trends in the periodic table towards dissociative adsorption.

1.1.2.1. Structure Sensitivity. Heterogeneous reactions can be classified as structure sensitive and structure insensitive, that is based on the change in the turnover frequency (TOF) per surface atom of the catalyst as a function of catalyst particle size (seen in Figure 1.10) [6].

Ammonia synthesis and alkane hydrogenolysis reactions are known to be strongly structure sensitive, on the other hand, hydrogenation of olefins and aromatics are not dependent on the structure of the surface. C-H bond activation activity decreases as the size of particle increases [6]. Hydrogenation of CO shows higher TOF on larger particles up to a certain size [6].

DFT calculations give information about insights of the relationship between reactivity and surface topology. In the case of hydrogenolysis as a type (2) reaction (seen in Figure 1.12), a single σ-bond should be cleaved on a single surface atom. As the coordination number of this atom decreases, C-H bond at late transition state will be better stabilized and this will decrease the activation energy. Since the smaller particles have relatively more edges and corners, where the coordination number of atoms decrease, the reaction becomes more facile (seen in Figure 1.11). Since hydrogenolysis involves late transition state with $\alpha_{BEP} \approx 1$, the reverse process, which is hydrogenation (a type (1) reaction) will have an early transition state and adsorption energy of the intermediates has almost no role in activation energy. That is why the hydrogenation reactions are structure insensitive.

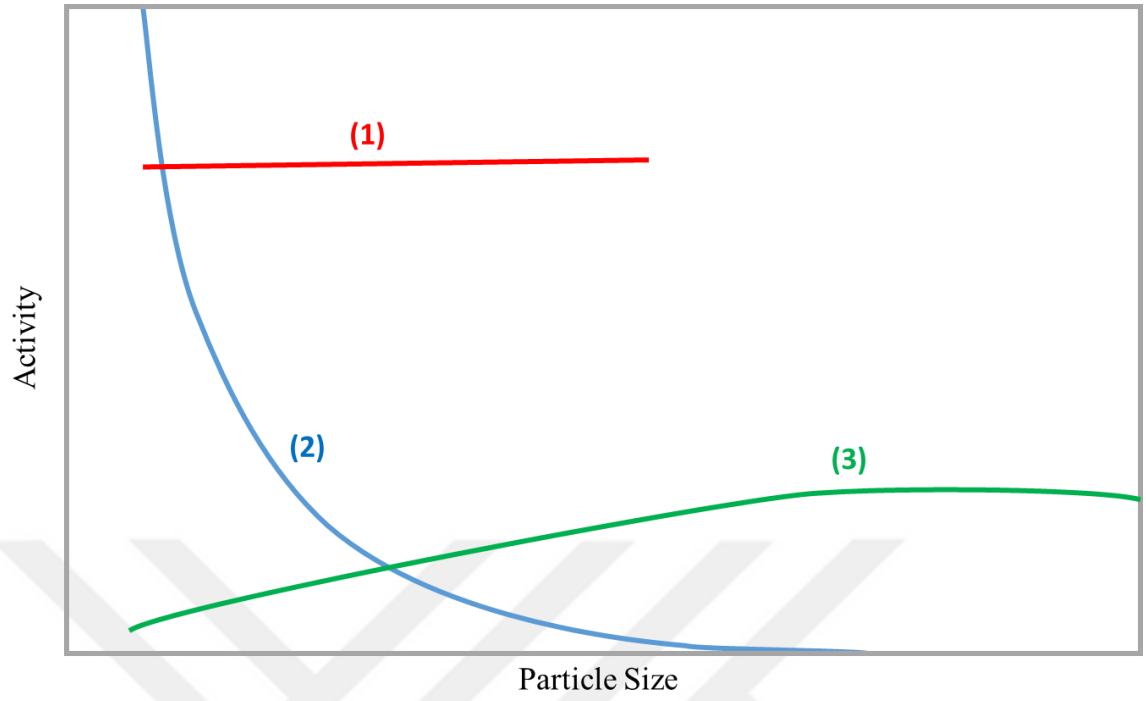


Figure 1.10. Three types of surface sensitivity, type (1) reactions are surface insensitive, type (2) reactions processes show lower activity as the particle size of the catalyst increases and type (3) reactions have an optimum particle size for the optimum reactivity. Reprinted from [1] with permission from John Wiley and Sons.

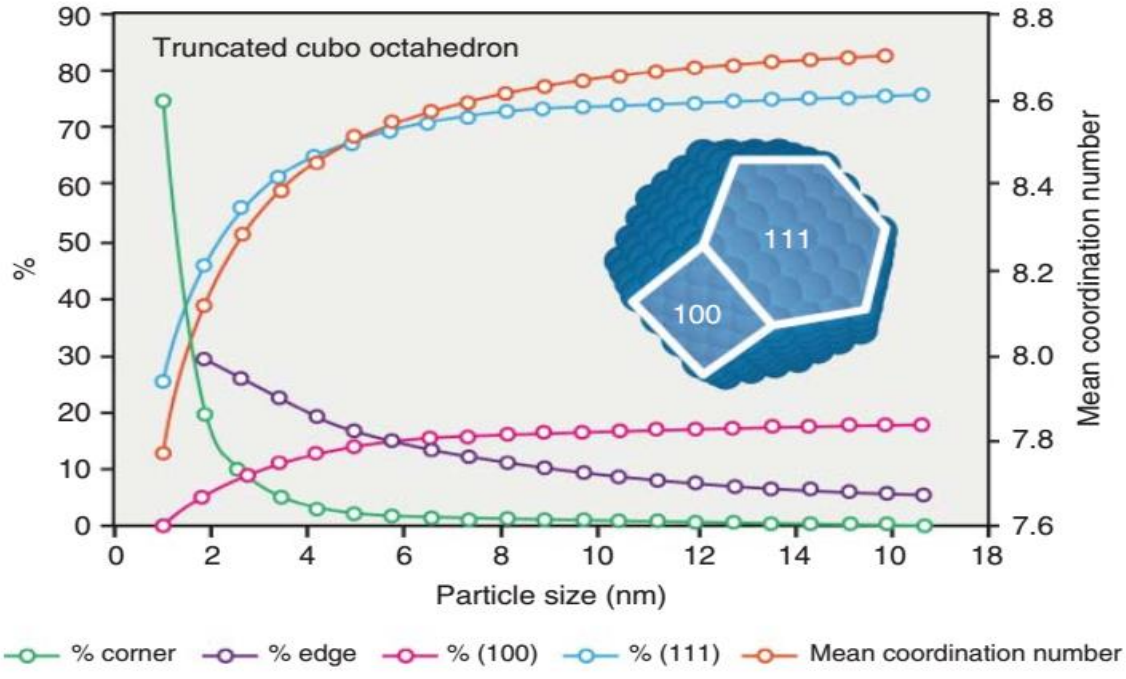


Figure 1.11. The change in the weight of different sites and mean coordination number as a function of the size. Reproduced from [9].

Type (3) reactions (seen in Figure 1.10) generally involves scission of multiple π-bonds, such as dissociation of CO, N_2 and NO. These reactions occur on sites that consist of multiple atoms, like steps. The activation barrier for dissociation of CO is greater than 200kJ mol^{-1} on planar Ru surface, it is lower than 100 kJ mol^{-1} on stepped one. There are a couple of causes for this event. First, the atoms at steps have a lower coordination number and this lowers the activation energy. C and O atoms can bind to different surface atoms at the transition state and it does not need to bend towards the surface on stepped surfaces. So, the backdonation to π*-antibonding orbitals of CO is eased (seen in Figure 1.12).

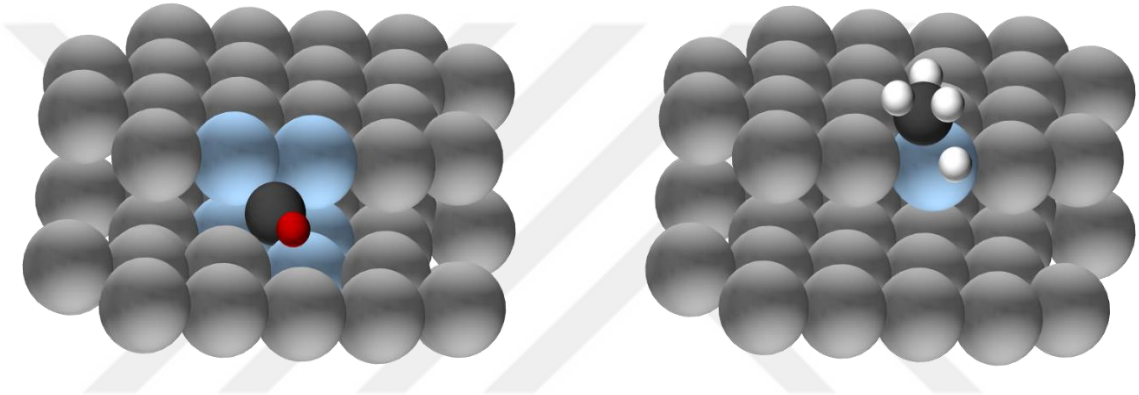


Figure 1.12. Transition states of CO dissociation (on the left), and methane dissociation (on the right) on a stepped surface.

1.1.2.2. Support Effect Heterogeneous catalysts are being implemented on support materials to avoid sintering and to provide mechanical strength, in general. But also, semiconductor support materials, such as TiO_2 are being used to facilitate electron transfer to/from the metal nanoparticle catalysts for electrochemical applications [7].

The strength of the interaction between the support and the metal can define the structure and properties of the catalyst. If it is weak metal particles tend to preserve their structure, whereas strong interactions lead to wetting of the support by the metal, as a consequence electronic structure of the catalyst may change and that automatically alters the behavior of the metal. In this case, the support materials can even migrate over the catalyst and block the active sites [8].

In some cases, the support material can react with the metal and the resulting compound would naturally have different properties. Also, the support can take part in the reaction together with the catalyst [9]. Such systems are named as bifunctional catalysts. This can happen in two different ways:

(i) The reaction can occur at the three-phase boundary of catalyst, support, and air.
(ii) If a step of reaction produces mobile intermediates on a metal surface, these can migrate to support and continue to react there. This event is named as spillover [9].

To achieve reactions with high activity, selectivity, and stability, there are myriad of parameters to be optimized. The requirement of this is fundamental knowledge of each step of reactions and this can be achieved through intense interdisciplinary work of different fields ranging from surface science to quantum chemistry.

1.2. Fischer-Tropsch Synthesis

Sabatier achieved first syngas conversion with nickel (Ni) and cobalt (Co) catalyst to synthesize methane in 1902. Then Franz Fischer and Hans Tropsch carried this idea further to the synthesis of hydrocarbons which can be used as fuels in the 1920s. In their first patent, they reported the synthesis of hydrocarbons at 300°C with iron and cobalt catalysts [10]. The first commercial plant was established in 1936. This technology supplied fuel to Germany and Japan during the World War II. Then China built cobalt based FT facilities from the 1940s to 1960.

After the war, efforts of US on FTS came out with new two-phase high-temperature Fischer-Tropsch synthesis [11] and small plants were built in the 50s. South Africa was the place, where large-scale FTS production has happened [12]. In 1955 Sasol built the first plant, which operated high- and low-temperature FTS with an iron catalyst to produce fuel and wax, respectively. In the 1970s when oil crises came out, Sasol built its 2nd and 3rd plants. The crises also led the companies like BP, ExxonMobil, Gulf, Shell, and Statoil to invest in FTS, especially to cobalt-based one [13, 14]. In the last 20 years, this has led to new commercial GTL plants by PetroSA (South Africa; 1993), Shell (Malaysia; 1992),

Sasol-Qatar Petroleum (Qatar; 2007), Shell (Qatar; 2011), and Sasol Chevron (Nigeria; under construction – start-up2013) [15].

Fischer-Tropsch Synthesis (FTS) is the technology which makes the conversion of any carbon feedstock to hydrocarbon chains. It is based on the reaction of carbon monoxide (CO) and hydrogen (H_2) on the active metal catalyst to give hydrocarbon chains which can be used as liquid fuel. But it also gives a wide range of organic compounds from straight-chain alkanes, olefins to oxygenated compounds such as alcohols that can put the FTS at the heart of the chemical industry. The process is highly exothermic, and the main byproducts are water (H_2O) and carbon dioxide (CO_2) depending on the activity of catalyst towards water-gas shift (WGS) reaction. The simplest equations for the process are:

$$\text{FTS:} \quad CO_{(g)} + 2H_{2(g)} \rightarrow -CH_2 - + H_2O_{(g)} \qquad -165\text{kJ mol}^{-1}$$

$$\text{WGS:} \quad CO_{(g)} + H_2O_{(g)} \rightleftharpoons H_{2(g)} + CO_{2(g)} \qquad -42\text{kJ mol}^{-1}$$

FTS reaction implies the FTS is a polymerization reaction and the product contains hydrocarbon chains that have various molecular weight. That is why selectivity of catalyst plays an immense role for the product quality.

The whole process from the source of the syngas to the final product of FTS is named according to the feedstock, namely coal to liquid (CTL), gas to liquid (GTL), biomass to liquid (BTL) and XTL for overall. In all cases, the feedstock is converted to syngas (CO + H_2). Solid carbon sources are generally gasified noncatalytically, by partial oxidation and reaction with steam. If natural gas is to be employed, adiabatic reformation with oxygen or steam is applied. This approach can be implemented as autothermal reforming (ATR), noncatalytic partial oxidation (POX) and catalytic partial oxidation (CPOX) [15]. Actually, the principle is the same with the solid feedstocks. Alternatively, the process based on external heat supply in the presence of only steam and/or CO_2 can be applied for the reformation of natural gas, which can be listed as steam reforming (mainly with steam), dry reforming (mainly with CO_2) and heat exchange reforming [15]. Generally, nickel (Ni) is implemented as an active catalyst for reforming [16]. Once obtained, syngas is converted catalytically to hydrocarbons, mainly to linear alkanes and 1-alkenes as the second step of the XTL process. In the last step, the product, which is a wide distribution of molecules with

different molecular weight is refined. This step includes hydrocracking of long chains to middle distillates.

During FTS, the C-O bond is dissociated, and new bonds between carbon and hydrogen are formed, which is a hydrogenation reaction. Also, for the occurrence of chain growth, new C-C bonds are formed. Since this is a polymerization reaction, there is a competition between chain growth and chain termination and this is represented by the α-value, which is the chain growth probability (displayed in Figure 1.13). The probability of having n number of carbons is given by the formula:

$$C_n = n(1-\alpha)\alpha^{n-1}$$

And the total number of carbons in the product is given by:

$$\sum_{1}^{\infty} C_n = \sum_{1}^{\infty} n(1-\alpha)\alpha^{n-1} = \frac{1}{1-\alpha}$$

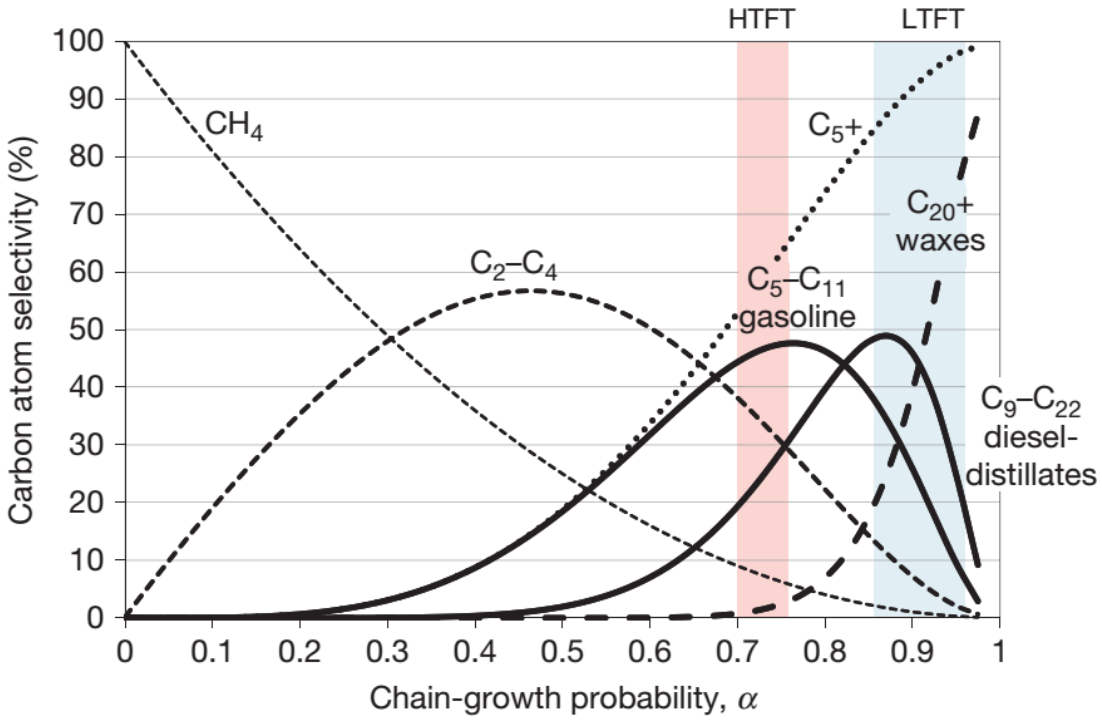


Figure 1.13. Product spectrum of FTS with varying chain growth probabilities. Reprinted from [15], Copyright (2013), with permission from Elsevier.

Selectivity towards the hydrocarbons with n number of carbons is given by S_n:

$$S_n = \frac{C_n}{\sum_1^\infty C_n} = n(1-\alpha)^2\alpha^{n-1}$$

So that [15]:

$$\ln\frac{S_n}{n} = n\ln\alpha + \ln\frac{(1-\alpha)^2}{\alpha}$$

Accordingly, $\ln(S_n/n)$ versus n graph gives a linear curve, which indicates that the FTS product shows Anderson-Schulz-Flory (ASF) distribution. But usually, deviations from this ideal rule is observed [17–20]. While selectivity toward methane is higher than expected, C_2-hydrocarbon gives lower yield than the model predicts. Additionally, as the chain length increases, the olefin to paraffin ratio decreases. Besides linear alkanes and 1-alkenes, compounds like branched aliphatic molecules, alcohols, aldehydes, ketones, acids and even aromatics are found within product spectrum. This indicates the complexity of the reaction mechanism, which has a myriad of unresolved issues. It is also unknown if these compounds are the result of primary reactions or secondary reactions of products. For instance, possible reactions for α-alkenes are hydrogenation, isomerization, cracking and hydrogenolysis, insertion into growing chains [18, 19].

Iron (Fe), cobalt (Co), ruthenium (Ru) and nickel (Ni) are known to be active metals towards FTS. But Ru is not practical to be used due to its cost and nickel only gives methane as a product at the reaction conditions which suppress nickel carbonyl formation. So iron and cobalt are remaining catalyst materials for commercial applications [21–23]. Iron catalyst gives more oxygenated products and alkenes, most probably due to its inability towards hydrogenation compared to cobalt. Iron is active as a mixture of oxides and carbides [22,24], while cobalt catalyzes FTS at its metallic state [21].

The byproducts of FTS are dictated mainly by the way of removal of oxygen from carbon monoxide. For the case of cobalt, it is removed as water, but since iron is active towards WGS reaction, oxygen is also removed as carbon dioxide.

$$\text{FTS:} \quad CO_{(g)} + 2H_{2(g)} \rightarrow -CH_2 - + H_2O_{(g)} \qquad -165\text{kJ mol}^{-1}$$

$$\text{WGS:} \quad CO_{(g)} + H_2O_{(g)} \rightleftharpoons H_{2(g)} + CO_{2(g)} \qquad -42\text{kJ mol}^{-1}$$

Relative conversion rates of CO and H_2 is an important factor for FTS. If there is no WGS the hydrogen to carbon monoxide ratio (usage ratio) is determined only by the first reaction and should have the value of around 2. In another extreme case, where all the oxygen from carbon monoxide is removed through WGS, H_2/CO ratio can be 0.5. Since cobalt has a low propensity towards WGS, it is used as GTL catalyst, since natural gas has usage ratio around 2 or higher. When syngas from feedstocks that have lower usage ratio, iron is used as FTS catalyst because of its WGS activity.

Different application types of FTS dictate the type of reaction conditions and reactor designs, accordingly. High-temperature FT (HTFT) synthesis is named after its process temperature, which is around 300-350°C, where there is the only product in the gas phase. Mainly this synthesis is performed at circulated fluidized bed reactors, but recently it is operated in a fixed fluidized bed reactor. Since methane is the only product of cobalt catalyst at this reaction conditions, iron catalysts with alkali promoters are implemented. Moving bed reactors demand robust catalyst particles that is why only fused iron catalysts are being used for HTFT synthesis. The product spectrum of HTFT synthesis consists of light hydrocarbons, which makes it well suited for gasoline synthesis. But it has also high selectivity towards linear 1-alkenes and some oxygenated compounds [25].

Low-temperature Fischer-Tropsch (LTFT) synthesis runs at 200-250°C [26, 27], both iron and cobalt catalysts are suitable. This process gives heavy hydrocarbons extending to waxes, which are liquid at reaction temperatures, which results in the gas-liquid-solid three-phase system. Generally, fixed-bed reactors seen in Figure 1.14 are employed. To hinder pressure-drop, the particle size must relatively large (millimeter range), but this causes the problem of diffusion reactants since the rate of CO and H_2 is different. This results in heterogeneity of usage ratio at different reaction sites. Another problem with this system is the occurrence of temperature profiles, due to the exothermic nature of FTS.

To avoid some of these problems, slurry bubble column reactors have been employed, lately. In this system reactant gases are bubbled through the reaction slurry, which has

catalyst materials with sizes in the micrometer range. So intra-particle diffusion problem is averted, and well-mixed slurry helps to maintain homogeneous heat distribution. The drawback of this system is the requirement of well-established extraction of products from the reaction medium.

Some research on the advancement of non-commercial reactors such as microchannel reactors is promising candidates for next-generation FTS. While high mass and heat transfer are attained, the fixed bed nature of it eliminates the problems of slurry reactors [28]. In addition, some monolith type reactors are being worked on by academia, where the active metal is loaded on structures with a specific geometry [29].

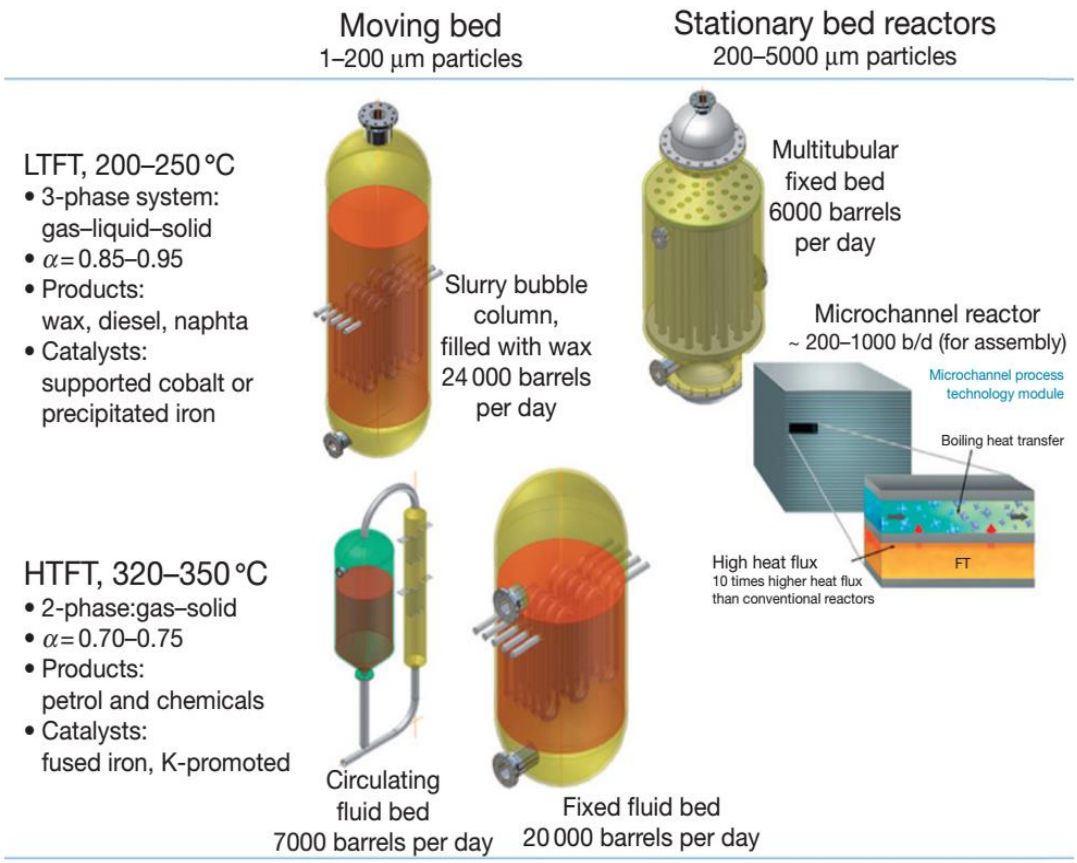


Figure 1.14. FTS reactor types, slurry bubble reactors (top-left), multitubuluar fixed bed reactors (top-right), circulating fluid bed reactors (bottom-left) and fixed fluid bed reactos (bottom-right). Reprinted from [15], Copyright (2013), with permission from Elsevier.

1.2.1. Iron-Based FTS

The process of FTS with the iron catalyst is one of the most studied heterogeneous catalyst systems because of its versatility. While it can generate light hydrocarbons, C_{35+} waxes can be synthesized. Iron is being used since the 1950s by Sasol and it is around 250 times cheaper than cobalt. Besides, it is known to be more tolerant to poisoning (e.g. by sulfur in synthesis gas). The iron catalyst is also sensitive to manipulations by addition of promoters or by reaction conditions, such as temperature, pressure and usage ratio of hydrogen and carbon monoxide. The chain growth probability (α) has the value ca. 0.94 at relatively lower temperatures (around 235°C), which results in a product spectrum composed of mainly C_{21+} hydrocarbons. However, α value becomes 0.7 at HTFT conditions and that generates lighter compounds. The main drawback of the iron FTS catalyst is its fast deactivation rate [15].

Despite the studies on iron FTS catalysts, its complex transformation during activation and FTS remains to be unsolved. The mixture of iron oxides (e.g. hematite and magnetite) which occurs at the preparation phase turns into carbides during activation. In the literature there are a couple of preparation methods for iron FTS catalyst, precipitation and fusion is being among the most common ones [30]. Commercially prepared iron catalysts are oxides, hydroxides, and oxy-hydroxides which requires pretreatments such as reduction or exposing it to syngas under elevated temperatures. An ideal FTS catalyst needs to be mechanically robust, stable, active and highly selective towards the aimed product. Conditions in which FTS runs, namely if it is HTFT or LTFT and the reactor design, dictates the preparation method of catalyst materials. In the case of tubular fixed-bed reactors, the shape and size of the catalyst have greater importance than the strength of catalyst, since the main limitation of these type of reactors stems from mass transport constraints. But for fluidized-bed-type reactors, the strength of the catalyst is an important factor among others [31].

Cost and availability are the main criteria while assigning the source of iron. While different kinds of oxides are abundant on earth, purity of the precursors must be in chemical grade to make sure to control the composition of final catalyst material, since impurities play a role on the properties of it. A common way to prepare iron catalyst is to the conversion of scrap iron to iron (III) nitrate, as a primary step for the case of the precipitation method.

Ores or scales of iron are the raw materials for the fusion preparation method. Complex novel methods are not adopted commercially, since they do not justify the cost, yet.

Catalysts, which are prepared by the method of fusion, have a low surface area, high density, and inherent robustness (seen in Figure 1.15). That makes it appropriate for FTS with fluidized-bed-type reactors. In this process, iron oxide particles are heated to the temperatures at 1000°C along with the precursors. Then the melt is cast on ingots and milled to a desired particle size after cooling. The problem with this is the inclusions of silica and alumina impurities, which are presented in the raw material, which happens in the process of cooling. The alkali promoters migrate and combine to these inclusions, which in turn affect the catalyst performance in a negative manner.

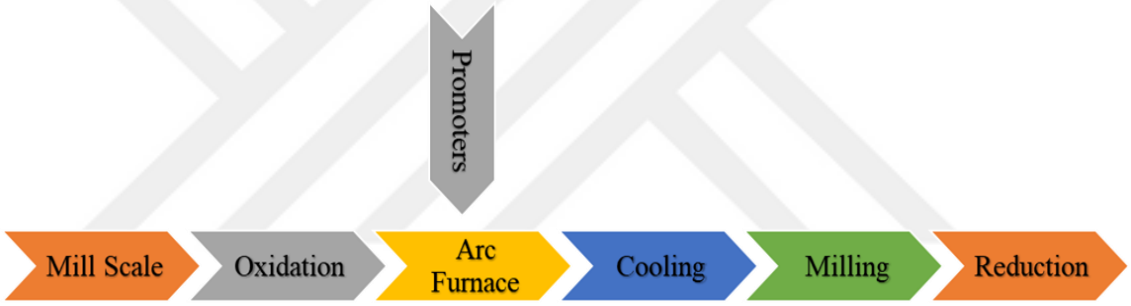


Figure 1.15. Process diagram of catalyst preparation by the fusion method.

Another catalyst preparation method, precipitation, is also being frequently used and it was one of the first approaches [32]. Later, Ruhrchemie established a precipitation process (seen in Figure 1.16), in which iron (III) salts are precipitated by a base to get oxides and oxy-hydroxides. The size of the particles and surface area were able to be controlled by modifications on reaction conditions, like temperature, pH, and precipitation rate. Then the precipitate is washed, filtered and reslurried to add Si, Al etc. as structural promoters. Then the slurry is spray-dried and calcinated. Spray-drying gives spherical particles, which are suitable for the chosen reactor type and the calcination removes volatile impurities like H_2O and NO_x and strengthens the catalyst. This method provides catalysts with increased strength, homogeneous distribution of promoter and since the shape of them are spherical, it helps to the fluidization of the reactor.

Iron Fischer-Tropsch catalysts show low activity, low selectivity, and sintering, but these problems can be solved by the presence of structural and chemical promoters. Structural promoters, such as Si, Al, and Mg helps against sintering and they preserve the active phase while increasing the mechanical stability. Alumina and silica stabilize the hematite phase of iron FTS catalysts [33]. Iron oxides maintain their high surface when they are implemented on silica structural promoter, even they are calcined at high temperatures. The activation of the catalyst becomes more difficult due to structural promoters, because they form iron silicates and aluminates together, and these compounds are difficult to be reduced. That is why chemical promoters like Cu and Ag is used since they help the reduction of oxides through hydrogen spillover. In addition, chemical promoters help to the nucleation of iron intermediates, so that the catalyst has higher surface area. They also increase the number and types of CO adsorption sites, stabilize selected phases and change the kinetics of secondary reactions [34].

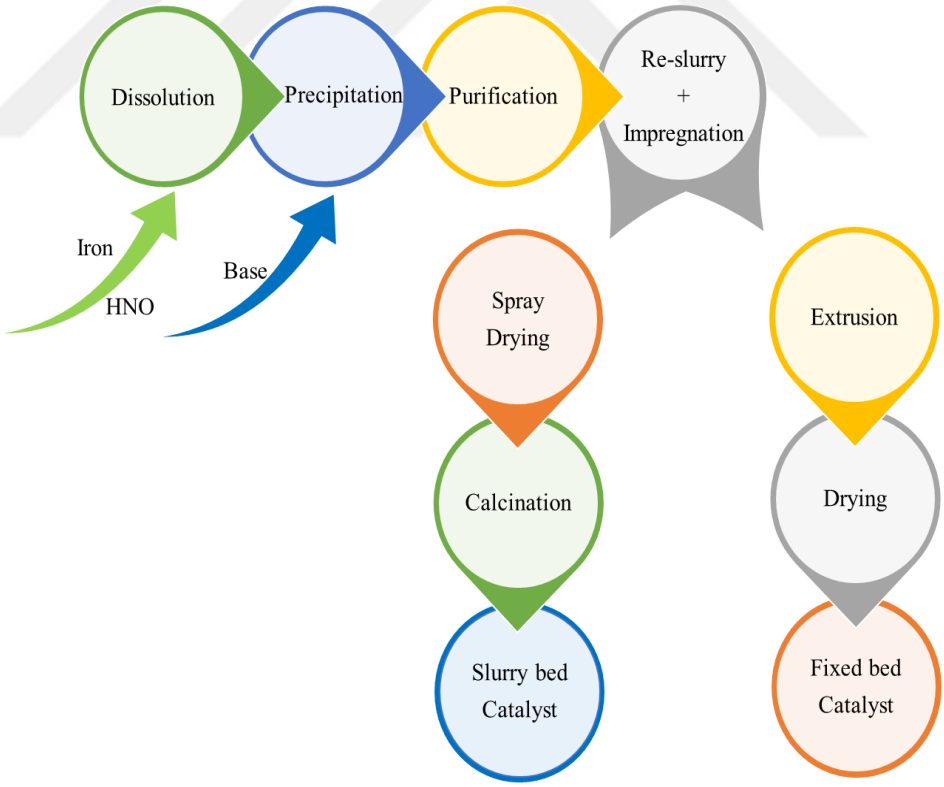


Figure 1.16. Process diagram of catalyst preparation by the precipitation method.

Alkali metals as a chemical precursor for LTFT synthesis are known to increase chain growth probability (α), diminish methane formation and hydrogenation rates, so the product has higher alkene to alkane ratio [35]. Also, alkali earth metals have similar effects.

Iron is inactive in the form of oxides and oxyhydroxides, so one needs an activation step prior to FT synthesis. This step is executed by hydrogen, carbon monoxide or syngas, dictated by the type of application (HTFT or LTFT). Chemical and structural promoters are important factors for the optimization of activation conditions. The activated phase's stability and composition play the most important role in the performance of FTS. That is why the activation procedure is critical for the activity and selectivity [36].

Removal of water is crucial for the reduction of iron oxide. The thermodynamic equation for the degree of reduction is:

$$\Delta G = \Delta G^{\circ} + RT\ln\frac{\rho H_2O}{\rho H_2}$$

ΔG is the change of free energy in the reaction conditions, ΔG° is standard free energy change of reduction reaction, R is ideal gas constant, T is the temperature and ρ is the partial pressure of gases. The equation tells that the faster the water is removed, the higher the degree of reduction will be achieved. The degree of the reduction can be predicted from the rewritten form of this equation:

$$\Delta G = nRT\ln\left(\frac{\rho H_2O}{\rho H_2}\right)\Big/\left(\frac{\rho H_2O}{\rho H_2}\right)_{eq}$$

$(\rho H_2O/\rho H_2)_{eq}$ is the ratio of partial pressures of water and hydrogen gas at equilibrium. Theoretically, for a high degree of reduction, the water content of the reaction medium must be below 1% [37, 38].

To understand the activation mechanism, it is essential to study the phase transformations on the catalyst surface. X-ray Diffraction (XRD), and Mössbauer Spectroscopy are strong tools for investigating the phases of iron, even though small sites and particles limits the information collected by XRD [39–41].

At the end of activation with CO, the resulting phases of catalyst are metallic iron (α-Fe), iron carbides (Fe_xC_y) and magnetite (Fe_2O_3). The ratio between these phases is

dependent on the activation conditions like temperature, the flow rate of activating gas and the composition [41].

Iron carbides are believed to be the active phase for FTS [42]. But there is a considerable amount of unknown about the nature of carbides during the process. Bulk stabilities of carbides are reported as: ε'-$Fe_{2.2}C$>ε-Fe_2C>χ-Fe_5C_2>θ-Fe_3C [43]. Depending on the preparation and activation methods of iron catalysts different types of carbides are formed. Besides metallic α-Fe has a chance to play a role [24]. For the catalysts prepared by the precipitation method, the hematite phase has a tendency to turn into magnetite, regardless of the gas used at the activation phase. But after that conversion, the choice of the activation gas manipulates the final composition. If hydrogen is used, it will turn into α-Fe, while it becomes Hägg-carbide (χ-Fe_5C), if it is performed under CO or syngas. Herranz et al. showed that the hematite will transform mostly to cementite (θ-Fe_3C) under CO, and Hägg-carbide (χ-Fe_5C) under syngas [44]. Reduction of fused magnetite FT catalyst under hydrogen at around 400°C leads to an increase in the surface area due to the removal of oxygen from oxide sites [45]. To maintain a high degree of reduction, this process is implemented with fast gas flow to bypass re-oxidation by water. Carbon monoxide and syngas do not cause any reduction on nonporous magnetite.

The activation conditions of iron catalysts which are prepared by precipitation method, are milder. These catalysts have higher porosity, higher surface area and it is subject to sintering at high temperatures. The relationship between the conditions of the activation process, the choice of gas and FTS activity were mentioned. It is shown that the activation of precipitated LTFT catalysts by carbon monoxide gives the best results in terms of low methane selectivity and high conversion rates [46].

The activity and selectivity of iron FTS catalysts can be manipulated by reaction conditions and composition of catalyst material, the latter plays a greater role. At lower temperatures, FTS shows higher selectivity towards longer hydrocarbons. Alkali promoters cause deviations from Anderson-Schulz-Flory distribution due to the introduction of a second α-value (seen in Figure 1.17). Addition of manganese (Mn) to Ruhrchemie catalyst leads to increased α-olefin selectivity at LTFT conditions [47]. A method called ChemFT

comprise of the introduction of various promoters at the same time (e.g. Fe/Zn/Mn/Cu/K/SiO2) to aim synthesis of different chemicals.

Stability is an essential element of a successful catalyst which implies the retention of its activity and selectivity throughout the stream time. The biggest drawback of the iron catalyst is its short lifetime. Recent studies are focused more on the extension of catalyst life of iron, rather than improvements on activity or selectivity. The reasons of deactivation are ascribed to: fouling of catalyst by the formation of free carbon, phase transformations such as oxidation during the process, mechanical decays, poisoning due to some gases presented in syngas and sintering.

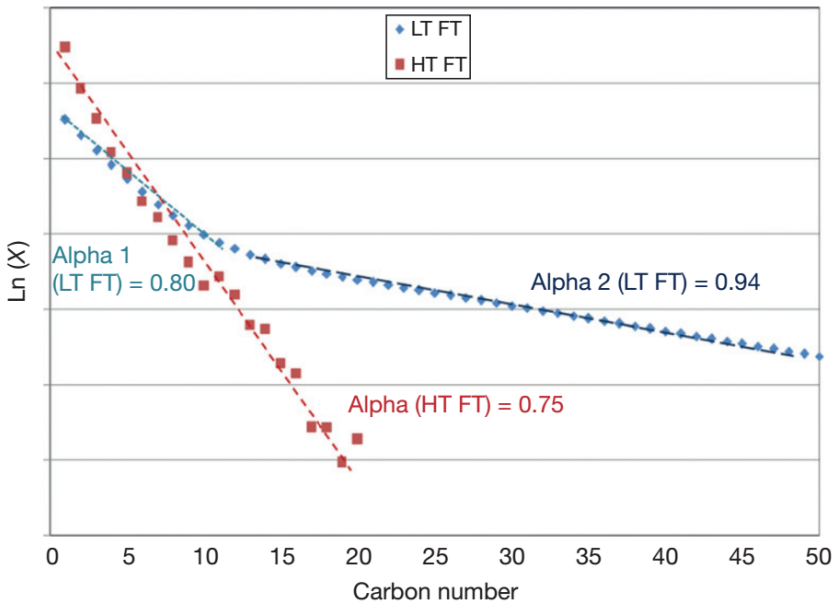


Figure 1.17. Anderson-Schulz-Flory distribution of LTFT and HTFT synthesis with iron catalysts. Reprinted from [15], Copyright (2013), with permission from Elsevier.

Free carbon formation is among major factors against catalyst life for HTFT. This buildup decreases the strength and density of catalyst and leads to bed expansion, particle break-up and loss of fine material [25]. Particle break-up has two sides: it exposes new active sites, and it is the desired accident since carbon covers the bulk of catalyst. But the carbon dust includes a high amount of alkali metal, which means the loss of promoter and selectivity, in turn. The most credible reasoning for the origin of free carbon is one of the possible reaction routes of carbon that is formed after the dissociation of carbon monoxide:

(i) The dissociated carbon can form carbide with iron.

(ii) The dissociated carbon can bind to the dissociated hydrogen atoms to form hydrocarbons.

(iii) A dissociated carbon can bind to another dissociated carbon and that is when the free carbon is formed [48].

Addition of promoters may reduce the formation of free carbon. Sasol has developed a catalyst which involves chromium (Cr) to suppress this issue [49].

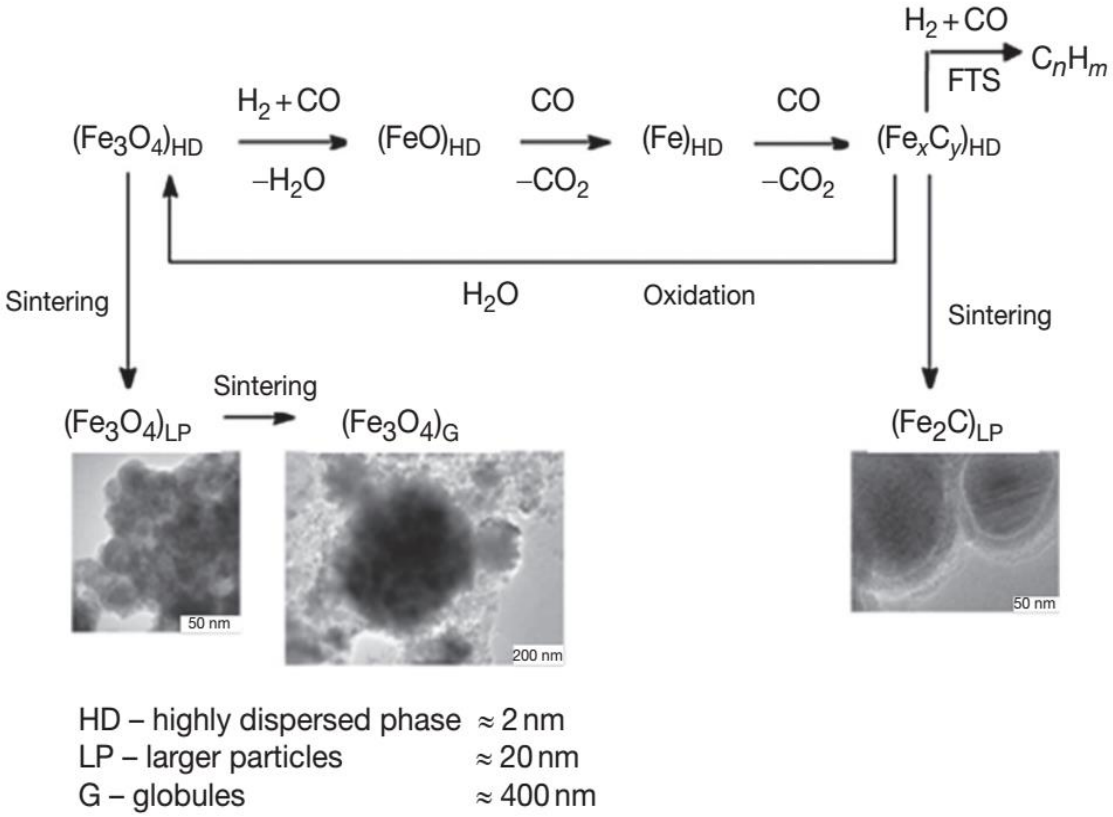


Figure 1.18. Deactivation mechanism of Ruhrchemie iron catalyst under LTFT conditions. Reprinted from [15], Copyright (2013), with permission from Elsevier.

For LTFT, while free carbon formation is a less noticeable factor for deactivation, sintering and oxidation become major challenges to overcome. Different types of carbides that are formed during the activation process, can undergo interconversion. This leads to the formation of carbon at interface boundaries, which weakens the catalyst particles seen in Figure 1.18.

1.2.2. Cobalt-Based FTS

The topic of cobalt FTS catalyst had a great interest in the last 20 years. Academic and industrial research brought up a tremendous amount of knowledge about nature about the active site, the effect of catalyst size on activity and selectivity and deactivation pathways [21, 27, 50–55]. General characteristics of the composition cobalt FTS catalysts that are adopted from academia and industry, are as follows [14, 56, 57]:

(i) Cobalt as active metal (10-30 wt.%).
(ii) A reduction promoter metal (usually a noble metal) (0.05-1 wt.%).
(iii) A structural oxidic promoter (e.g. Zr, Si or La) (1-10 wt.%).
(iv) A refractory oxidic support.

Because of cobalt's high cost as a catalyst material, optimization of its dispersion is a key parameter to maximize its use. Metallic state of cobalt is the active phase for FTS, so, it is very important to expose active sites as much as possible and this can be achieved by varying particle size, structure and the degree of reduction, while considering issues regarding mechanical stability [57].

Primary activation requires a degree of reduction greater than 60% but it should be also considered that cobalt will be further reduced at reaction conditions (seen in Figure 1.19). The optimum particle size for cobalt catalyst is just above 8-10 nm. Smaller particles show lower turnover frequency (TOF) and are more prone to sintering [58]. This also causes difficulties in a reduction because particle-support interaction increases as the size decrease.

Two phases of metallic cobalt, which are supported, are presented: face-centered-cubic (fcc) and hexagonal-closed-pack (hcp) [21, 59]. For particles smaller than 40 nm, it is reported that the predominant phase is fcc [60]. The activation process, promoters, and support have impact on the weight distribution of phases [21]. Studies claim that the activity of hcp sites is higher towards FTS [61].

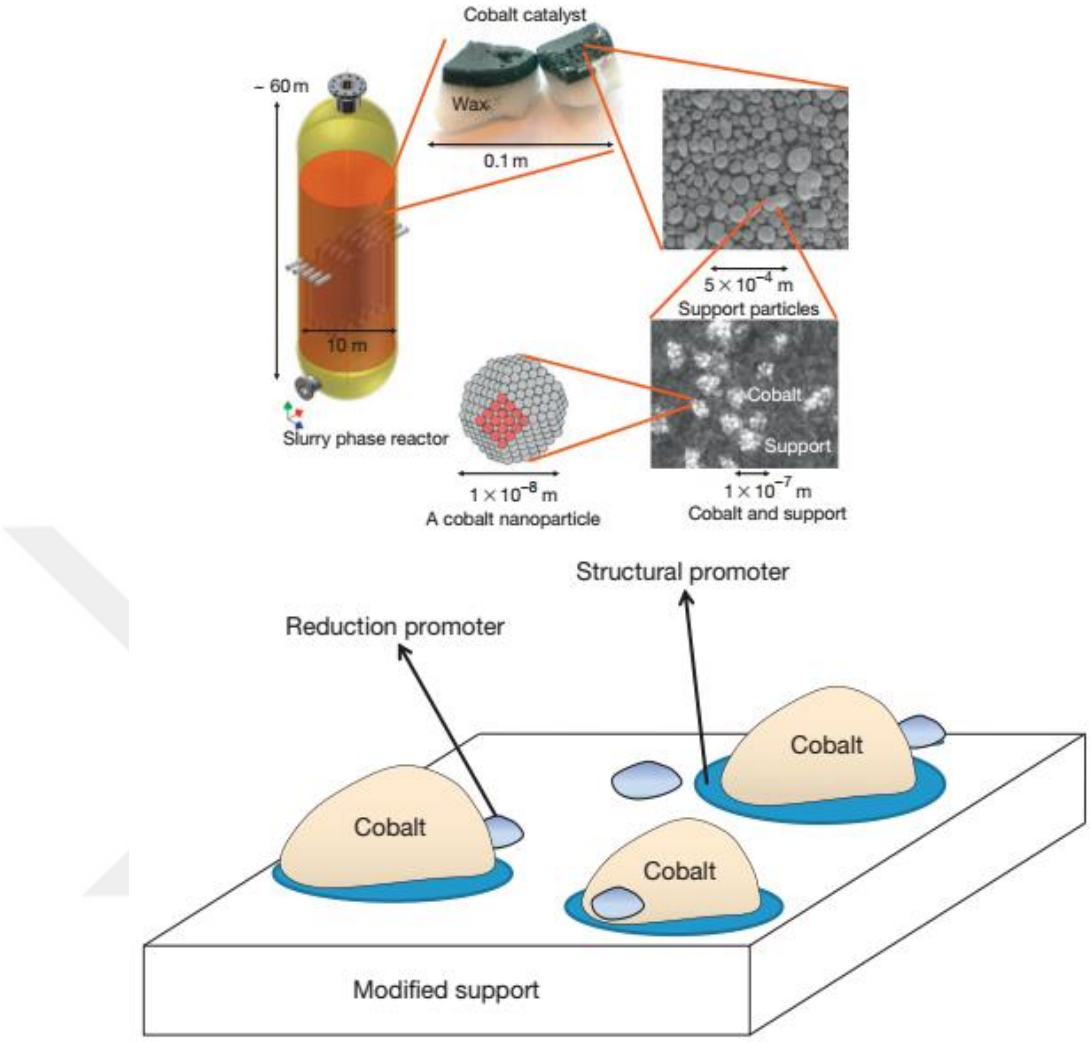


Figure 1.19. Composition of cobalt FTS catalyst prepared for the slurry phase reactor. Reprinted from [15], Copyright (2013), with permission from Elsevier.

The reason to use noble metal promoters (Pt, Ru, Re) for cobalt FTS catalyst is the strong interaction of catalyst with oxidic support (e.g silica, alumina, titania), which diminishes the ability of reduction. So, these noble metal promoters increase the reducibility and activity, in turn. These metals are more active than cobalt at hydrogen activation, so the resulting hydrogen spillover from these metals to cobalt facilitates the reduction [21, 57]. Noble metal promoters affect the decomposition of cobalt precursors and that plays a role in the nucleation process and average size of catalyst particles becomes smaller [57]. According to literature, ruthenium forms alloys and bimetallic particles, which affects the activity, selectivity and it keeps the surface clean, so it facilitates the catalyst regeneration [62].

Structural promoters act upon the formation and stability of active phase. Zirconium (Zr) is known to decrease the cobalt-silica interaction at silica supported cobalt catalysts and that helps in the reduction of cobalt [21, 63]. Zr is reported to suppress the cobalt aluminate formation at alumina supported catalysts [64]. B [65] and Ni [66] prevent free carbon formation.

The purpose of support is to provide thermal and mechanical stability and to facilitate high dispersion of catalyst. Composition and the structure of support are crucial for overall performance. Patents in the 1980s require alumina support with high purity, low acidity and high surface area (150-250 m^2g^{-1}) [67–69]. Recently, alumina-based supports such as nickel promoted α-Al_2O_3 is reported to have better stability and selectivity towards C_{5+} hydrocarbons when it has a surface area of 50 m^2g^{-1} [70]. The pore size of support is another important parameter for FTS, as an example in literature, it is claimed that for the optimum size of a cobalt catalyst, the size of support's pores should be around 12-16nm [71].

The support must also be stable under harsh reaction conditions. It is observed that unprotected alumina supports undergo decays due to hydrothermal attack and this causes to contamination of the product [72–74]. Coating the alumina support with silica is an alternative solution to this problem. TiO_2 is also a commercially used support material with high thermal stability and resistance against high water pressure.

Also, there are some non-commercial support materials embraced by the academia, such as MCM-41, SBA-16, carbon nanofibers, nanotubes, spheres [21, 58, 75]. Carbon has a weak interaction with cobalt, so high degrees of reduction can be achieved easily and it is used as a support to understand the size-effects of cobalt particles.

As with the iron-based FTS catalysts, the choice of the preparation of cobalt catalyst depends on the application, namely, aimed product spectrum, reactor choice, reaction conditions etc. Mostly used methods are as follows:

(i) Coprecipitation of cobalt, promoters and support material.
(ii) Precipitation or impregnation of cobalt and promoters to support.
(iii) Impregnation of cobalt onto a pre-shaped support.

Coprecipitation was the most common method of FTS catalyst preparation at the initial stages of the industry. Also, some modern FTS applications still implement this method like Co/Mn catalyst [76], Co/Mg/SiO_2 and Co/ZnO_2 [77].

This procedure has these principle steps: precipitation, washing, drying and shaping. Control of the size and composition are adjusted by temperature, precipitation agent, precursor salts, structure-directing or organic hydrolysis reagents, aging time, and reaction atmosphere (air or N_2). If precipitation agent is chosen to be Na_2CO_3 or KOH for preparation of Co/SiO_2 catalyst, there occurs formation of cobalt silicate, which is catalytically inactive. To remove excess chemicals the product should be filtrated and washed because even small amounts of alkali metals and halogens are detrimental to catalyst performance. As the last step, these precipitates are shaped by either reslurried and spray-dried or extruded and pelletized, former for bubble bed reactors and former for fixed-bed reactors. Addition of acid to the final form of the catalyst increases the final strength of the catalyst [78].

In addition to coprecipitation, there are methods based on the attachment of catalyst materials to pre-shaped support particles. In this application to have the optimum amount of cobalt crystals with a size of 8-10 nm, support materials should mainly have the following properties:

(i) The amount of the precursor that can be added per impregnation is determined by the pore size of the support.
(ii) The time required to get a well-dispersed catalyst depends on diffusion path length, pore size, viscosity, wetting properties and diffusion coefficients [79–81].
(iii) For fixed-bed reactors, eggshell type catalyst material is required to avoid pore diffusion limitations. This geometry is maintained by the addition of viscosity enhancers or using cobalt salt melts.

After the drying, the catalyst material is calcined to immobilize cobalt on the support. The calcination conditions play a key role in a good catalyst. For the case of cobalt catalyst synthesized from cobalt nitrate precursors, successful removal of NO_x and water at the calcination phase is very important [82]. To minimize the mobility of cobalt this overall step should proceed very fast, which requires optimizations on heat flow.

Also, the gas used at the calcination step affects the end results. Using NO in this process generates cobalt hydroxy nitrate, which is less mobile and helps optimization of cobalt phase dispersion [83]. H_2 and CO as calcination gas also give a good dispersion of cobalt, at temperatures lower than the reduction temperatures [84].

After the calcination, cobalt particles are reduced under H_2 or dilute H_2 atmosphere. Some examples of reduction with CO are present but the formation of carbon on cobalt is a problematic issue in that case. The reduction conditions and temperatures are dictated by the type and amount of reduction promoters, alkali promoters that make the reduction more difficult, support, support modifiers ant the cobalt precursors. Cobalt catalysts are prone to sintering at high temperatures, which causes to loss of surface area. It is reported that at temperatures higher than 350°C formation of cobalt silicate is observed at Co/SiO catalysts.

As almost every step of catalyst preparation, reduction procedure is crucial for catalyst performance [85]. Consecutive reduction-oxidation cycles can improve the performance up to the values of 30% [86].

The performance of FTS is a function of reactor choice, hydrodynamics, heat transfer, mass transfer, and pressure [21]. The choice of catalyst should be made accordingly. For instance, Co catalysts show higher activity in fixed-bed reactors when compared to slurry-bed reactors. But the optimum reaction temperature at slurry-bed reactors is 230°C, while it is at 210°C in fixed bed reactors, and this results in overall higher conversion rates with the slurry-bed reactors. Iglesia [87] showed that the activity of Co catalyst towards FTS is directly proportional to the surface area. In this work, they tested particles with ranging sizes from 9 to 200 nm and reaction rate or turnover frequency per unit of active site was observed to be stable. This indicates that FTS is structure insensitive. Thereafter, this structure-activity relationship was studied by a number of authors [58, 75, 88–92]. These studies show that Co FTS is structure insensitive above the size of 8-10nm, but catalysts smaller than 8 nm show low TOF (seen in Figure 1.20).

When it comes to selectivity, Iglesia claims that there is no particle size-selectivity relationship within the range of 9-100nm [87]. Later, Barbier et al. reported that chain growth probability, α, increases from 0.74 to 0.87 as the catalyst size changes from 4.5 to

9.5 nm at 170°C, 1 bar [92]. In the study of Bezemer et al. the selectivity towards methane had increased sharply as the catalyst size gets smaller than 6 nm at 220°C and atmospheric pressure [58]. The size-selectivity relationship becomes more pronounced at high pressures. The C_{5+} selectivity increases as the catalyst size increase at the pressures of around 35 bar [75, 88, 89].

The fundamental knowledge on the size-activity and size-selectivity relationship is scarce. The explanation for size-selectivity relation is more than classical size effect of heterogeneous catalysis, which is based on the change of a fraction of different sites with the variation in size. The process of FTS includes different elemental reactions that occur simultaneously. It is suggested that relatively larger particles have the optimum combination of active sites for all these reactions and this causes higher selectivity towards longer chains [58]. Another idea is that the binding modes of CO differ as the size changes, and bridge-bonded CO is found to have higher dissociation rate, which leads to higher activity and this mode is preferred at larger Co particles [58, 92]. Prieto et al. reported an enhancement of $Co^{\delta+}$-SiO_2 sites due to flattening of the crystal caused by carbon-induces surface reconstruction at FTS conditions [89]. Another study proposed that the oxygen and carbon from dissociation of CO bind stronger to the surface of smaller particles and block the active sites [93]. More fundamental research is required to understand size effects on activity and selectivity.

Cobalt FTS catalysts generally show fast initial deactivation and then that starts to level off. As in the case of size effect little fundamental understanding of deactivation mechanism is present. B5 sites of cobalt metal are accepted to be the active site for FTS [53]. Hence the deactivation of Co catalyst is caused by the changes in these sites. Since FTS is a complex process and current techniques are limited to study certain sites, the scope of research on deactivation is limited to changes in the metallic surface area. Possible deactivation mechanisms proposed are oxidation, catalyst-support interactions, deposition of carbon, sintering, poisoning and surface reconstruction [15].

The oxidation of cobalt by the water thought to be one of the deactivation mechanisms. But recent studies claim the opposite. Studies show no oxidation of Co for particles larger than 2 nm and even further reduction is observed during the reaction [94–97].

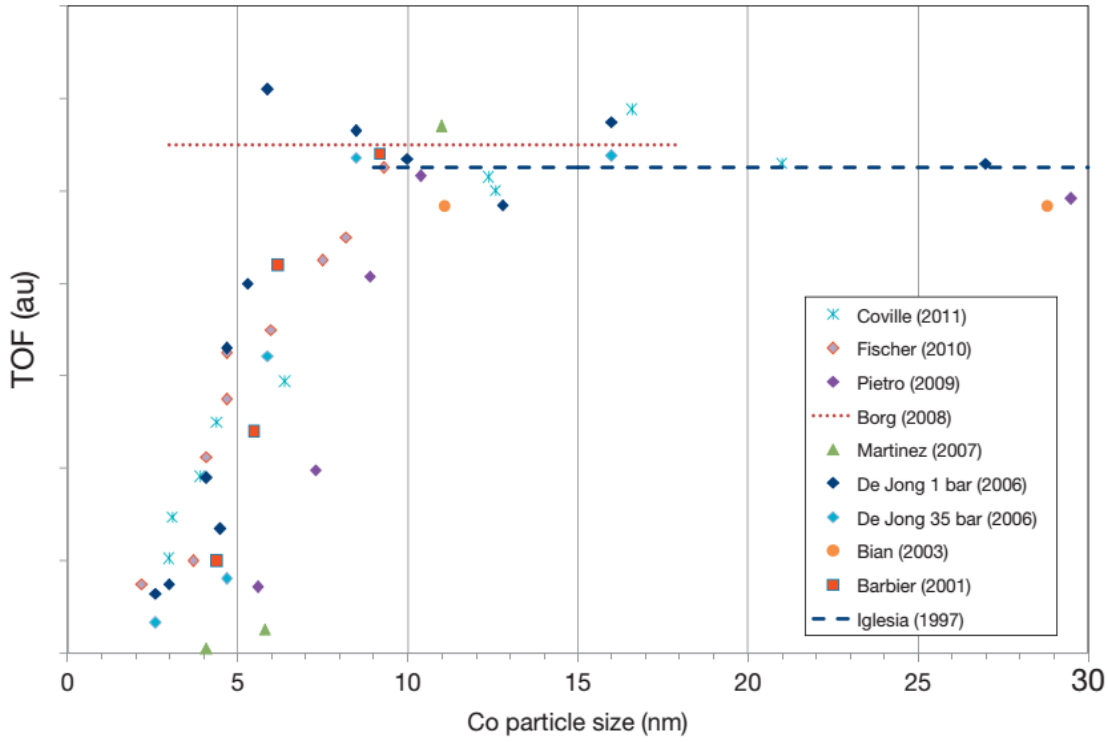


Figure 1.20. TOF-size relationship at FTS. Reprinted from [15], Copyright (2013), with permission from Elsevier.

Another source of deactivation considered to be was the formation of cobalt aluminate. This reaction is thermodynamically favored but this requires CoO formation as intermediate. As mentioned above, this is not observed in FTS conditions.

Deactivation by carbon deposition has many faces. One is the blockage of pores by long hydrocarbon products, this causes to mass transport limitations of reactants. This is partially being solved by treating the deactivated catalyst with hydrogen or washing it with a proper solvent. Another one is the formation of inactive polymeric carbon species such as graphene [98]. Carbon deposition problem is being suppressed by the addition of promoters such as ruthenium [62]or boron [65].

Sintering is the merge of smaller particles with higher surface energy to form larger particles with lower energy and it is thermodynamically driven. Increase in temperature and partial pressure of water boosts sintering. Support materials suppress such deactivation pathways. Alumina is a better choice when compared to silica, due to its stronger cobalt-support interactions.

Cobalt catalyst is known to be poisoned by S, NH_3, HCN, Hg, and Cl, especially at CTL processes [51, 53, 99–102]. Sulfur has high adsorption energy which causes irreversible poisoning and its electronic effect and size also poisons the adjacent active cobalt site. It is hard to remove and accumulates over time. Zinc-oxide or lead-oxide guard beds are employed to remove sulfur from syngas for prevention of poisoning. Poisoning of nitrogen-based compounds like NH_3 or HCN is not as severe as S-based chemicals, it can be reversed by mild hydrogen treatment [103].

Surface reconstruction, just like sintering, is thermodynamically favored and results in surfaces with lower energy that diminishes the activity. A model study suggests that the carbon dissociated from CO can cause the Co fcc (111) surface to change to Co (100)-like sites, which are less active towards FTS [104].

There are couple of methods to reverse the adverse effects of deactivation processes. Most widely used one is the application of consecutive reduction-oxidation cycles under hydrogen or steam [53, 105].

1.2.3. Mechanism and Kinetics

There are three classes of the mechanism proposed for FTS (shown in Table 1.1), in which the type of monomer differs in the prorogation step: carbide mechanism, enol mechanism, and Co insertion mechanism.

According to carbide mechanism CO first dissociates to carbon and oxygen atoms. Hydrogenation of carbon gives rise to the formation of CH_x species. And these bind to each other one by one. And the termination path of chain growth determines the type of end-product which might be an olefin, a paraffin or an oxygenate. The enol mechanism proposes partial hydrogenation of CO to form CHOH species. These give condensation reactions for the chain growth. Here the type of product is determined by the termination step, as well. In the CO insertion mechanism, carbon monoxide acts as the monomer and then it is hydrogenated, and its oxygen is removed.

Table 1.1. Most common reaction mechanisms that are proposed for FTS.

Steps	Carbide Mechanism	Enol Mechanism	CO Insertion Mechanism
Initiation	$CO \rightarrow C+O$ $O+2H \rightarrow H_2O$ $C+xH \rightarrow CH_x$	$CO+2H \rightarrow CHOH$	$CO+H \rightarrow H_3CO$ $H_3CO+2H \rightarrow H_2O+H_3C$
Propagation	$R+CH_x \rightarrow R\text{-}CH_x$ $R\text{-}CH_x+(2-x)H \rightarrow R\text{-}CH_2$	R-C-H+CHOH→ $R\text{-}C\text{-}COH+H_2O$ R-C-COH+H→ $R\text{-}CH_2COH$	$CH_3+CO \rightarrow CH_3\text{-}CO$ $CH_3\text{-}CO$ +H→ $CH_3\text{-}CH_2+H_2O$
Termination	$R\text{-}CH_2+H \rightarrow R\text{-}CH_3$ $R\text{-}CH_2\text{-}CH_2\text{-}H \rightarrow R\text{-}$ $H_2=CH_2$ R+CO→oxygenates	$R\text{-}CH_2COH+4H \rightarrow$ $R\text{-}CH_2\text{-}CH_3+H_2O$ $R\text{-}CH_2COH+nH \rightarrow$ oxygenates	$R\text{-}CH_2+H \rightarrow R\text{-}CH_3$ $R\text{-}CH_2\text{-}CO+nH \rightarrow$ oxygenates

The mechanism of FTS is still on debate and different approaches should be implemented to fully understand the fundamentals of its working principle such as model surface science experiments, DFT calculations, and microkinetic studies.

Surface science approach focuses on each elementary step of the whole process one by one. For that purpose, first, a well-defined single crystal surface of a catalyst material is prepared, then the adsorbate is presented to the surface at ultra-high vacuum to achieve a well-defined coverage. Then the surface is investigated by various techniques.

The most elemental step of FTS is the adsorption of CO and H_2 on the catalyst surface, and that is the easiest step to study by surface scientists. In a typical experiment, Co surface is exposed to CO with an increasing concentration at 180 K [106]. At first CO shows 0.33 ML (monolayer) coverage with a sticking coefficient of 0.7 and adsorption energy around 115 $kJmol^{-1}$. With increasing concentration, the coverage reaches to the values of around 0.65 ML. Any coverage above 0.33 ML leads to different binding modes of CO and desorption temperature falls due to repulsive interactions between CO molecules. Hydrogen shows surface coverage values around 0.5ML with low sticking coefficient and adsorption

energy of 33 kJmol^{-1} [107]. When the surface covered with hydrogen is exposed to CO, only 50% of adsorbed hydrogen remains on the surface and desorption temperatures fall about 100K due to the presence of CO. However, the interaction between of CO and surface is slightly affected by the presence of hydrogen. The combined outcome of these experiments is the proof of the existence of repulsive interactions between CO and hydrogen and this causes a barrier to the formation of H_xCO species.

In FTS, cleavage of the C-O bond is one of the key steps and not all sites of cobalt are able to break that bond. While Co (0001) surface is not active towards CO scission [106] after thermal desorption or longer exposure of CO at high temperatures carbon and oxygen species were observed at Co (1012) [108, 109], Co (1120) [110] sites and cobalt foils. UHV experiments with 2 nm cobalt catalysts showed activity towards CO scission, which is explained by the high density of defect sites [111]. These studies show that C-O bond cleavage is possible on Co but not on the most abundant surface, which is the closed-pack site.

To study the CO insertion mechanism, ethanol's behavior on cobalt closed-pack surface was investigated. It is observed that ethanol adsorbs to the surface as ethoxy species at 160 K and decomposes at 350 K giving rise to acetaldehyde as an intermediate. The energetic barrier for this process is 70 kJ mol^{-1} and oxygen and C_2H_x species were the end product of this experiment, which indicates C-O bond scission and that insertion of alky to CO facilitates the step [112].

When it comes to carbide mechanism, the stability of C_1H_x species plays a key role, since they are the monomers of the propagation step. In an experiment performed on cobalt foil [113], methane is dissociated to CH_3 and a hydrogen atom with the help of molecular beam. Then as the temperature increased CH_3 species are transformed into CH species, and it is mentioned that the closed pack surfaces of nickel and platinum follow the similar trends.

Investigation of reaction by DFT calculations is the relatively new approach in the area of heterogeneous catalysis [114, 115]. These models give insight into adsorption configurations, transition states, and their energetics. To validate these results from computational calculations, experimental data from surface science is required, but the

amount of experimental data is scarce, and the conditions of these experiments are not realistic since they are performed under ultra-high vacuum.

Calculations on dissociation of CO show that the activation energy for that step is 109 kJ mol^{-1} on (100) surface of bcc-iron [116, 117], where the reported experimental data is 110 kJ mol^{-1} [118]. This activation energy corresponds to reaction temperatures of 400-450 K. (110) surfaces show activation barriers around 146 kJ mol^{-1} which indicates that this site is inactive towards CO scission at FTS conditions. Some studies reported that hydrogen assisted C-O bond breaking is easier [119–121], but the formation of CHO species also require energy [120]. On surfaces such as Co(0001), Fe(110), Hägg carbide (100), that have lower activity towards CO dissociation, hydrogen assisted pathway is energetically favored over direct dissociation [119, 121].

Nørskov group estimated the energetics of each step of a possible pathway for methane formation on different metals [122]. According to Sabatier Principle, the adsorption energies of intermediates should be moderate for an optimum catalysis [123]. The metals highlighted with the green in Figure 1.21 seems to be the best candidates among others for this reaction.

A computational study on carbide mechanism suggests that C_xH_y monomer species with less hydrogen is energetically more favored for the chain growth reaction [124]. Zhuo et al. proposed a CO insertion mechanism based on DFT calculations, where CO inserts to adsorbed CH_2 species and then gets hydrogenated to give C_2 intermediate and another CO insertion follows the process [125].

Even though FTS is originally used to convert coal to liquid fuel, it has the potential for wider applications. Conversion of any carbon feedstock to functional chemicals from fuels to chemicals for industry. BTL and GTL can take part in the reduction of CO_2 emission. Even though CTL might be an alternative for this purpose along with CO_2 sequestration systems. This process would play a role in the utilization of CO_2 as the technology on the reduction of carbon dioxide proceeds. For that purpose, along with the industry, more interdisciplinary academic work on the mentioned issues is needed.

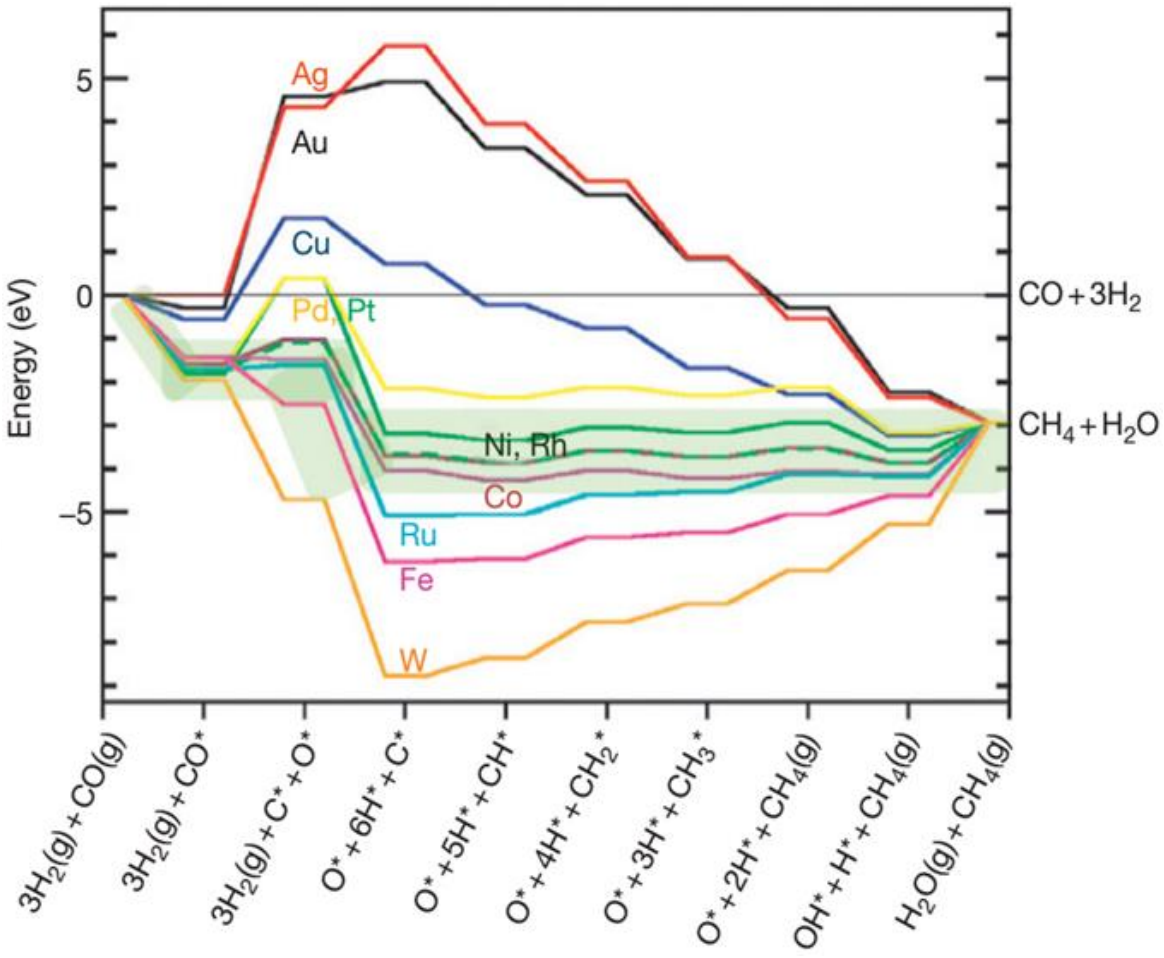


Figure 1.21. Energy profile obtained by DFT calculations for methane formation reactions on various metal surfaces.

1.3. Bimetallic Nano-Structures

Mixing different metals to have improved properties are known for a couple of thousands of years. These systems enhance chemical properties as well as mechanical ones. A most common example is stainless steel, an alloy of chromium, carbon, and iron which is prone to oxidation in its elemental form. This phenomenon is not specific to bulk materials, of course. Access to information about materials at nano dimensions brought up new fundamentals such as size-shape-property relationships for various applications, ranging from catalysis to optoelectronics. Presenting different metals to the nanocrystals also play a crucial role in their operation.

1.3.1. The Architectures of Bimetallic Nanocrystals

Besides the choice of metals, the arrangement of atoms also changes the characteristics of the crystals. The architecture of particles seen in Figure 1.22 is determined both by thermodynamic parameters such as atomic radii, lattice parameters, and atomic interactions; and also kinetic effects [126–129].

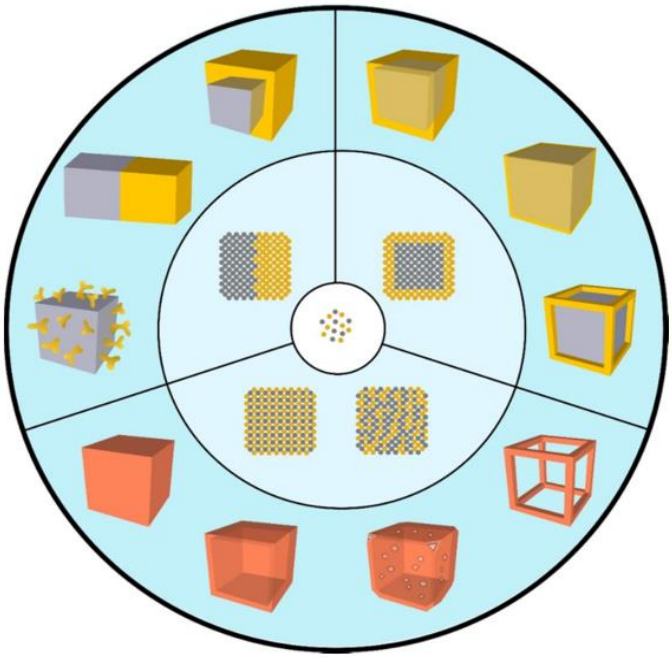


Figure 1.22. Possible architectures of bimetallic nanoparticles. Reprinted with permission from [138]. Copyright (2016) American Chemical Society.

1.3.1.1. Alloys and Bimetallic Compounds. Alloying metals to obtain superior properties is a well-known phenomenon. To understand the fundamentals on the role of size and composition, well-established synthesis methods are a must. Mostly used methods are co-reduction and thermal decomposition of metal precursors. From the perspective of thermodynamics, to achieve the mixing of metals the interaction between the atoms of different metals should be greater than the one between the atoms of same metals, the lattice parameters -such as crystal structure and lattice constant- should be similar and they must have similar surface energies [130]. But playing with conditions related to the kinetics can help to overcome thermodynamic equilibrium states. Synthesis of Au-Ag alloys at low temperatures prevents the atoms to diffuse thermodynamically stable positions and lead to core-shell structures. One should heat these particles to obtain alloys [131].

Some bimetallic systems, such as Au_3Cu or $PtNi_2$, form distinct lattice structures from their individual states, and they obtain a well-defined stoichiometry. This behavior is again derived by thermodynamics, but they require annealing to transform from alloy to intermetallic state. They are superior to alloys in some applications like catalysis, even though the atomic ratios are the same and control over composition and surface structure is easier in such systems [132].

1.3.1.2. Core-Shell Nanoparticles. Bimetallic core-shell nanoparticles are structures that have a metallic coating on another metal. Seed-mediated growth is the most common synthesis method to obtain such structures. The term "seed" refers to the metal nanoparticle which is the growth site of the other metal atoms that are generated by the reduction or decomposition of their precursor salts. Implementing precious catalyst metals as shell material is a clever way to minimize cost without sacrificing surface area. Besides, the thickness of the shell is a definitive parameter on the properties of core-shell nanoparticles, as it decreases, enhancements in the electronic coupling and strain effects boost the catalytic properties of these materials. Also, as the thickness varies the chemical and thermal stabilities, as well as optical properties of them, changes [133].

1.3.1.3. Hollow Structures. This kind of architectures, such as nanocages and nanoboxes, have highly open structures with optical tenability. These properties are exploited by advanced applications like drug delivery, photothermal cancer therapy, and sensing [134–136]. Especially nanocages obtain high porosity, which facilitates encapsulation and release of molecules. Also, the high surface area to mass ratio provides high catalytic activity [137]. These structures can be synthesized by selective etching of core material from core-shell nanoparticles, or by galvanic replacement.

1.3.1.4. Core-Frame Structures. Core-frame nanocrystals consist of a well-defined core crystal, where its corners and edges are covered by another metal. Such structures help nanocrystals to conserve their shapes, edges, and corners at elevated temperatures. Also, they provide a high number of atoms with low coordination number in a small area, which enhances catalytic activity. Synthetic approaches are kinetically controlled deposition of secondary metal atoms on corners and edges of a seed particle, where the surface free energy is relatively higher; and galvanic replacement to a lesser extent.

1.3.1.5. Dendritic and Heterostructured Nanocrystals. Aforementioned structures are the most common ones among the bimetallic structures. But there are myriad of architecture types including dendritic structures, such as highly branched nanocrystals, multipods, stars, pentacles, flowers etc., and heterostructured forms, like dimers, dumbbells, Janus particles and so on [131, 138]. Dendritic nanostructures can be synthesized by kinetically controlled (the rate of the deposition should be much higher than the surface diffusion) seed-mediated growth, galvanic replacement, anisotropic etching or by merging different nanostructures. These particles provide a high surface to volume ratios and high density of atoms with low coordination number, which are the properties required for catalysis. Also, tips of needle-like structures help to generate strong electric field upon resonance excitation, which is a key factor for optical applications like surface-enhanced Raman scattering (SERS) [138].

Heterostructured nanocrystals are formed through the union of two different nanoparticles at an interface. Kinetic control over the seed-mediated growth is the key parameter to achieve their synthesis. These are being implemented in photocatalytic applications since they provide two different surfaces for two different reaction steps.

1.3.2. Synthetic Approaches

There is an immense number of studies on the synthesis of bimetallic nanoparticles with well-controlled structures. Most common synthesis methods fall into four main classes: co-reduction, thermal decomposition, seed-mediated growth, and galvanic replacement. These approaches are also being combined to achieve more complex structures.

1.3.2.1. Co-reduction. Co-reduction method is generally used to synthesize alloy and intermetallic nanoparticles. The precursor salts of two metals (M1 and M2) are reduced simultaneously to obtain zerovalent atoms and these first nucleate, then grow to form M1-M2 nanoparticles. Post-annealing might be necessary to achieve the thermodynamical equilibrium state. Generally, the control over the composition and geometry is maintained with the help of several factors such as reduction potentials of metal ions, the strength of reducing agent, the precursor ligand, surfactant and reaction conditions. But the synthesis of alloys from metals with big differences in redox potential, crystal structure, surface energy, cohesive energy and melting point is very difficult.

To obtain alloys, reduction potentials of the metals should be close to each other, otherwise, the one with higher reduction potential would be reduced first and form a nanocrystal right away. In that case, the other metal can diffuse into that nanoparticle and would form a shell around the seed. But one can overcome this problem by varying the feeding rates of the precursor salts. The metal with lower reduction potential should be higher in concentration to compensate for the rate of reduction.

The ligands have a dual role in the synthesis of nanoparticles. First, they alter the actual reduction potential of the metals. For example, gold-halide complexes have the following order in reduction potentials: $[AuCl_4]^-$ > $[AuBr_4]^-$ > $[AuI_4]^-$. Secondly, these ligands can attach to certain sites of the seeds and change the mode of growth. This leads to nanoparticles with different geometries.

Surfactants are, without a doubt, one of the most important factors in controlling size and shape of nanoparticles. They bind selectively to certain sites of the particles, which dictate the anisotropy in surface energy and subsequent growth consequently. These surface capping agents can be polymers, like polyvinylpyrrolidone (PVP), polyethylene glycol (PEG) and their derivatives; amphiphilic molecules with C_{10-20} hydrocarbon tail such as oleic acid (OA), oleylamine (OLA); or small anions like halide ions, $C_2O_4^{2-}$. Along with these factors, timing in addition of reagents, the solvent, temperature and relative concentrations are definitive on the synthesis of bimetallic nanoparticles.

1.3.2.2 Thermal Decomposition. Along with mono- and bimetallic nanocrystals, this method is also being implemented for the synthesis of semiconductor and metal oxide particles. It is generally being used to synthesize metals with relatively lower reduction potentials, such as iron (Fe), cobalt (Co) and nickel (Ni). Acetylacetonate and carbonyl salts of metals are the most common precursors for this approach. The key parameters for the co-reduction method apply here, too.

To obtain alloys, the decomposition temperatures of both precursors should be similar, otherwise, core-shell structures form, and this is being exploited to synthesize core-shell structures through a one-pot process. There are ways to overcome this struggle such as employing a reducing agent or using bimetallic precursors [139, 140].

1.3.2.3. Seed-Mediated Growth. As mentioned before, seeds provide sites for secondary metal atoms to adsorb and grow. This approach is the most common synthesis route of well-defined bimetallic structures.

In the synthesis of nanoparticles as the monomers (atoms) are generated from the precursor salts through reduction or decomposition, they start to form seeds right after they reach a certain concentration (supersaturation) seen in Figure 1.23 [141]. And seeds start to grow right away by adsorption of monomers on these seeds. The concentration required for the growth process is lower than the supersaturation. That is why the concentration of the precursors should be kept under a certain level to avoid self-nucleation of shell material. To obtain seeds with the similar size the nucleation phase should be fast, which can be controlled by the strength of the reducing agent and the temperature. The concentration is also a key parameter to control shell thickness, shape, and size.

Seeds with different shape and size have various sites that have anisotropy in their surface energies. This affect the pattern of growth and result in different structures. Hence, to synthesize a desired bimetallic nanoparticle, first, a well-defined seed must be prepared, and this is again a function of surfactant, precursor, solvent, temperature among others.

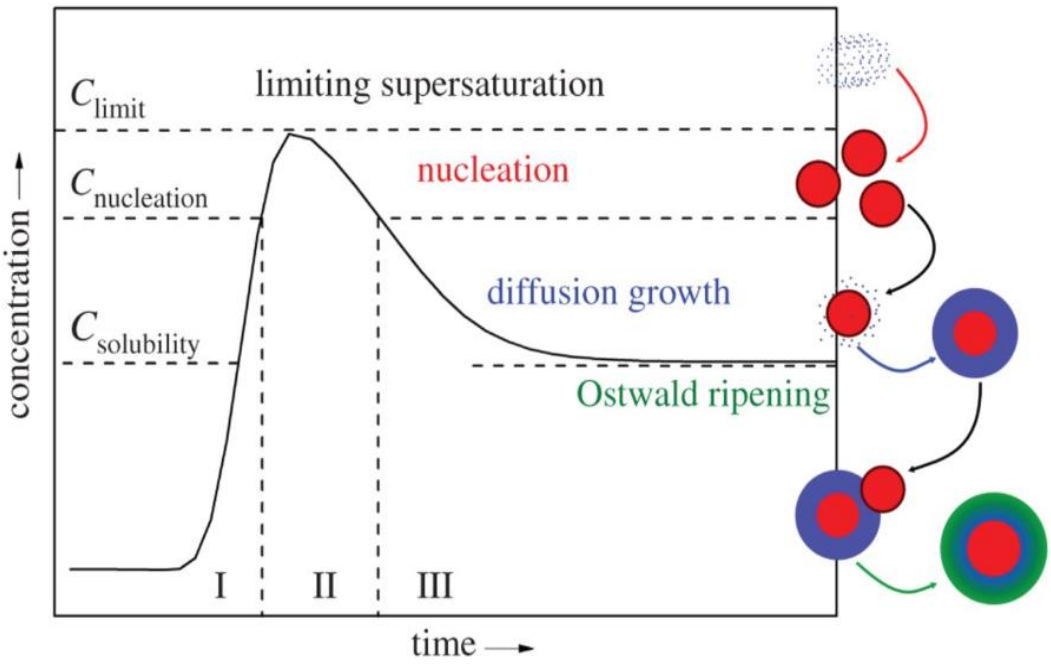


Figure 1.23. LaMer Diagram for the generation of nanoparticles.

There are three modes of growth of secondary metals on seeds as seein in Figure 1.24: layer by layer deposition (Frank-van der Merwe), island formation (Volmer-Weber), and the mode that consist of conversion from Frank-van der Merwe to Volmer-Weber (Stranski-Krastanov) [138]. The modes are dictated by the parameters of the surface adsorption rate, surface diffusion rate, surface energy, inter-/intra-metallic bond strengths, the lattice constant, crystal structure among others. For example, metals that have a vast difference in their lattice parameters prefer Volmer-Weber type growth, especially when the secondary metal atoms have strong M2-M2 interactions because this hinders the surface diffusion of the atoms. Employing these growth modes helps to obtain a wide variety of bimetallic nanostructures ranging from core-shells to dendritic structures.

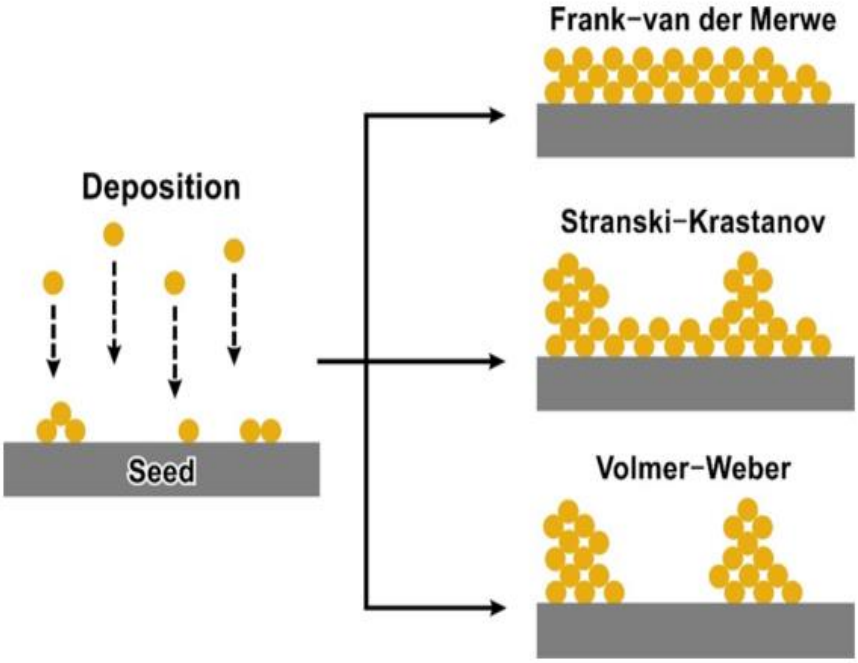


Figure 1.24. Growth modes in the seed-mediated growth process. Reprinted with permission from [138]. Copyright (2016) American Chemical Society.

1.3.2.4. Galvanic Replacement. Galvanic replacement an exceptional method to synthesize nanostructures that cannot be possible in another way such as hollow structures [142]. This relies on oxidation of atoms that are presented on a nanostructure, and its electrons reduce a metal with a higher reduction potential. Throughout this process, the reduced metal atom adsorbs to the nanoparticle, where the oxidized one leaves. Anisotropies in surface energies of different sites dictate the path of this event. Also, crystal parameters play an immense

role. If the lattice constant of the seed is larger, the incoming atoms most likely diffuse into the seed to form an alloy. To avoid that the seed should have a relatively small lattice constant. Another important parameter is the possible oxidation states of the metals. Since the ratio of oxidation states will determine how many atoms required to reduce incoming cation and this will affect the kinetics and shape consequently.

In some cases, galvanic replacement is not desired, as for the case of core-shell synthesis. To avoid that, the ligand of the precursor can be changed to adjust actual reduction potential or boost the rate of reduction by adding bases like NaOH or employing strong reducing agents so that the rate of deposition exceeds the rate of galvanic replacement [143].

1.3.3. Catalytic Properties of Bimetallic Nanoparticles

According to Sabatier principle, the adsorption energies of reactants to the catalytic surface should have an optimum value. Building on this idea, Balandin has plotted the trend in catalytic activity as a function of the heat of adsorption, which is named as volcano plot. And lately, Brønsted-Evans-Polanyi (BEP) theorized the role of position and with of the d-band of metals on their catalytic activity The tip of the curve shows the optimum adsorption energy required for the best catalytic activity [144].

The surface energies of nanoparticles are a function of composition, shape, and size. By changing these parameters, one can obtain the optimum adsorption energy and catalytic performance consequently. Presenting a second metal bring some unprecedented features such as new atomic ensembles, change in the electronic structure of surface atoms by charge transfers between two metals and a new arrangement of surface atoms due to strain effects, geometry and size.

Charge transfer between two metals happens from the metal with higher Fermi level to the other. So, one can adjust the electronic structure and Fermi level of the active metal and surface energy consequently, which is crucial for the catalytic activity, as mentioned before.

In core-shell nanoparticles, if there is a mismatch of lattice constant, core metal induces strain on the shell. If the lattice constant of the core is smaller than the one of the shell, there occurs a compressive strain. So, the atoms of shell metal tend to get closer to each other and that decreases the surface energy. To increase the adsorption energy of the metal on the shell, a metal with larger lattice constant should be employed in the core to cause tension. In addition, the strength of the strain can be tuned with a variation of the shell, it decreases as the shell thickness increases.

As a conclusion, bimetallic nanoparticles are strong tools to enhance catalytic activities through their unique properties to electronic and geometric structures. However, there are myriad of possibilities in composition and architecture. This requires new standardized synthesis approaches and advanced characterization techniques along with multidisciplinary studies involving computational modelings.

1.4. Aim of the Study

Richard Smalley, who has a Nobel Prize in chemistry for the discovery of fullerenes, claims that in the list of humanity's problems in next 50 years, energy is going to be the most problematic one. Conventional energy sources are being drained day by day and even this was not the case, their adverse effects to the environment and climate make them unpractical for the long run. The carbon dioxide level in the atmosphere is already above the critical limits. So, there is an urgent need for alternative energy sources, which do not release carbon dioxide and even employ it to convert to useful chemicals. FT technology is a promising candidate for this approach. Its versatility and possible synergic applications with CO_2 reduction technologies are important factors that is worth the attention of academy and industry.

Colloidal science has made a great progress in the synthesis of nanoparticles with well-defined size, structure, and compositions. And these newly established structures show advanced performance in applications ranging from catalysis to optics. Yet, there is a myriad of possibilities for improvement of the synthesis and applications.

For these reasons, the scope of this thesis is focused on creating a library of bimetallic core-shell nanoparticles with different elemental compositions. Primary goal of this study is to synthesize core-shell structures with tin (Sn) in the core and catalytically active Co, Fe or their alloy on the shell. This architecture has many aspects regarding the catalytic activity. First, it decreases the amount of catalytic element without sacrificing from the surface area which is crucial especially for the applications that involve noble metals. Secondly, the core material can enhance the activity through strain and ligand effects. The main reasons why tin is chosen as the core metal can be counted as follows: First, it has a number of different oxidation states which can contribute to the reaction steps that involves reversible oxidation processes. Secondly, it would change the electronic structure of the surface metal through charge transfers, which is crucial for heterogeneous catalysis. Last but not least, tin has relatively large lattice constants compared to cobalt and iron, so it would induce strain on the shell, which would modify the atomic arrangement and catalytic activity consecutively.

Chapter 1 comprise of general knowledge on heterogeneous catalysis, FTS, and bimetallic nanostructures. In Chapter 2 experimental procedure of the study and working principle of the characterization techniques are explained and discussion is made in Chapter 3 referring to acquired results from analysis techniques. Conclusion remarks on the synthesis and characterization of nanoparticles are in Chapter 4 and the future work of this study is mentioned in Chapter 5.

2. EXPERIMENTAL

2.1. Reagents

Chemicals and materials, used for the synthesis of bimetallic nanoparticles, are listed in Table 3.1.

Table 3.1. Chemicals and materials used in this study

Name	Supplier	Purity or Noted
$SnCl_2$	Alfa-Aesar	98%
$CoCl_2.6H_2O$	Alfa-Aesar	98%
$FeCl_2.4H_2O$	Alfa-Aesar	98%
$CuCl_2.2H_2O$	Acros Organics	99%
H_2PtCl_6	Sigma-Aldrich	ACS
Triethylene Glycol	Fischer Scientific	purified
Polyvinylpyrrolidone	Alfa-Aesar	M.W. 58000
$NaBH_4$	Alfa-Aesar	98%
Acetone	Sigma-Aldrich	ACS
Ethanol	Sigma-Aldrich	ACS
tert-Butylamine	Sigma-Aldrich	98%
NaOH	Sigma-Aldrich	99%
Oleic Acid	Sigma-Aldrich	99%
Sodium Oleate	TCI	97%

2.2. Synthesis of Bimetallic Nanostructures

2.2.1. Synthesis of Tin Seed Nanoparticles

For the synthesis of tin nanoparticles, first 36 mg (0.019mmol) of $SnCl_2$ and 210 mg polyviniylpyrrolidone (PVP) were dissolved in 9 ml triethylene glycol (TEG) in a 50 ml-two necked round bottom flask. While these were dissolving, the mixture was purged with

argon gas for 30 minutes to get rid of oxygen in the medium and the rest of the experiment is performed under argon atmosphere at 50°C with vigorous stirring (1200 rpm). In a separate vial, 55 mg $NaBH_4$ was dissolved in 1 ml TEG. As $NaBH_4$ is dissolved completely, it was taken via a syringe and injected to the reaction mixture with a rate of 1ml/min. As the first drop of the reducing agent meets the colorless solution, its color is turned into a very dark brown, and the occurrence of bubbles was observed. After one hour of reaction time, 1 ml of the sample was taken and 25 ml of acetone was added on top of it in a centrifuge tube. After 10 minutes of sonication, it was centrifuged at 5500 rpm for 5 minute and the supernatant was discarded. The precipitate was dispersed in 2 ml of TEG, then 25 ml of acetone was added and sonicated for 10 minutes and centrifuged at 5500rpm for 5 minutes. This washing step was performed three times to get rid of excess reactants and side products. After that, the precipitate was washed 2 times only with acetone to get rid of TEG, which is not volatile, and this is problematic for the characterization techniques performed in vacuum. Finally, the product is dispersed in 10 ml of ethanol, if it is going to be characterized. If the product is going to be used as a seed for the growth of shell metal, it is dispersed in 10 ml of TEG.

2.2.2. Synthesis of Sn@Co Nanoparticles

First as prepared tin nanoparticles, dispersed in 10 ml of TEG, were added in a 50 ml-two necked round bottom flask. Then 66 mg of PVP was dissolved in it while being purged with argon at 50°C with vigorous stirring (1200 rpm). In a vial, 55 mg of $NaBH_4$ was dissolved in 2 ml TEG and added to the round bottom flask. In another vial 2.5mg (0.001 mmol) $CoCl_2.6H_2O$ was dissolved in 4 ml TEG and this was injected to the reaction flask with a rate of 4 ml per 30 minutes. After one hour of reaction time, the solution was distributed equally in two centrifuge tubes and 25 ml acetone was added on top of each and centrifuged for 10 minutes at 7000 rpm. The supernatant was discarded, the precipitates were dispersed in 2 ml TEG and combined in a centrifuge tube. Then, 25 ml of acetone was added and sonicated for 10 minutes and centrifuged at 7000rpm for 10 minutes. This washing step was performed three times to get rid of excess reactants and side products. After that, the precipitate was washed 2 times only with acetone and the final precipitate was dispersed in 10 ml of ethanol.

2.2.3. Synthesis of Sn@Fe Nanoparticles

First as prepared tin nanoparticles, dispersed in 10 ml of TEG, were added in a 50 ml-two necked round bottom flask. Then 66 mg of PVP was dissolved in it while being purged with argon at 50°C with vigorous stirring (1200 rpm). In a vial, 55 mg of $NaBH_4$ was dissolved in 2 ml TEG and added to the round bottom flask. In another vial 2.1 mg (0.001 mmol) $FeCl_2.4H_2O$ was dissolved in 4 ml TEG and this was injected to the reaction flask with a rate of 4 ml per 30 minutes. After one hour of reaction time, the solution was distributed equally in two centrifuge tubes and 25 ml acetone was added on top of each and centrifuged for 10 minutes at 7000 rpm. The supernatant was discarded, the precipitates were dispersed in 2 ml TEG and combined in a centrifuge tube. Then, 25 ml of acetone was added and sonicated for 10 minutes and centrifuged at 7000rpm for 10 minutes. This washing step was performed three times to get rid of excess reactants and side products. After that, the precipitate was washed 2 times only with acetone and the final precipitate was dispersed in 10 ml of ethanol.

2.2.4. Synthesis of $Sn@Co_{0.5}Fe_{0.5}$ Nanoparticles

First as prepared tin nanoparticles, dispersed in 10 ml of TEG, were added in a 50 ml-two necked round bottom flask. Then 66 mg of PVP was dissolved in it while being purged with argon at 50°C with vigorous stirring (1200 rpm). In a vial, 55 mg of $NaBH_4$ was dissolved in 2 ml TEG and added to the round bottom flask. In another vial, 1.3 mg $CoCl_2.6H_2O$ and 1.1 mg $FeCl_2.4H_2O$ was dissolved in 4 ml TEG and this was injected to the reaction flask with a rate of 4 ml per 30 minutes. After one hour of reaction time, the solution was distributed equally in two centrifuge tubes and 25 ml acetone was added on top of each and centrifuged for 10 minutes at 7000 rpm. The supernatant was discarded, the precipitates were dispersed in 2 ml TEG and combined in a centrifuge tube. Then, 25 ml of acetone was added and sonicated for 10 minutes and centrifuged at 7000rpm for 10 minutes. This washing step was performed three times to get rid of excess reactants and side products. After that, the precipitate was washed 2 times only with acetone and the final precipitate was dispersed in 10 ml of ethanol.

2.3. Characterization of Nanoparticles

The characterization of nanoparticles was performed by HRTEM, XRD, and XPS techniques. HRTEM experiments were employed to obtain information about particle size, geometry, and architecture. XRD and XPS were employed to determine the crystal structure and elemental composition.

2.3.1. Transmission Electron Microscopy (TEM)

Transmission electron microscopy (TEM) is a powerful tool to characterize the structure and morphology of nanoparticles. It has the potential of giving details about size, shape and assembly in atomic resolution. In this thesis study, contrast between the metals in core and shell has helped to point core-shell structure.

For characterization, nanoparticles were dispersed in ethanol with a very low concentration and that was drop-casted on a carbon-coated copper TEM grid. HRTEM analysis of seed nanoparticles was conducted with JEOL 2100 JEM HRTEM device within TUBITAK MAM. And the characterization of core-shell nanoparticles was performed at UNAM, Bilkent University.

2.3.2. X-Ray Diffraction (XRD)

X-Ray Diffraction is a technique to investigate the crystal structure of materials. It is based on constructive interference of the rays and sample. Monochromatic, collimated X-rays that are generated by a cathode ray tube. If the sample satisfies the conditions of Bragg's law, constructive interference occurs. And the diffracted X-rays are being detected and the data is being converted to d-spacing, which is unique for each material. However, samples with small crystalline size cause peak broadening in XRD, and that makes the investigation of nanoparticles problematic.

X-Ray Diffraction (XRD) analyses were conducted with Rigaku D/MAX-Ultima+/PC Diffractometer using Cu-Kα radiation (λ=1.54056Å) at Boğaziçi University Advanced Technologies Research and Development Center.

2.3.3. X-Ray Photoelectron Spectroscopy (XPS)

X-Ray Photoelectron Spectroscopy (XPS) is a powerful tool to investigate elemental composition and oxidation states of surface atoms. It is based on the measurement of kinetic energies of electrons that are kicked from surface atoms by an incident monochromatic X-ray. The resulting intensity in the peaks and binding energy provides detailed information about the elemental composition of the sample.

XPS experiments were performed by Thermo Scientific K-Alpha Surface Analysis instrument at Boğaziçi University Advanced Technologies Research and Development Center. Al K Alpha X-Ray source with a spot size 400 μm was utilized. The step scanning was carried out from 0 to 90 degrees while measuring.

3. RESULTS AND DISCUSSION

3.1. Transmission Electron Microscopy (TEM) Results

Transmission electron microscopy (TEM) experiments were performed to gather information about the size, shape and morphology of the synthesized nanoparticles. Contrast in different layers of nanoparticles is planned to be used as a proof for core-shell structures. Size histograms of nanoparticles were obtained from TEM images to acquire information about size distribution of nanoparticles and to track change in size with the formation of shells.

The TEM image of as-prepared tin nanoparticles in Figure 3.1 shows that the synthesis protocol results in particles with an average diameter of 6.3 nm. The histogram displayed in Figure 3.2 consists of data that are taken from 178 particles from the Figure 3.1. As seen in the size histogram, as-synthesized Sn NPs are not monodispersed. According to LaMer model mentioned in Chapter 1, to obtain nanoparticles with same size the initial generation and consumption (nucleation) step should be very fast so that only growth step occurs after nucleation. This phenomenon is generally mentioned as separation of nucleation and growth. If they happen simultaneously first seed particles becomes bigger compared to the seeds occurred later. This is generally achieved at reaction temperatures above 200°C to boost the reduction and nucleation rate. Also, the choice of reducing agent plays a key role. Another crucial parameter is the type of precursor. Finally, choice of the surfactant and its concentration is very important, which dictates shape and size. One of the best examples for the synthesis of monodisperse Sn NPs implement modification of $SnCl_2$ with $LiN(SiMe_3)_2$ and oleyl amine and reduction of the obtained precursor with DIBAL [145]. Increasing the pH would help to increase the reduction rate and rate of nucleation consequently.

The lattice fringe in Figure 3.3 with the dimension around 0.3 nm indicates the (113) surface of SnO_2. The obtained size of Sn nanoparticles that are going to be used as seed for the growth of the shell is favorable since it is known that FTS catalysts, especially cobalt catalysts, has the optimum activity with the size around 8 nm [58, 75, 88-92]. So, with these

seeds, the core-shell nanoparticles with shell thickness around 1-2 nm would have high activity with minimum catalytic metal loading.

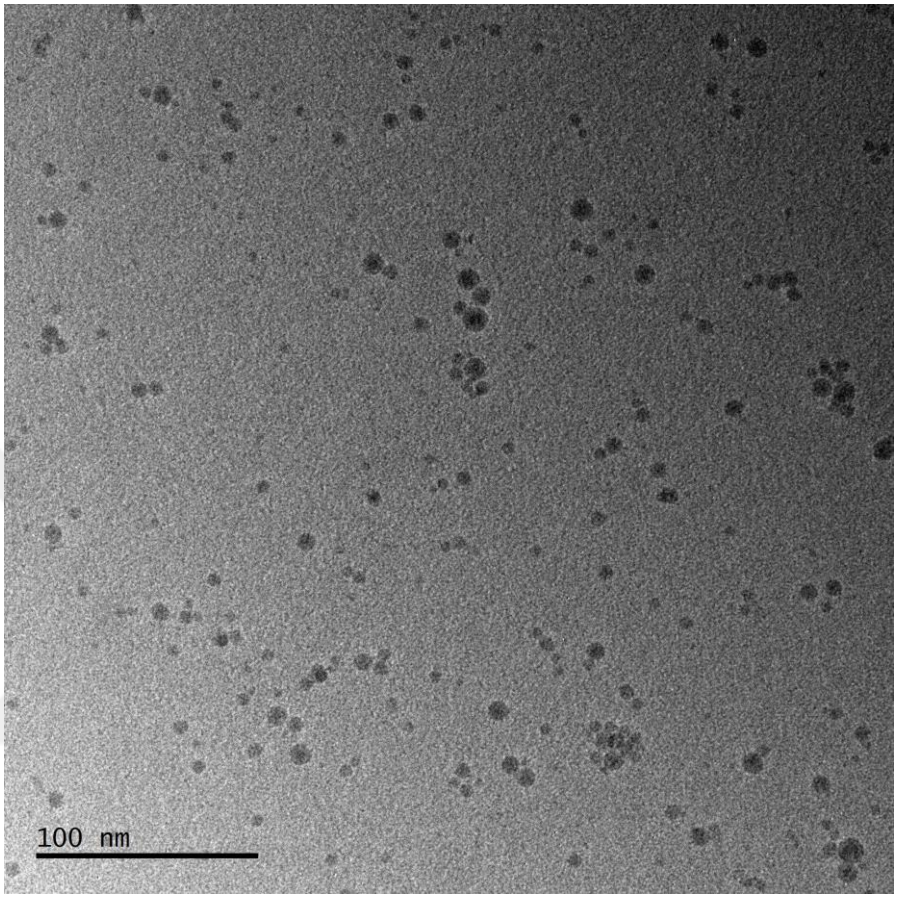


Figure 3.1. TEM image of as-prepared Sn nanoparticles.

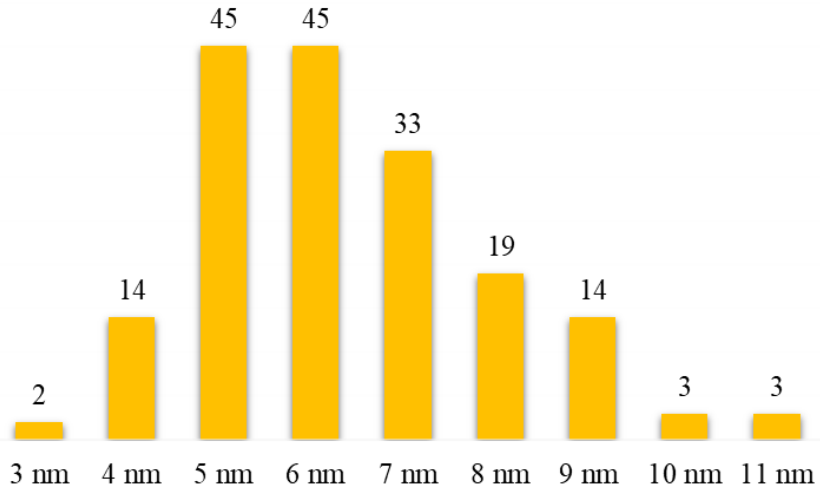


Figure 3.2. Size histogram of Sn nanoparticles. Numbers over the bars indicate the number of NPs with the same size.

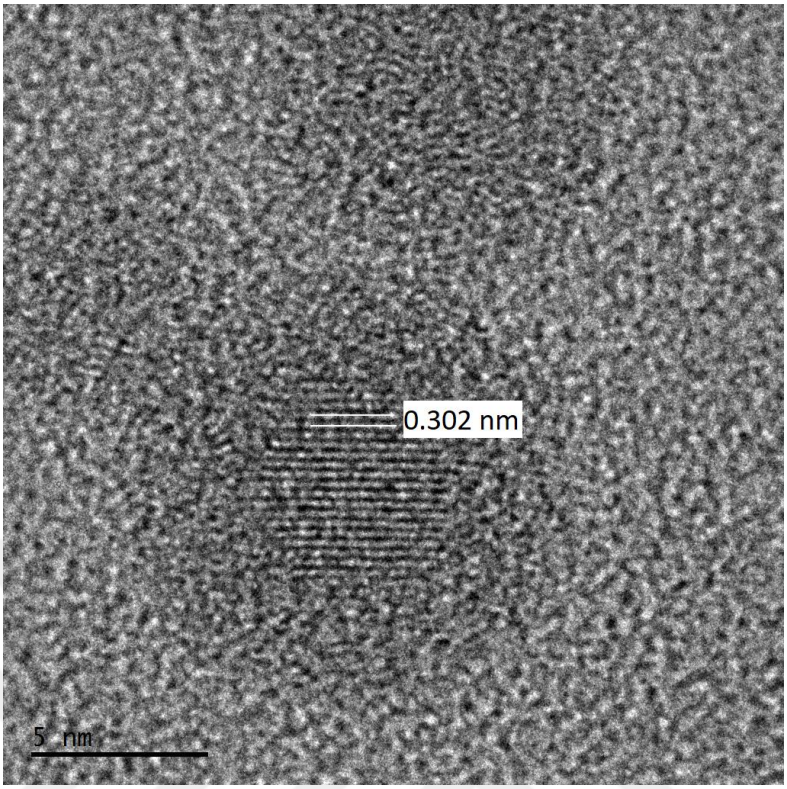


Figure 3.3. Lattice fringe of Sn nanoparticle.

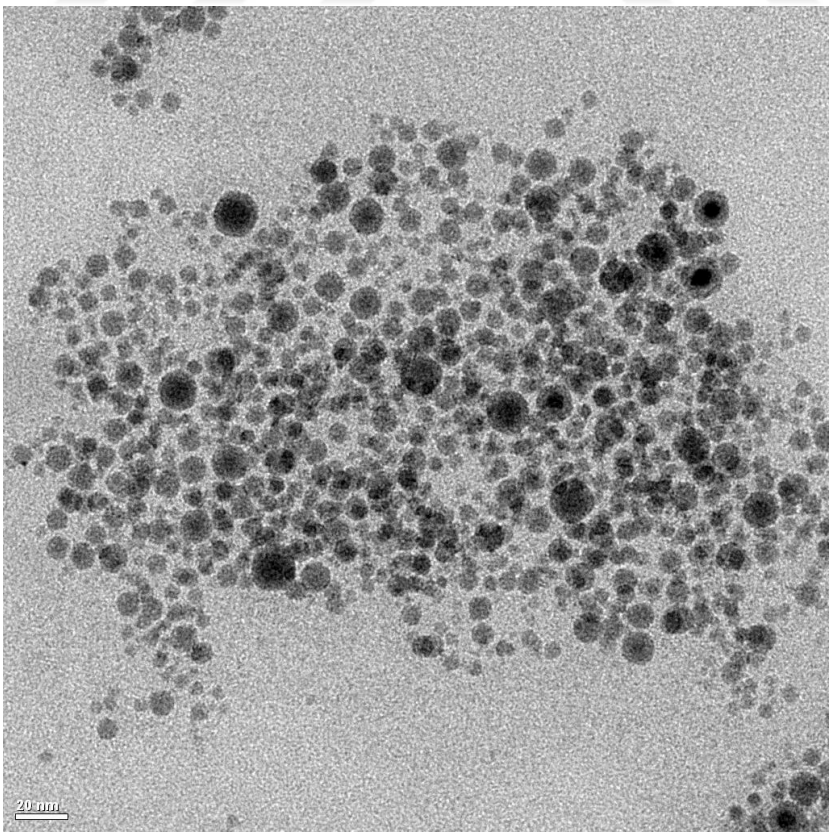


Figure 3.4. TEM image of Sn@Fe core-shell nanoparticles.

In the case of Sn@Fe nanoparticles, the core-shell structure is clear (seen in Figure 3.4), yet the number them is relatively low. This can be interpreted as follows:

(i) The particles that do not seem to be core-shell nanoparticles, might have relatively thin shells so the contrast in the image is not so strong to pick. In this case, an electron microscope with higher resolution and capability of elemental analysis is needed. And to obtain thicker shells, one should increase the amount of the precursor of the metal in the shell, without increasing the concentration to avoid self-nucleation.

(ii) Iron and tin might form alloyed structures rather than core-shell nanoparticles and this is an expected behavior due to the large lattice constant of Sn. For a conformal growth lattice mismatch should be less than 5%, the electronegativity of the core metal should be higher and M1-M1 and M2-M2 bond energies should be higher than M1-M2 bond energy [146]. But there are many exceptions that disobey these rules and there are ways to overcome [138]. The formation of Sn-Co and Sn-Fe alloys is a known fact and these compounds being exploited for Li-ion battery applications [147]. This problem might be overcome with kinetic control, such as increasing reduction rate of iron by using a stronger reducing agent, increasing the basicity of the medium or the temperature. Another solution might be the oxidation of the tin nanoparticles before the growth of secondary metal.

(iii) The amount of the iron precursor might be lower than required. In this case, the amount of the precursor should be increased without increasing the concentration to suppress self-nucleation of iron.

(iv) Iron might have self-nucleated instead of growing on the tin surface. According to LaMer model, this happens if the concentration of the monomers reaches to a certain concentration seen in Figure 1.23. This might be alleviated by the dilution of the iron precursor solution and decreasing the rate of injection of it.

The histogram of Sn-Fe nanoparticles in Figure 3.5 shows a shift towards larger sizes compared to seed particles. This indicates the growth of seed particles by the iron atoms and growth of particles with Ostwald ripening where two or more NPs becomes one and the occurrence of this process generally increases with time. High concentration of surfactants

might alleviate this problem. The average size of these bimetallic particles is around 7.3 nm which is 1nm thicker than Sn NPs. This corresponds to 9 atomic layers of iron if it is in metallic state. But the TEM image (seen in Figure 3.4) shows heterogeneity in the thickness of nanoparticles. The thickness of the shell can be controlled by the amount of precursor. Some kinetic control is also required for homogeneous shell formation, which can be achieved by temperature increase. Otherwise, thermodynamically favored phases or structures may form. In this case once the shell is formed the atoms would prefer that site and shell of that particle gets thicker while some of the seed NPs remain "naked".

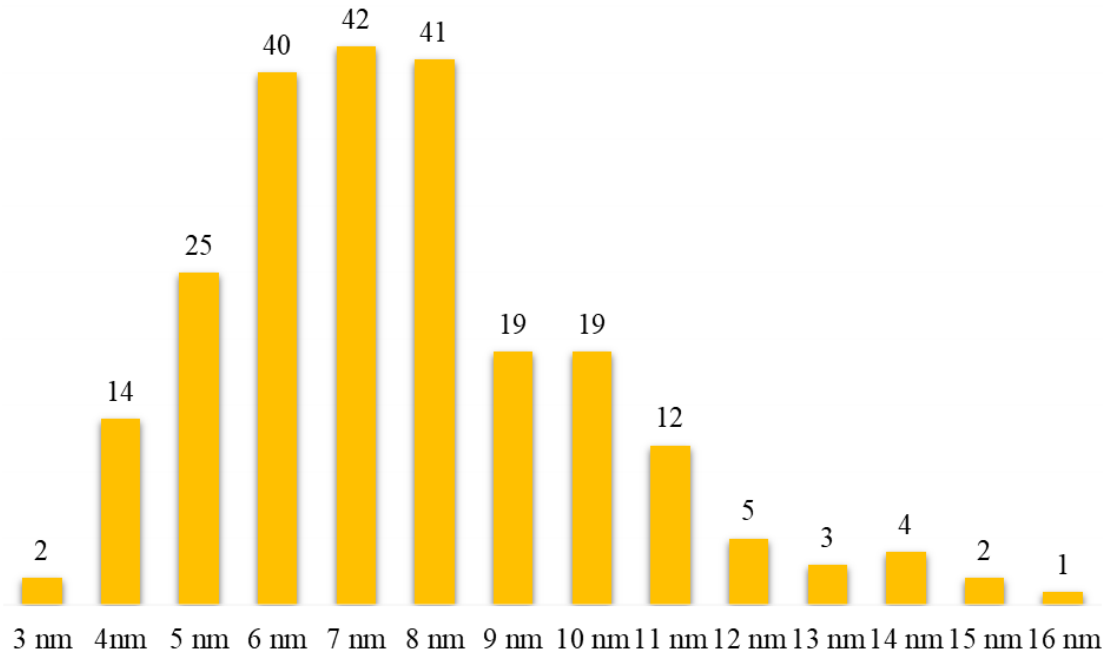


Figure 3.5. Size histogram of Sn-Fe bimetallic nanoparticles. Numbers over the bars indicate the number of NPs with the same size.

The average size of Sn-Co bimetallic nanoparticles is around 6.7 nm seen in TEM image and histogram displayed in Figure 3.6 and Figure 3.7. As in the case of Sn-Fe system, core-shell structures are visible and the similar reasonings listed there are also valid for this protocol.

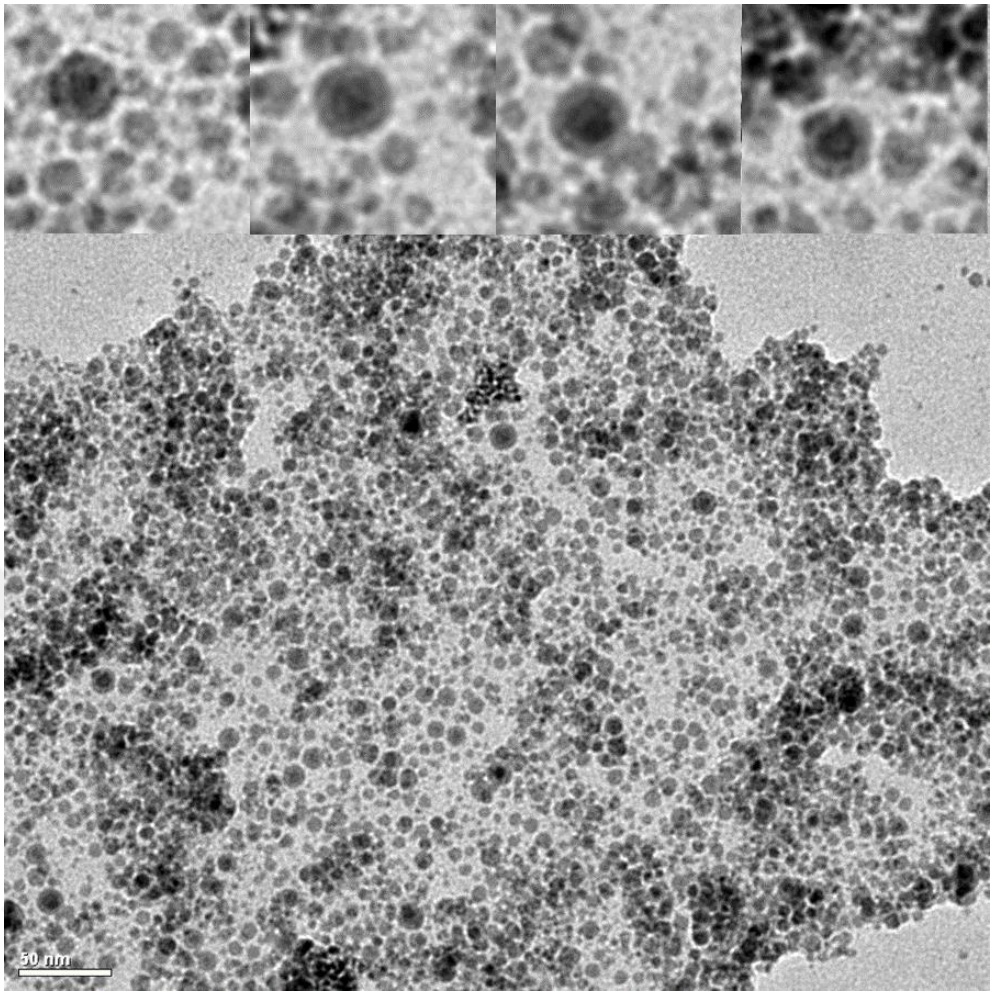


Figure 3.6. TEM image of Sn@Co core-shell nanoparticles.

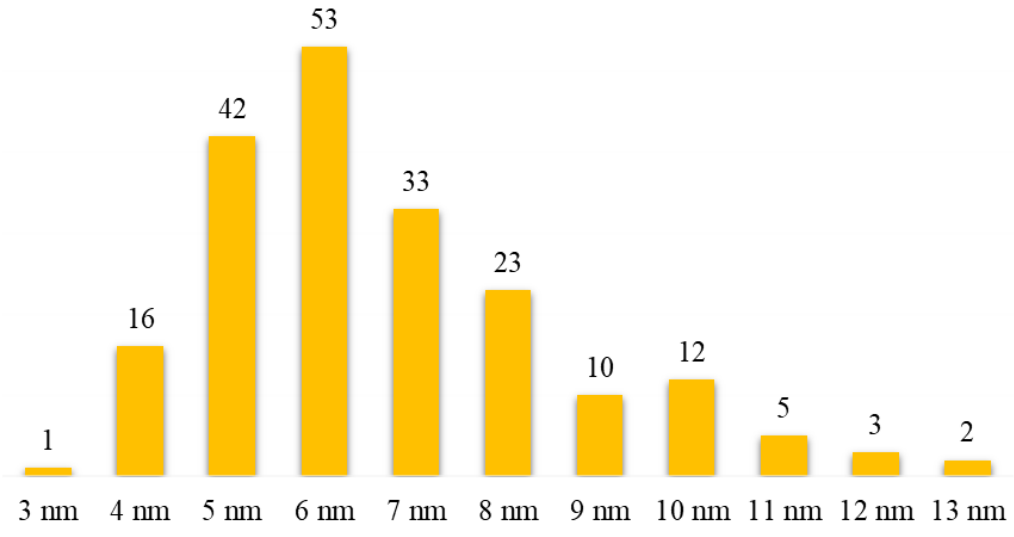


Figure 3.7. Size histogram of Sn-Co bimetallic nanoparticles. Numbers over the bars indicate the number of NPs with the same size.

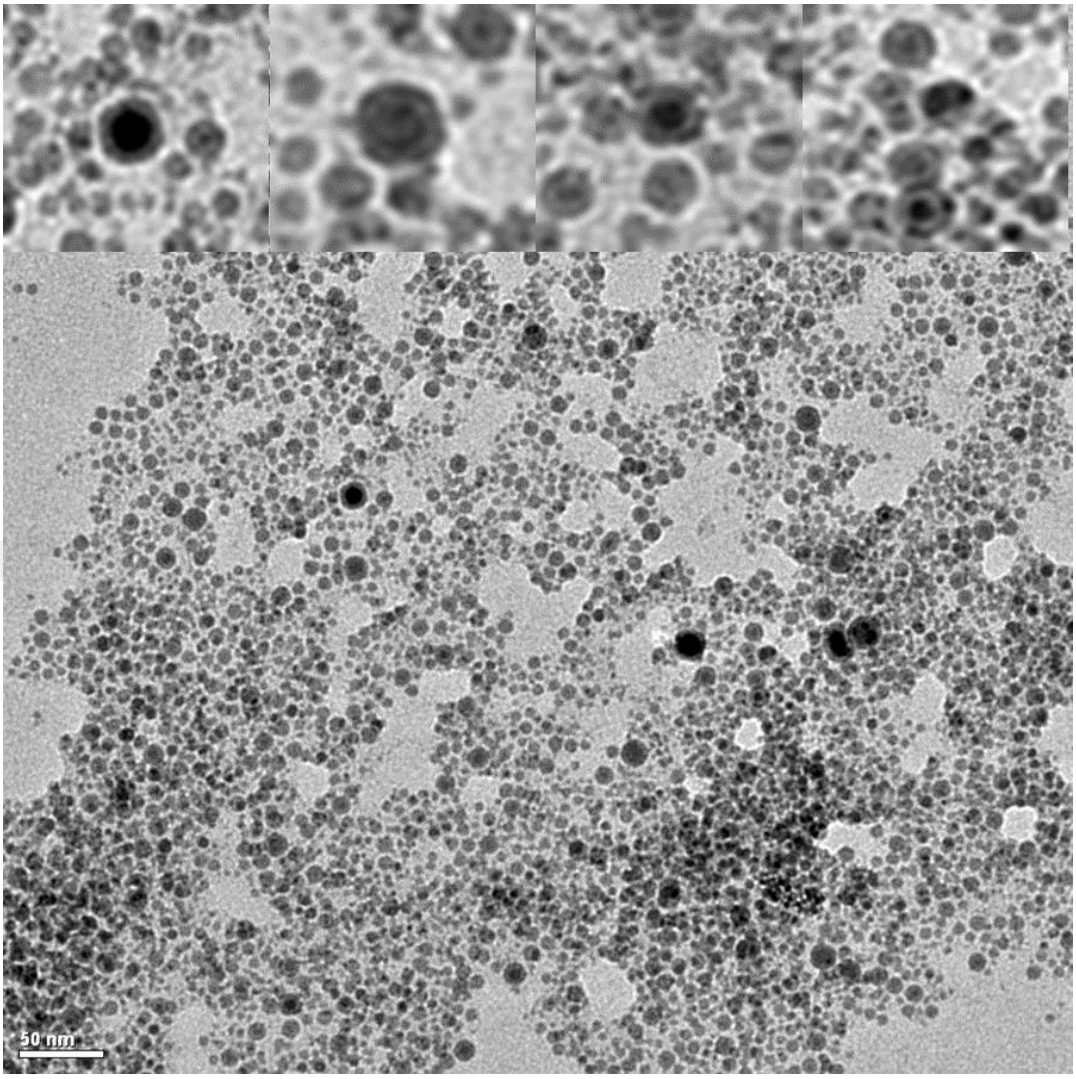


Figure 3.8. TEM image of Sn@CoFe core-shell nanoparticles.

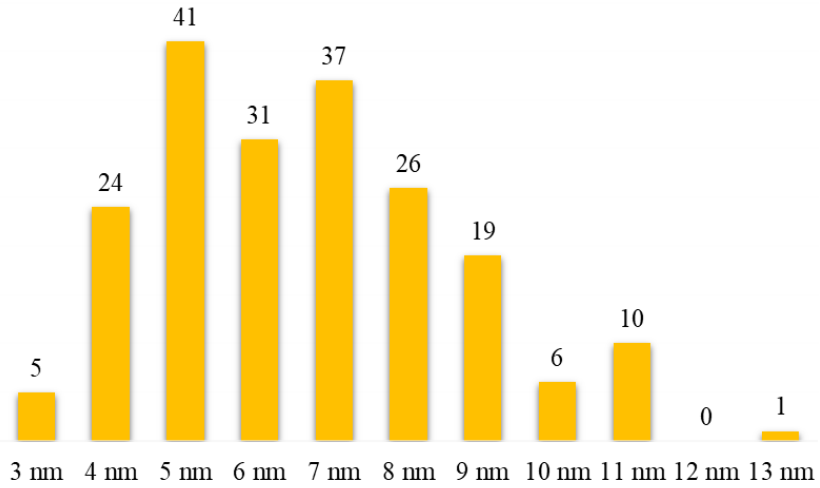


Figure 3.9. Size histogram of Sn-CoFe bimetallic nanoparticles. Numbers over the bars indicate the number of NPs with the same size.

The average size of nanoparticles that are resulted from the synthesis of Sn@CoFe core-shell nanoparticles, is around 6.6 nm seen in TEM image and histogram displayed in Figure 3.8 and Figure 3.9.

3.2. X-Ray Photoelectron Spectroscopy (XPS) and X-Ray Diffraction (XRD) Results

XPS technique together with XRD is a strong tool to analyze the structure and elemental composition of nanoparticles. XPS provides information about the empirical formulas, elemental compositions, electronic and chemical states of surface atoms. The crystal structure of the species is identified from the XRD data.

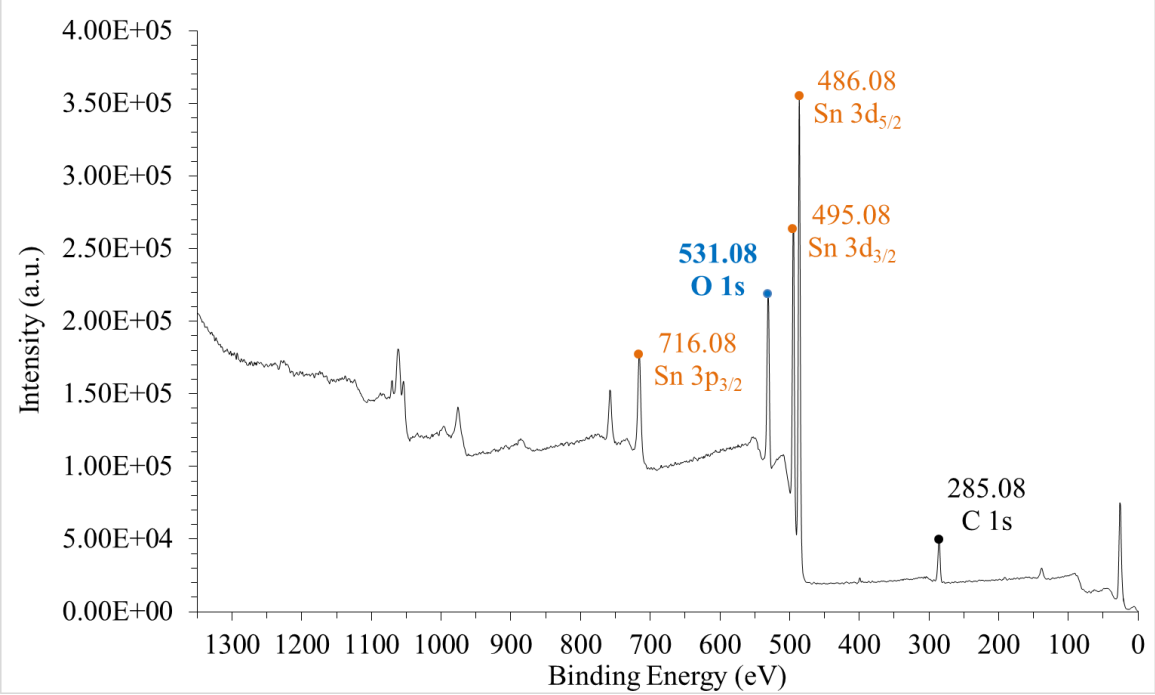


Figure 3.10. XPS survey analysis of as-prepared Sn nanoparticles.

The XPS survey analysis of as-prepared Sn nanoparticles (Figure 3.10) show that Sn, O, and C atoms present on the surface. Carbon atoms and some of the oxygen belong to surfactant PVP. Figure 3.11 shows that the tin species on the surface of the nanoparticles present mostly as oxides. The relative ratio of SnO to SnO_2 is higher due to its stability. Also, XRD results of Sn nanoparticles in Figure 3.12 confirm the presence of tin oxides. The broad peak between the 2θ values between 20° and 40° consists of the interference of mainly SnO_2 (26.9° and 29.6°), SnO (30.0°) and metallic tin (30.6° and 32.0°). There is a

small metallic peak around the 2θ value of 45.0°. The second broad peak between 47° and 65° consists of different phases of SnO_2, the dominant one is (211) phase of it, which has a signal at 57.5°.

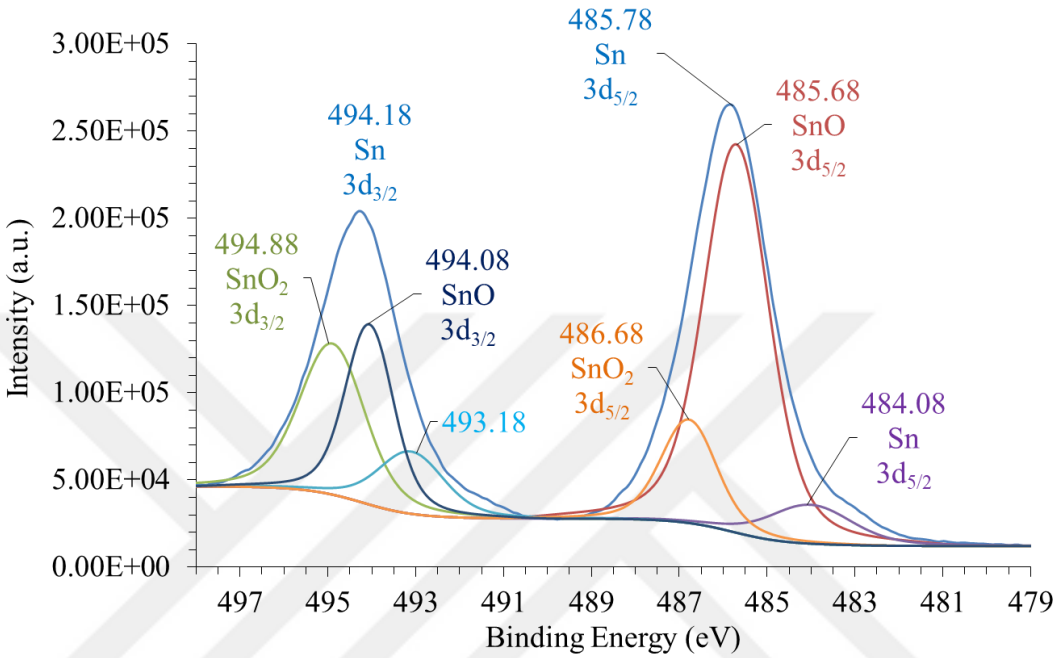


Figure 3.11. The Sn3d core level XPS spectra of as-prepared Sn nanoparticles.

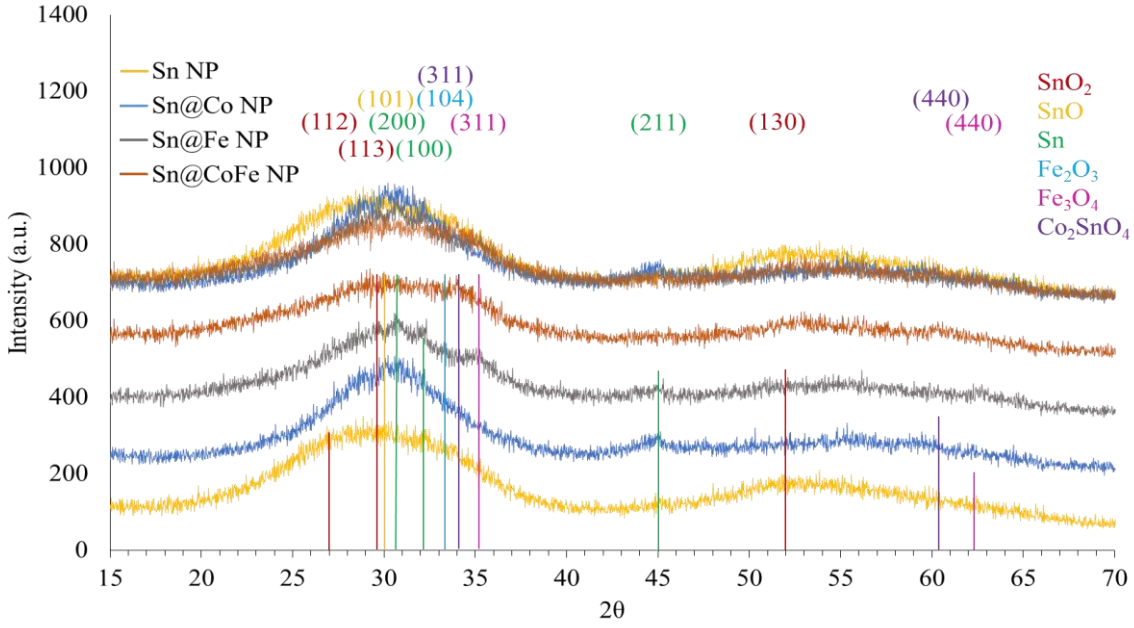


Figure 3.12. XRD results of all nanoparticles.

As in the case of all synthesis of core-shell nanoparticles, regardless of the metal on the shell, the atomic ratio of atoms present on the surface is higher than the ratio of moles

of metal precursors. For the case of Sn@Co NPs the precursor ratio of Co:Sn is 1:2, but XPS analysis show that Co:Sn ratio on the surface is 44:56. This indicates that cobalt atoms adsorbs to the surface of tin seeds, rather than self-nucleate. However, the signal of tin shows that it is also present on the surface. This can be interpreted in three ways:

(i) The amount of the cobalt precursor is not sufficient to cover all of the seed particles, which might lead to partial coverage of seeds or some seeds form core-shell structures while others remain naked or both.

(ii) Tin and cobalt might form alloys on the surface.

(iii) Cobalt atoms might self-nucleate to form separate nanoparticles.

Since we do not see any cobalt or any kind of cobalt oxide peak in the XRD spectrum of Sn@Co NPs, the third option seems to be a weak possibility. The second case is only visible in the XRD of Sn@CoFe nanoparticles. The shoulder peaks around 34.3° and 51.7° belongs to Co_2SnO_4 phase which does not exist in the Sn@Co NP case. This indicates that iron has a role in the formation of that alloy phase.

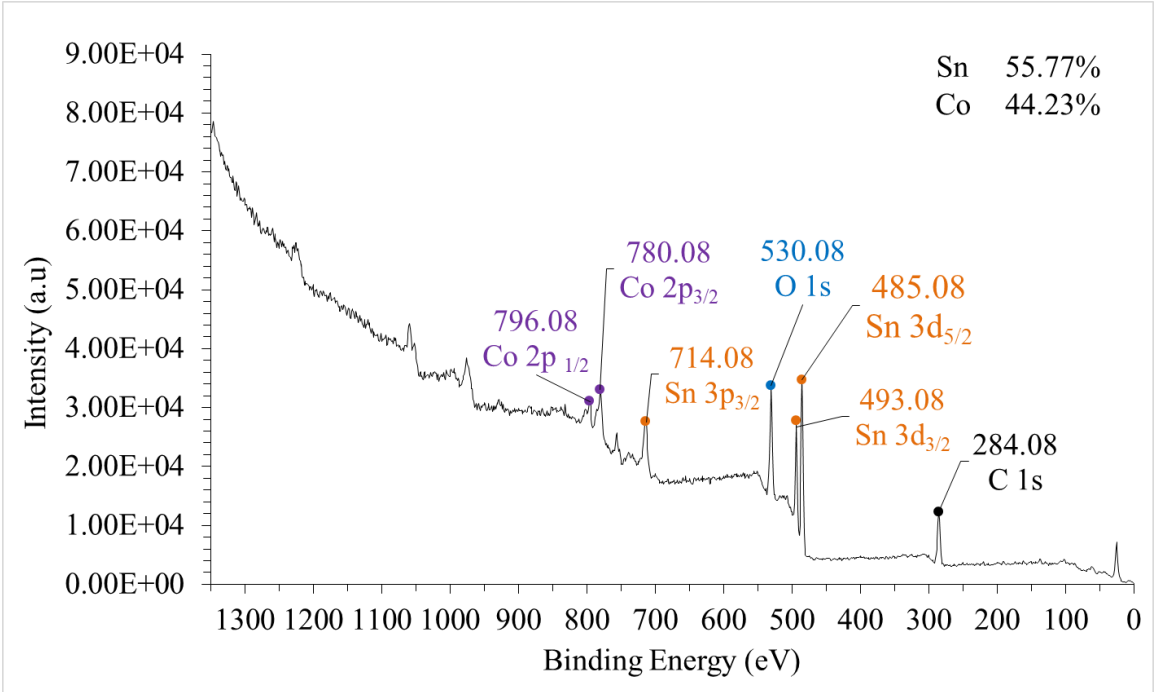


Figure 3.13. XPS survey analysis of Sn-Co nanoparticles.

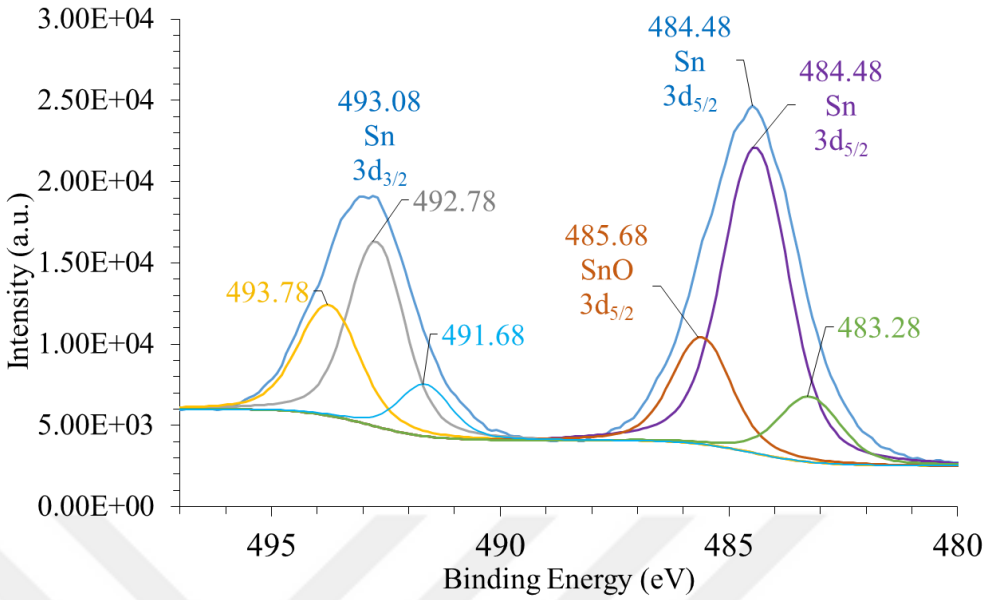


Figure 3.14. The Sn3d core level XPS spectra of Sn-Co nanoparticles.

Figure 3.12 shows that the tin oxide phases disappear and the amount of the metallic tin phase increases with the addition of second metal. The narrowing of first broad signal from left side that has SnO_2 signal at 26.9°, confirms that behavior. Same is observed for the XRD signal at 51.8°. In addition, the peaks of metallic tin at 30.7°, 32.0° and 44.9 becomes visible. This is expected since the reduction potential of tin is higher than cobalt or iron. Another reason for this occurrence might be the addition of reducing agent at the second phase of the synthesis, where shell is formed. The signals in the Figure 3.12 that does not have any corresponding data in the literature might belong to different phases of tin with cobalt.

Based on the XPS survey analysis of Sn-Fe NPs in Figure 3.15, the atomic ratio of atoms Sn:Fe is around 47:53 while the mole ratio used for synthesis is around 2:1. Hence, the same reason for possible situations in the Sn-Co case is valid for Sn-Fe system. One main difference is the greater atomic ratio over cobalt's even though the precursor amount is the same for both. This can be attributed to the formation of alloys between tin and cobalt on the surface, which automatically increases the relative ratio of tin on the surface or the concurrence of Sn2p peak with Fe2p peak.

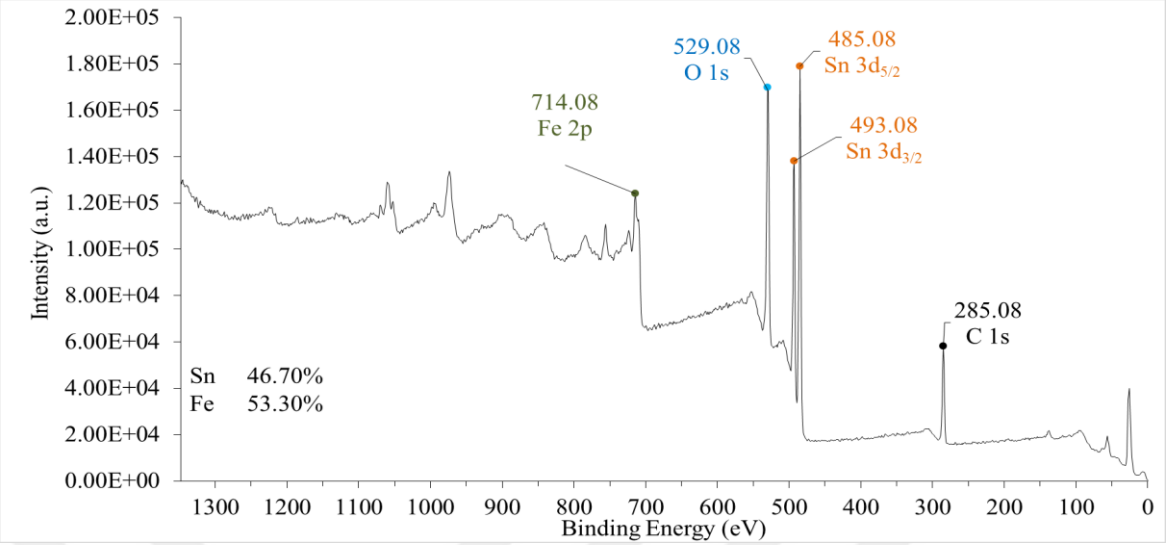


Figure 3.15. XPS survey analysis of Sn-Fe nanoparticles.

The disappearance of tin oxides is observed from both XPS (Figure 3.14) and XRD (Figure 3.12). XPS data in Figure 3.15 shows that the main composition of iron consists of its oxides and the lack of metallic iron peaks in the XRD is in the same line with this result. In addition, the magnetite shoulders exist in the Figure3.12 at 35.4° and 62.5° at Sn-Fe NPs. These Fe_3O_4 peaks also show that iron oxide exists as a shell layer on the tin core because the surface coverage is higher than cobalt one and there is no self-nucleation in cobalt.

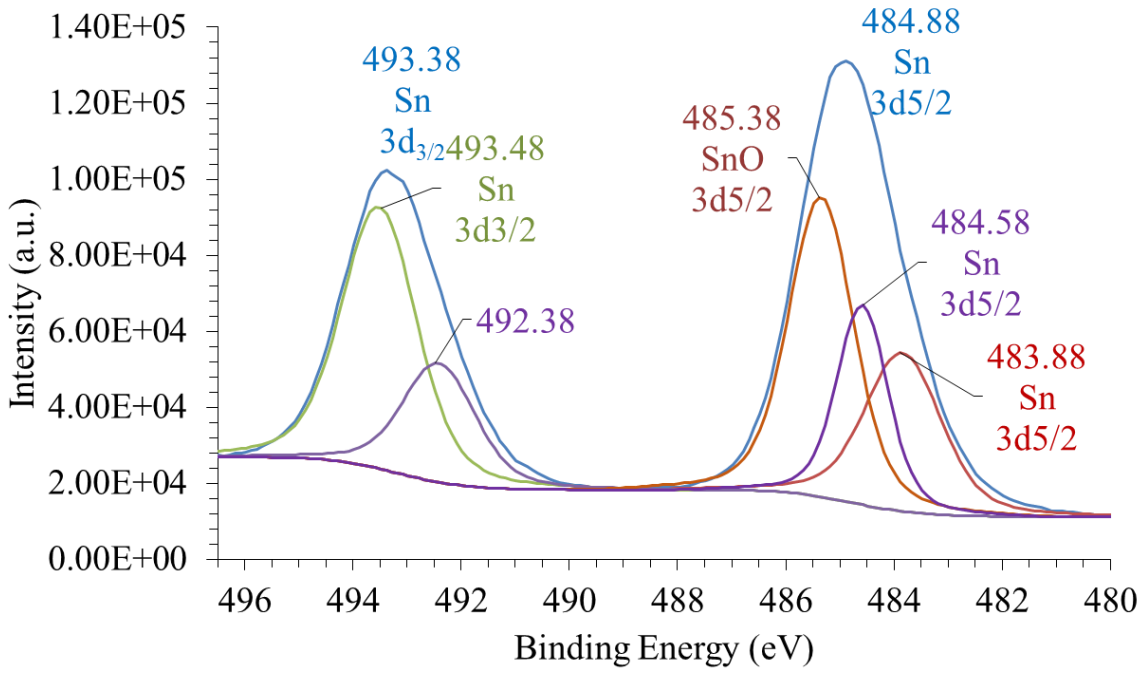


Figure 3.16 The Sn3d core level XPS spectra of Sn-Fe nanoparticles.

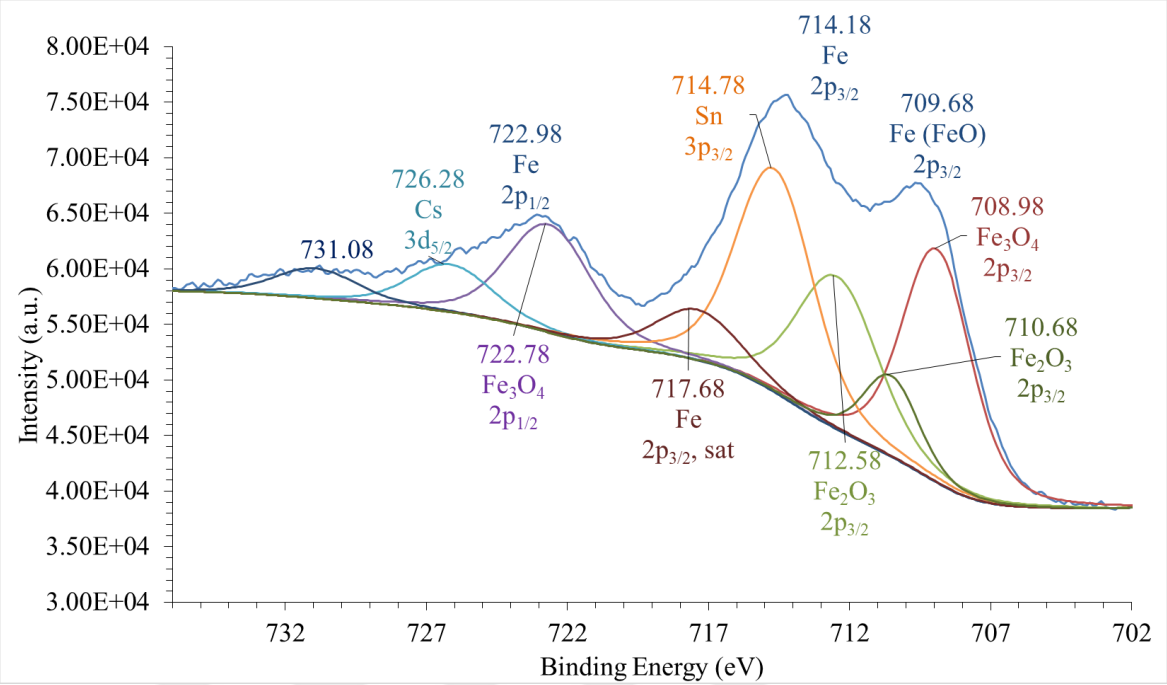


Figure 3.17. The Fe2p core level XPS spectra of Sn-Fe nanoparticles.

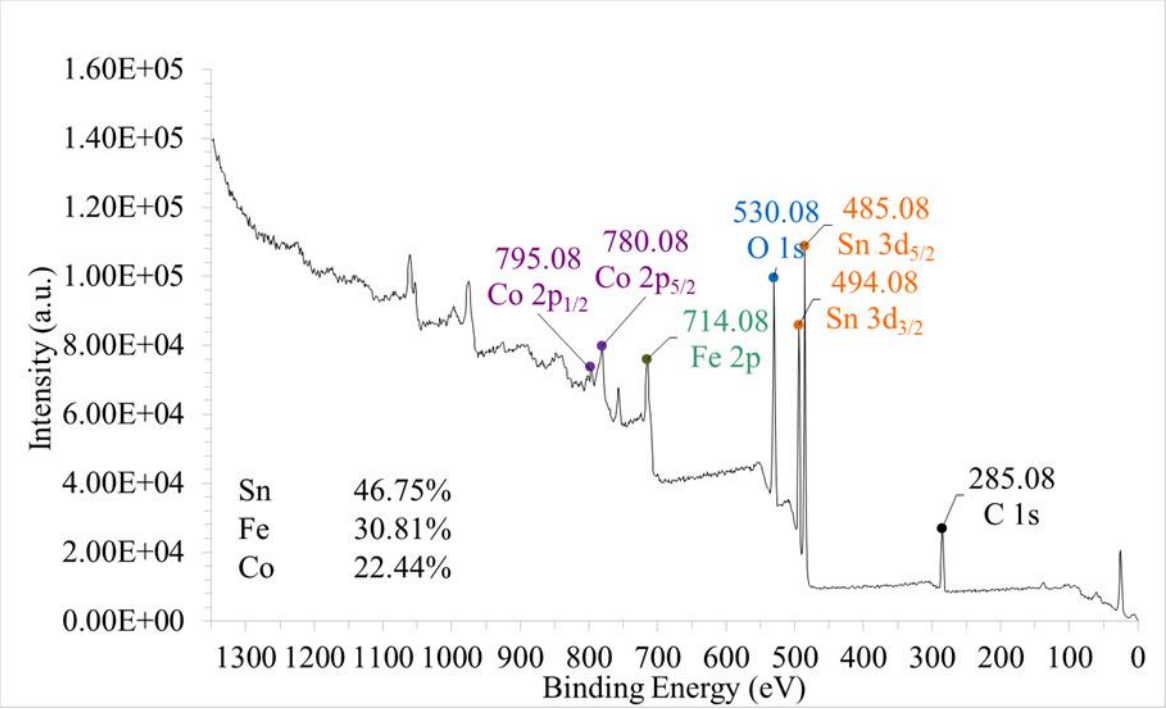


Figure 3.18. XPS survey analysis of Sn-CoFe nanoparticles.

The XPS survey analysis of Sn-CoFe NPs in Figure 3.18 demonstrates that the atomic ratio of Sn:Co:Fe on the surface is 47:22:31 while the precursor ratio was 4:1:1. Reduction of tin oxides is still the case as in other bimetallic systems shown with XRD and XPS data.

According to XPS in Figure 3.19, Figure 3.20 and Figure 3.21, and XRD data in Figure 3.12, there is no metallic cobalt in nanoparticles and this minimizes the possibility of self-nucleation. Since there is no crystalline phase of cobalt that consists of cobalt or its oxide, the possibility of the existence of a cobalt shell is low. If there is a cobalt shell, then it must be amorphous or alloy form with tin. The XRD peaks for these NPs at 34.3° and 60.4° in Figure 3.12 are characteristic to Co_2SnO_4. Other binary or ternary alloys involving Sn, Co, Fe have signals around these points but their other characteristic signals do not exist in our spectrum. The metallic tin peak at 32.9° and 44.9° that exist in Sn-Co and Sn-Fe NPs disappear in the XRD spectrum of Sn-CoFe NPs. This can be related to that Co_2SnO_4 formation and clearly iron has a key role in this occurrence since it does not happen in Sn-Co NPs. The difference between the Fe2p core level XPS spectra of Sn-Fe and Sn-CoFe NPs Figure 3.21, where the relative ratio of Fe_3O_4 phase decreases, supports this claim.

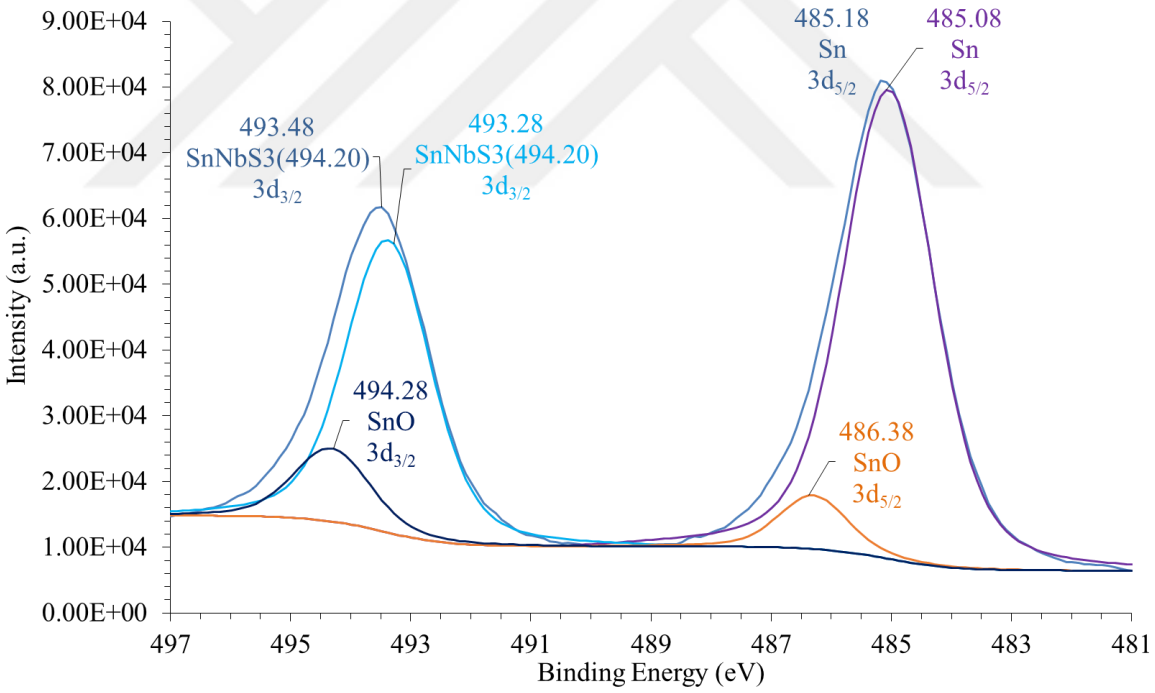


Figure 3.19. The Sn3d core level XPS spectra of Sn-CoFe nanoparticles.

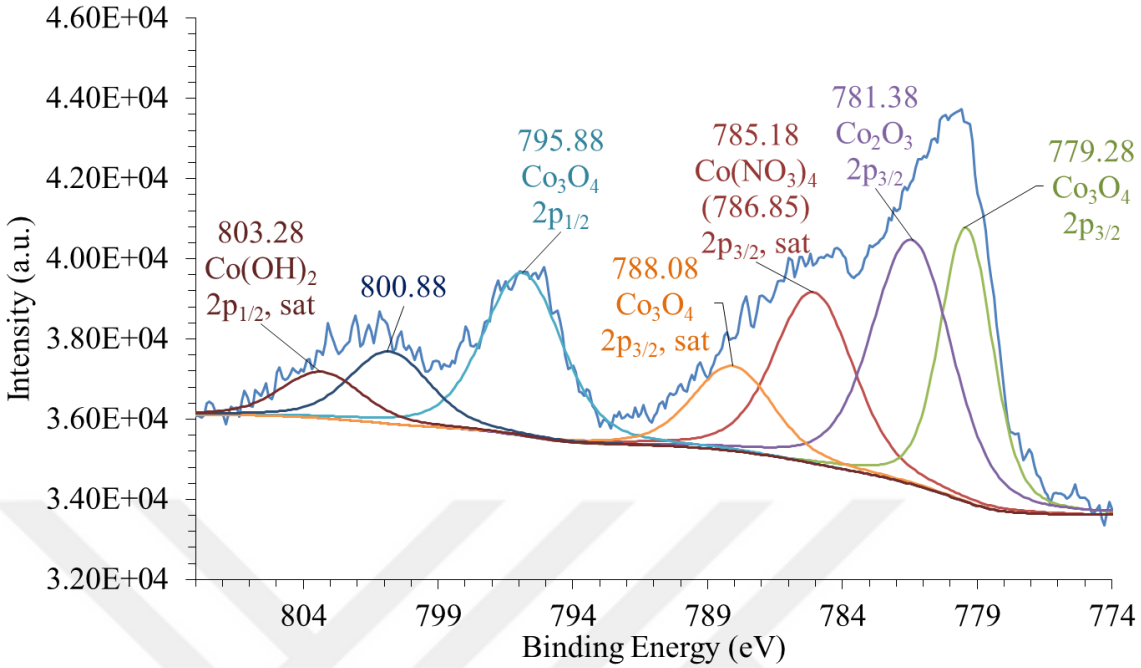


Figure 3.20. The Co2p core level XPS spectra of Sn-CoFe nanoparticles.

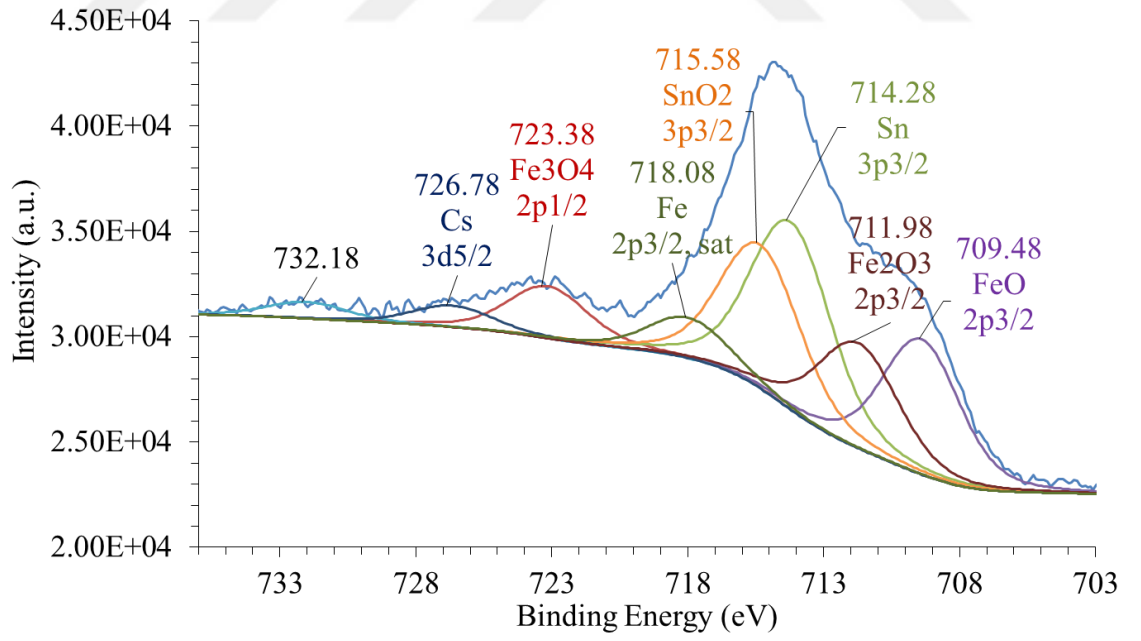


Figure 3.21. The Fe2p core level XPS spectra of Sn-CoFe nanoparticles.

4. CONCLUSIONS

Firstly, tin nanoparticles with an average size of 6.3 nm is synthesized as seeds for core-shell structures by a polyol process. XRD and XPS results show that it has metallic and oxide phases and oxides mainly sits on the surface. Lattice fringes measured as 0.301 nm corresponds to (200) plane of metallic tin.

All bimetallic systems lead to reduction of tin nanoparticles to an extent which is most probably due to relatively high reduction potential of tin. This itself, shows that these atoms of different metals reside on the same particle. The higher abundance of secondary metal atoms on surface relative to used amount of precursor indicates the adsorption of these metals (Co and Fe) to surface rather than self-nucleation.

In the case of Sn@Co NPs there is no peak of metallic cobalt or its oxide in the XRD spectrum, which is another proof against the self-nucleation of cobalt. However, it also shows that either cobalt or its oxides on the surface are amorphous or in an alloy state.

On the other hand, Sn@Fe NPs show same or greater iron atom coverage with magnetite peaks in XRD. Similar surface coverage with cobalt indicates that the occurrence of self-nucleation is low, if any. Along this, the magnetite peaks in the XRD proves the existence of a metal-oxide shell or islands. But the amount of iron precursor, also cobalt, should be increased for total coverage, if it is possible.

Sn@CoFe NPs mostly show similar trends with Sn@Co and Sn@Fe NPs. One peculiar result is that, while SnO_2 XRD peaks disappear but no metallic tin peak appears as it was the case for other bimetallic nanoparticles. Instead a new Co_2SnO_4 peak appeared, which was not the case in Sn@Co NPs. Apparently, iron or its oxides play a key role in this formation.

This attempt of synthesis of bimetallic core-shell nanoparticles with aforementioned elements with this polyol method is new to literature. The results are promising and has the potential of showing the direction of future work in the synthesis of such structures.

5. FUTURE WORK

The first thing to do is to implement these nanoparticles for performance tests for FTS. In that work, the activity (TOF) towards FTS and its reaction steps (CO hydrogenation, C-O bond scission etc.), selectivity and stability of nanoparticles under reaction conditions should be investigated. Since reaction conditions play a crucial role, their optimization for a single nanoparticle type as a catalyst would be an important study in itself.

Secondly, the synthesis protocol is open to any optimization from changing precursors, surfactants, their concentrations to manipulating reaction conditions. The most urgent one among them is increasing the precursor amount of the secondary metal and to check whether full coverage of tin seed without obtaining too thick shell or self-nucleation is possible with this setup.

The role of size, composition and shell thickness over the performance of these catalysts, is another option to study. The change of shell material would diverse the application fields of these core-shell structures. Namely, Sn@Pt nanoparticles would be a great candidate for fuel cell applications.

REFERENCES

1. U. Hanefeld and L. Lefferts, *Catalysis: An Integrated Textbook for Students*, John Wiley and Sons, 2018.

2. A. Groß, *Theoretical Surface Science A Microscopic Perspective*, 2nd ed. Springer Berlin, 2014.

3. B. I. Lundqvist, O. Gunnarsson, H. Hjelmberg, and J. K. Nørskov, "Theoretical description of molecule-metal interaction and surface reactions", *Surf. Sci.*, Vol. 89, 1–3, pp. 196–225, 1979.

4. M. G. Evans and M. Polanyi, "Inertia and driving force of chemical reactions", *Trans. Faraday Soc.*, Vol. 34, 0, pp. 11–24, 1938.

5. R. A. van (Rutger A. . Santen and M. Neurock, *Molecular heterogeneous catalysis: a conceptual and computational approach*, Wiley-VCH, 2006.

6. M. Che and C. O. Bennett, "The Influence of Particle Size on the Catalytic Properties of Supported Metals", *Adv. Catal.*, Vol. 36, C, pp. 55–172, 1989.

7. A. Hervier, J. R. Renzas, J. Y. Park, and G. A. Somorjai, "Hydrogen Oxidation-Driven Hot Electron Flow Detected by Catalytic Nanodiodes", *Nano Lett.*, Vol. 9, 11, pp. 3930–3933, 2009.

8. S. J. Tauster, "Strong metal-support interactions", *Acc. Chem. Res.*, Vol. 20, 11, pp. 389–394, 1987.

9. D. Uzio and G. Berhault, "Factors governing the catalytic reactivity of metallic nanoparticles", *Catal. Rev. - Sci. Eng.*, Vol. 52, 1, pp. 106–131, 2010.

10. F. Fischer and H. Tropsch, "Process for the production of paraffin-hydrocarbons with more than one carbon atom", US1746464A, 1926.

11. H. H. Storch, N. Golumbic, and R. B. Anderson, *Fischer-Tropsch and Related Syntheses*. John Wiley and Sons, 1961.

12. M. E. Dry, "The Fischer–Tropsch process: 1950–2000", *Catal. Today*, Vol. 71, 3–4, pp. 227–241, 2002.

13. S. T. Sie, "Process development and scale up: IV. Case history of the development of a fischer-tropsch synthesis process", *Rev. Chem. Eng.*, Vol. 14, 2, pp. 109–157, 1998.

14. R. Oukaci, A. H. Singleton, and J. G. Goodwin, "Comparison of patented Co F-T catalysts using fixed-bed and slurry bubble column reactors", *Appl. Catal. A Gen.*, Vol. 186, 1–2, pp. 129–144, 1999.

15. J. Van de Loosdrecht *et al.*, *Fischer-Tropsch Synthesis: Catalysts and Chemistry*, Vol. 7, August. Elsevier Ltd., 2013.

16. J. R. Rostrup-Nielsen, J. Sehested, and J. K. Nørskov, "Hydrogen and Synthesis Gas by Steam- and CO2 Reforming", in *Advances in Catalysis*, Vol. 47, pp. 65–139, 2002.

17. H. Schulz, E. vein Steen, and M. Claeys, "Selectivity and mechanism of Fischer-Tropsch synthesis with iron and cobalt catalysts", *Stud. Surf. Sci. Catal.*, Vol. 81, pp. 455–460, 1994.

18. G. P. Van der Laan and A. A. C. M. Beenackers, "Kinetics and Selectivity of the Fischer–Tropsch Synthesis: A Literature Review", *Catal. Rev.*, Vol. 41, 3–4, pp. 255–318, 1999.

19. F. G. Botes and N. S. Govender, "Secondary Reactions of Ethylene As Studied in a Laboratory-Scale Recycle Slurry Reactor", *Energy & Fuels*, Vol. 21, 6, pp. 3095–3101, 2007.

20. F. G. Botes, "Proposal of a new product characterization model for the iron-based low-temperature Fischer-Tropsch synthesis", *Energy and Fuels*, Vol. 21, 3, pp. 1379–1389, 2007.

21. A. Y. Khodakov, W. Chu, and P. Fongarland, "Advances in the development of novel cobalt Fischer-Tropsch catalysts for synthesis of long-chain hydrocarbons and clean fuels", *Chemical Reviews*, Vol. 107, 5. American Chemical Society, pp. 1692–1744, 2007.

22. M. E. Dry, "Fischer-Tropsch synthesis over iron catalysts", *Catal. Letters*, Vol. 7, 1–4, pp. 241–251, 1990.

23. B. H. Davis, "Fischer-Tropsch synthesis: Comparison of performances of iron and cobalt catalysts", in *Industrial and Engineering Chemistry Research*, Vol. 46, 26, pp. 8938–8945, 2007.

24. E. de Smit and B. M. Weckhuysen, "The renaissance of iron-based Fischer–Tropsch synthesis: on the multifaceted catalyst deactivation behaviour", *Chem. Soc. Rev.*, Vol. 37, 12, p. 2758, 2008.

25. A. P. Steynberg, R. L. Espinoza, B. Jager, and A. C. Vosloo, "High temperature Fischer–Tropsch synthesis in commercial practice", *Appl. Catal. A Gen.*, Vol. 186, 1–2, pp. 41–54, 1999.

26. R. L. Espinoza, A. P. Steynberg, B. Jager, and A. C. Vosloo, "Low temperature Fischer–Tropsch synthesis from a Sasol perspective", *Appl. Catal. A Gen.*, Vol. 186, 1–2, pp. 13–26, 1999.

27. J. J. C. Geerlings, J. H. Wilson, G. J. Kramer, H. P. C. E. Kuipers, A. Hoek, and H. M. Huisman, "Fischer–Tropsch technology — from active site to commercial process", *Appl. Catal. A Gen.*, Vol. 186, 1–2, pp. 27–40, 1999.

28. S. R. Deshmukh *et al.*, "Enabling cellulosic diesel with microchannel technology", *Biofuels*, Vol. 2, 3. Future Science LtdLondon, UK, pp. 315–324, 2011.

29. C. G. Visconti *et al.*, "An experimental investigation of Fischer-Tropsch synthesis over washcoated metallic structured supports", *Appl. Catal. A Gen.*, Vol. 370, 1–2, pp. 93–101, 2009.

30. B. H. Davis, "Fischer-Tropsch synthesis: Relationship between iron catalyst composition and process variables", in *Catalysis Today*, Vol. 84, 1–2, pp. 83–98, 2003.

31. B. H. Davis, "Fischer-Tropsch synthesis: relationship between iron catalyst composition and process variables", *Catal. Today*, Vol. 84, 1–2, pp. 83–98, 2003.

32. D. F. Smith, C. O. Hawk, and P. L. Golden, "The mechanism of the formation of higher hydrocarbons from water gas", *J. Am. Chem. Soc.*, Vol. 52, 8, pp. 3221–3232, 1930.

33. H. Hayakawa, H. Tanaka, and K. Fujimoto, "Studies on precipitated iron catalysts for Fischer–Tropsch synthesis", *Appl. Catal. A Gen.*, Vol. 310, pp. 24–30, 2006.

34. R. J. O'Brien, L. Xu, R. L. Spicer, S. Bao, D. R. Milburn, and B. H. Davis, "Activity and selectivity of precipitated iron Fischer-Tropsch catalysts", *Catal. Today*, Vol. 36, 3, pp. 325–334, 1997.

35. M. Luo, R. J. O'Brien, S. Bao, and B. H. Davis, "Fischer–Tropsch synthesis: induction and steady-state activity of high-alpha potassium promoted iron catalysts", *Appl. Catal. A Gen.*, Vol. 239, 1–2, pp. 111–120, 2003.

36. R. J. O'Brien, L. Xu, R. L. Spicer, and B. H. Davis, "Activation Study of Precipitated Iron Fischer−Tropsch Catalysts", *Energy & Fuels*, Vol. 10, 4, pp. 921–926, 1996.

37. A. J. H. M. Kock and J. W. Geus, "The characterization of iron surfaces", *Prog. Surf. Sci.*, Vol. 20, 3, pp. 165–272, 1985.

38. J. W. Niemantsverdriet, *Spectroscopy in Catalysis: An Introduction*, 3rd ed., Vol. 68. Weinheim, Germany, 2007.

39. J. W. Niemantsverdriet, A. M. Van der Kraan, W. L. Van Dijk, and H. S. Van der Baan, "Behavior of metallic iron catalysts during Fischer-Tropsch synthesis studied with Moessbauer spectroscopy, x-ray diffraction, carbon content determination, and reaction kinetic measurements", *J. Phys. Chem.*, Vol. 84, 25, pp. 3363–3370, 1980.

40. G. B. Raupp and W. N. Delgass, "Mössbauer investigation of supported Fe and FeNi catalysts: II. Carbides formed Fischer-Tropsch synthesis", *J. Catal.*, Vol. 58, 3, pp. 348–360, 1979.

41. E. De Smit *et al.*, "Stability and reactivity of ε-X-θ iron carbide catalyst phases in fischer-tropsch synthesis: Controlling μc", *J. Am. Chem. Soc.*, Vol. 132, 42, pp. 14928–14941, 2010.

42. M. E. Dry, "FT catalysts", in *Studies in Surface Science and Catalysis*, Vol. 152, Elsevier, pp. 533–600, 2004.

43. M. Luo, H. Hamdeh, and B. H. Davis, "Fischer-Tropsch Synthesis: Catalyst activation of low alpha iron catalyst", *Catal. Today*, Vol. 140, 3–4, pp. 127–134, 2009.

44. T. Herranz, S. Rojas, F. J. Pérez-Alonso, M. Ojeda, P. Terreros, and J. L. G. Fierro, "Genesis of iron carbides and their role in the synthesis of hydrocarbons from synthesis gas", *J. Catal.*, Vol. 243, 1, pp. 199–211, 2006.

45. J. R. Anderson and M. Boudart, *Catalysis : Science and Technology*, Vol. 1. Springer-Verlag: New York, 1981.

46. M. Luo and B. H. Davis, "Fischer–Tropsch synthesis: activation of low-alpha potassium promoted iron catalysts", *Fuel Process. Technol.*, Vol. 83, 1–3, pp. 49–65, 2003.

47. R. A. Fiato and S. L. Soled, "Fischer-Tropsch hydrocarbon synthesis with high surface area Cu and K promoted reduced-carbided iron/manganese spinels", US4621102, 1986.

48. J. W. Niemantsverdriet and A. M. van der Kraan, "On the time-dependent behavior of iron catalysts in Fischer-Tropsch synthesis", *J. Catal.*, Vol. 72, 2, pp. 385–388, 1981.

49. T. C. Bromfield and R. Visagie, "The use of a source of chromium with a precipitated catalyst in a fischer-tropsch reaction", WO2005049765A1, 2005.

50. E. Iglesia, S. C. Reyes, R. J. Madon, and S. L. Soled, "Selectivity Control and Catalyst Design in the Fischer-Tropsch Synthesis: Sites, Pellets, and Reactors", *Adv. Catal.*, Vol. 39, pp. 221–302, 1993.

51. N. E. Tsakoumis, M. Rønning, Ø. Borg, E. Rytter, and A. Holmen, "Deactivation of cobalt based Fischer–Tropsch catalysts: A review", *Catal. Today*, Vol. 154, 3–4, pp. 162–182, 2010.

52. J. van de Loosdrecht *et al.*, "Cobalt Fischer-Tropsch synthesis: Deactivation by oxidation?", *Catal. Today*, Vol. 123, 1–4, pp. 293–302, 2007.

53. A. M. Saib *et al.*, "Fundamental understanding of deactivation and regeneration of cobalt Fischer-Tropsch synthesis catalysts", *Catal. Today*, Vol. 154, 3–4, pp. 271–282, 2010.

54. M. Claeys and E. van Steen, "Basic studies", in *Studies in Surface Science and Catalysis*, Vol. 152, Elsevier, 2004, pp. 601–680.

55. F. Morales and B. M. Weckhuysen, "Promotion Effects in Co-based Fischer–Tropsch Catalysis", *Catalysis*, Vol. 19, pp. 1–40, 2006.

56. B. H. Davis, "Fischer-Tropsch synthesis: Comparison of performances of iron and cobalt catalysts", in *Industrial and Engineering Chemistry Research*, Vol. 46, 26, pp. 8938–8945, 2007.

57. F. Diehl and A. Y. Khodakov, "Promotion of Cobalt Fischer-Tropsch Catalysts with Noble Metals: a Review", *Oil Gas Sci. Technol. - Rev. l'IFP*, Vol. 64, 1, pp. 11–24, 2009.

58. G. L. Bezemer *et al.*, "Cobalt particle size effects in the Fischer-Tropsch reaction studied with carbon nanofiber supported catalysts", *J. Am. Chem. Soc.*, Vol. 128, 12, pp. 3956–3964, 2006.

59. H. Karaca *et al.*, "In situXRD investigation of the evolution of alumina-supported cobaltcatalysts under realistic conditions of Fischer-Tropsch synthesis", *Chem. Commun.*, Vol. 46, 5, pp. 788–790, 2010.

60. O. Kitakami, H. Sato, Y. Shimada, F. Sato, and M. Tanaka, "Size effect on the crystal phase of cobalt fine particles", *Phys. Rev. B*, Vol. 56, 21, pp. 13849–13854, 1997.

61. D. I. Enache, B. Rebours, M. Roy-Auberger, and R. Revel, "In Situ XRD Study of the Influence of Thermal Treatment on the Characteristics and the Catalytic Properties of Cobalt-Based Fischer–Tropsch Catalysts", *J. Catal.*, Vol. 205, 2, pp. 346–353, 2002.

62. E. Iglesia, S. L. Soled, R. A. Fiato, and G. H. Via, "Bimetallic Synergy in Cobalt Ruthenium Fischer-Tropsch Synthesis Catalysts", *J. Catal.*, Vol. 143, 2, pp. 345–368, 1993.

63. A. Feller, M. Claeys, and E. van Steen, "Cobalt Cluster Effects in Zirconium Promoted Co/SiO2 Fischer–Tropsch Catalysts", *J. Catal.*, Vol. 185, 1, pp. 120–130, 1999.

64. G. . Moradi, M. . Basir, A. Taeb, and A. Kiennemann, "Promotion of Co/SiO2 Fischer–Tropsch catalysts with zirconium", *Catal. Commun.*, Vol. 4, 1, pp. 27–32, 2003.

65. K. F. Tan, J. Chang, A. Borgna, and M. Saeys, "Effect of boron promotion on the stability of cobalt Fischer–Tropsch catalysts", *J. Catal.*, Vol. 280, 1, pp. 50–59, 2011.

66. E. Rytter, T. H. Skagseth, S. Eri, and A. O. Sjåstad, "Cobalt Fischer−Tropsch Catalysts Using Nickel Promoter as a Rhenium Substitute to Suppress Deactivation", *Ind. Eng. Chem. Res.*, Vol. 49, 9, pp. 4140–4148, 2010.

67. H. Beuther, C. L. Kibby, T. P. Kobylinski, and R. B. Pannell, "Conversion of synthesis gas to diesel fuel and catalyst therefor", US4605680A, 1986.

68. H. Beuther, C. L. Kibby, T. P. Kobylinski, and R. B. Pannell, "Fluid bed catalyst for synthesis gas conversion and utilization thereof for preparation of diesel fuel", US4413064A, 1983.

69. H. Beuther and C. Kibby, "Synthesis gas conversion using ruthenium-promoted cobalt catalyst", US4585798A, 1986.

70. S. Eri, K. J. Kinnari, D. Schanke, and A.-M. Hilmen, "Catalyseur fischer-tropsch dote d'alumine a faible aire specifique, preparation et utilisation associees", WO2002047816A1, 2002.

71. E. van Steen and M. Claeys, "Fischer-Tropsch Catalysts for the Biomass-to-Liquid (BTL)-Process", *Chem. Eng. Technol.*, Vol. 31, 5, pp. 655–666, 2008.

72. B. P. J. Van, D. L. J. Van, E. A. Caricato, and S. Barradas, "Process for producing hydrocarbons from a synthesis gas, and catalysts therefor", WO1999042214A1, 1999.

73. P. J. Van Berge, J. Van de Loosdrecht, and S. Barradas, "Production of fischer-tropsch synthesis produced wax", EP1432778B1, 2001.

74. P. J. Van Berge, J. Van de Loosdrecht, and S. Barradas, "Production of hydrocarbons from a synthesis gas", EP1303350B1, 2001.

75. H. Xiong, M. A. M. Motchelaho, M. Moyo, L. L. Jewell, and N. J. Coville, "Correlating the preparation and performance of cobalt catalysts supported on carbon nanotubes and carbon spheres in the Fischer–Tropsch synthesis", *J. Catal.*, Vol. 278, 1, pp. 26–40, 2011.

76. M. J. Keyser, R. C. Everson, and R. L. Espinoza, "Fischer–Tropsch studies with cobalt–manganese oxide catalysts: Synthesis performance in a fixed bed reactor", *Appl. Catal. A Gen.*, Vol. 171, 1, pp. 99–107, 1998.

77. BASF, "Co-Precipitated Cobalt–Zinc Catalysts for Fischer–Tropsch Reaction or Functional Group Hydrogenation", EP1358934A1, 2003.

78. A. H. Joustra and B. Scheffer, "Process for the preparation of alumina-based extrudates", EP0455307A1, 1991.

79. A. V. Neimark, L. I. Kheifets, and V. B. Fenelonov, "Theory of preparation of supported catalysts", *Ind. Eng. Chem. Prod. Res. Dev.*, Vol. 20, 3, pp. 439–450, 1981.

80. K. P. de Jong, "Deposition Precipitation Onto Pre-Shaped Carrier Bodies. Possibilities and Limitations", *Stud. Surf. Sci. Catal.*, Vol. 63, pp. 19–36, 1991.

81. S. Järas, S. Lögdberg, and M. Boutonnet, "Method for depositing metal particles on a support", EP1985361A1, 2008.

82. J. van de Loosdrecht *et al.*, "Calcination of Co-Based Fischer–Tropsch Synthesis Catalysts", *Top. Catal.*, Vol. 26, 1–4, pp. 121–127, 2003.

83. M. Wolters, P. Munnik, J. H. Bitter, P. E. de Jongh, and K. P. de Jong, "Method for producing a supported metal nitrate", WO2010109216A1, 2010.

84. S. L. Soled, J. E. Baumgartner, S. C. Reyes, and E. Iglesia, "Synthesis of eggshell cobalt catalysts by molten salt impregnation techniques", *Stud. Surf. Sci. Catal.*, Vol. 91, pp. 989–997, 1995.

85. W. C. Behrmann, S. M. Davis, and C. H. Mauldin, "Method for preparing cobalt-containing hydrocarbon synthesis catalyst", WO1992006784A1, 1991.

86. H. Oosterbeek, "Bridging the pressure and material gap in heterogeneous catalysis: cobalt Fischer–Tropsch catalysts from surface science to industrial application", *Phys. Chem. Chem. Phys.*, Vol. 9, 27, pp. 3570–3576, 2007.

87. E. Iglesia, "Design, synthesis, and use of cobalt-based Fischer-Tropsch synthesis catalysts", *Appl. Catal. A Gen.*, Vol. 161, 1–2, pp. 59–78, 1997.

88. Ø. Borg *et al.*, "Fischer–Tropsch synthesis: Cobalt particle size and support effects on intrinsic activity and product distribution", *J. Catal.*, Vol. 259, 2, pp. 161–164, 2008.

89. G. Prieto, A. Martínez, P. Concepción, and R. Moreno-Tost, "Cobalt particle size effects in Fischer–Tropsch synthesis: structural and in situ spectroscopic characterisation on reverse micelle-synthesised Co/ITQ-2 model catalysts", *J. Catal.*, Vol. 266, 1, pp. 129–144, 2009.

90. A. Martínez and G. Prieto, "Breaking the dispersion-reducibility dependence in oxide-supported cobalt nanoparticles", *J. Catal.*, Vol. 245, 2, pp. 470–476, 2007.

91. G.-Z. Bian, N. Fujishita, T. Mochizuki, W.-S. Ning, and M. Yamada, "Investigations on the structural changes of two Co/SiO2 catalysts by performing Fischer–Tropsch synthesis", *Appl. Catal. A Gen.*, Vol. 252, 2, pp. 251–260, 2003.

92. A. Barbier, A. Tuel, I. Arcon, A. Kodre, and G. A. Martin, "Characterization and Catalytic Behavior of Co/SiO2 Catalysts: Influence of Dispersion in the Fischer–Tropsch Reaction", *J. Catal.*, Vol. 200, 1, pp. 106–116, 2001.

93. J. Yang, E. Z. Tveten, D. Chen, and A. Holmen, "Understanding the effect of cobalt particle size on fischer-tropsch synthesis: Surface species and mechanistic studies by SSITKA and kinetic isotope effect", *Langmuir*, Vol. 26, 21, pp. 16558–16567, 2010.

94. A. M. Saib, A. Borgna, J. van de Loosdrecht, P. J. van Berge, and J. W. Niemantsverdriet, "XANES study of the susceptibility of nano-sized cobalt crystallites to oxidation during realistic Fischer–Tropsch synthesis", *Appl. Catal. A Gen.*, Vol. 312, pp. 12–19, 2006.

95. M. Rønning *et al.*, "Combined XRD and XANES studies of a Re-promoted Co/γ-Al2O3 catalyst at Fischer–Tropsch synthesis conditions", *Catal. Today*, Vol. 155, 3–4, pp. 289–295, 2010.

96. J. P. den Breejen, J. R. A. Sietsma, H. Friedrich, J. H. Bitter, and K. P. de Jong, "Design of supported cobalt catalysts with maximum activity for the Fischer–Tropsch synthesis", *J. Catal.*, Vol. 270, 1, pp. 146–152, 2010.

97. Z. Yan, Z. Wang, D. B. Bukur, and D. W. Goodman, "Fischer–Tropsch synthesis on a model Co/SiO2 catalyst", *J. Catal.*, Vol. 268, 2, pp. 196–200, 2009.

98. D. J. Moodley, J. van de Loosdrecht, A. M. Saib, M. J. Overett, A. K. Datye, and J. W. Niemantsverdriet, "Carbon deposition as a deactivation mechanism of cobalt-based Fischer–Tropsch synthesis catalysts under realistic conditions", *Appl. Catal. A Gen.*, Vol. 354, 1–2, pp. 102–110, 2009.

99. C. H. Bartholomew and R. M. Bowman, "Sulfur poisoning of cobalt and iron fischer-tropsch catalysts", *Appl. Catal.*, Vol. 15, 1, pp. 59–67, 1985.

100. Y. Liu and P. Wynblatt, "Segregation to the (100) surface of dilute Cu–Ag alloys", *J. Vac. Sci. Technol. A Vacuum, Surfaces, Film.*, Vol. 12, 1, pp. 255–257, 1994.

101. R. J. Madon and H. Seaw, "Effect of Sulfur on the Fischer-Tropsch Synthesis", *Catal. Rev.*, Vol. 15, 1, pp. 69–106, 1977.

102. C. H. Bartholomew, "Mechanisms of catalyst deactivation", *Appl. Catal. A Gen.*, Vol. 212, 1–2, pp. 17–60, 2001.

103. S. C. Leviness, C. J. Mart, W. C. Behrmann, S. J. Hsia, and D. R. Nesroka, "Slurry hydrocarbon synthesis process with increased catalyst life", WO1998050487A1, 1998.

104. I. M. Ciobîcă, R. A. van Santen, P. J. van Berge, and J. van de Loosdrecht, "Adsorbate induced reconstruction of cobalt surfaces", *Surf. Sci.*, Vol. 602, 1, pp. 17–27, 2008.

105. P. C. Thüne *et al.*, "Studying Fischer–Tropsch catalysts using transmission electron microscopy and model systems of nanoparticles on planar supports", *Catal. Sci. Technol.*, Vol. 1, 5, p. 689, 2011.

106. J. Lahtinen, J. Vaari, and K. Kauraala, "Adsorption and structure dependent desorption of CO on Co(0001)", *Surf. Sci.*, Vol. 418, 3, pp. 502–510, 1998.

107. K. M. E. Habermehl-Cwirzen, K. Kauraala, and J. Lahtinen, "Hydrogen on Cobalt: The Effects of Carbon Monoxide and Sulphur Additives on the D2/Co(0001) System", *Phys. Scr.*, p. 77, 2004.

108. K. A. Prior, K. Schwaha, and R. M. Lambert, "Surface chemistry of the non-basal planes of cobalt: The structure, stability, and reactivity of Co(10$\bar{1}$2)-CO", *Surf. Sci.*, Vol. 77, 2, pp. 193–208, 1978.

109. J. J. C. Geerlings, M. C. Zonnevylle, and C. P. M. de Groot, "Structure sensitivity of the Fischer-Tropsch reaction on cobalt single crystals", *Surf. Sci.*, Vol. 241, 3, pp. 315–324, 1991.

110. H. Papp, "Chemisorption and reactivity of carbon monoxide on a Co(11$\bar{2}$0) single crystal surface; Studied by LEED, UPS, EELS, AES and work function measurements", *Surf. Sci.*, Vol. 149, 2–3, pp. 460–470, 1985.

111. T. Nowitzki, H. Borchert, B. Jürgens, T. Risse, V. Zielasek, and M. Bäumer, "UHV Studies of Methanol Decomposition on Mono- and Bimetallic CoPd Nanoparticles Supported on Thin Alumina Films", *ChemPhysChem*, Vol. 9, 5, pp. 729–739, 2008.

112. C. J. Weststrate, H. J. Gericke, M. W. G. M. Verhoeven, I. M. Ciobîcă, A. M. Saib, and J. W. (Hans) Niemantsverdriet, "Ethanol Decomposition on Co(0001): C−O Bond Scission on a Close-Packed Cobalt Surface", *J. Phys. Chem. Lett.*, Vol. 1, 12, pp. 1767–1770, 2010.

113. F. Steinbach, J. Kiss, and R. Krall, "Identification and stability of CH3, CH2, and CH species on Co and Ni surfaces, a Pes investigation", *Surf. Sci.*, Vol. 157, 2–3, pp. 401–412, 1985.

114. R. A. van Santen, M. Neurock, and S. G. Shetty, "Reactivity Theory of Transition-Metal Surfaces: A Brønsted−Evans−Polanyi Linear Activation Energy−Free-Energy Analysis", *Chem. Rev.*, Vol. 110, 4, pp. 2005–2048, 2010.

115. B. Hammer and J. K. Nørskov, "Theoretical surface science and catalysis—calculations and concepts", *Adv. Catal.*, Vol. 45, pp. 71–129, 2000.

116. T. C. Bromfield, D. Curulla Ferré, and J. W. Niemantsverdriet, "A DFT Study of the Adsorption and Dissociation of CO on Fe(100): Influence of Surface Coverage on the Nature of Accessible Adsorption States", *ChemPhysChem*, Vol. 6, 2, pp. 254–260, 2005.

117. D. Curulla-Ferré, A. Govender, T. C. Bromfield, and J. W. Niemantsverdriet, "A DFT study of the adsorption and dissociation of CO on sulfur-precovered Fe(100)", *J. Phys. Chem. B*, Vol. 110, 28, pp. 13897–13904, 2006.

118. D. W. Moon *et al.*, "A tilted precursor for CO dissociation on the Fe(100) surface", *Surf. Sci.*, Vol. 180, 1, pp. L123–L128, 1987.

119. M. Ojeda, R. Nabar, A. U. Nilekar, A. Ishikawa, M. Mavrikakis, and E. Iglesia, "CO activation pathways and the mechanism of Fischer–Tropsch synthesis", *J. Catal.*, Vol. 272, 2, pp. 287–297, 2010.

120. S. Shetty and R. A. van Santen, "Hydrogen induced CO activation on open Ru and Co surfaces", *Phys. Chem. Chem. Phys.*, Vol. 12, 24, p. 6330, 2010.

121. O. R. Inderwildi, S. J. Jenkins, and D. A. King, "Fischer-Tropsch mechanism revisited: Alternative pathways for the production of higher hydrocarbons from synthesis gas", *J. Phys. Chem. C*, Vol. 112, 5, pp. 1305–1307, 2008.

122. G. Jones, T. Bligaard, F. Abild-Pedersen, and J. K. Nørskov, "Using scaling relations to understand trends in the catalytic activity of transition metals", *J. Phys. Condens. Matter*, Vol. 20, 6, p. 064239, 2008.

123. P. Sabatier, "Hydrogénations et déshydrogénations par catalyse", *Berichte der Dtsch. Chem. Gesellschaft*, Vol. 44, 3, pp. 1984–2001, 1911.

124. I. M. Ciobîcă, G. J. Kramer, Q. Ge, M. Neurock, and R. A. van Santen, "Mechanisms for Chain Growth in Fischer–Tropsch Synthesis over Ru(0001)", *J. Catal.*, Vol. 212, 2, pp. 136–144, 2002.

125. M. Zhuo, K. F. Tan, A. Borgna, and M. Saeys, "Density Functional Theory Study of the CO Insertion Mechanism for Fischer−Tropsch Synthesis over Co Catalysts", *J. Phys. Chem. C*, Vol. 113, 19, pp. 8357–8365, 2009.

126. M. L. Personick and C. A. Mirkin, "Making Sense of the Mayhem behind Shape Control in the Synthesis of Gold Nanoparticles", *J. Am. Chem. Soc.*, Vol. 135, 49, pp. 18238–18247, 2013.

127. Y. Xia, X. Xia, and H.-C. Peng, "Shape-Controlled Synthesis of Colloidal Metal Nanocrystals: Thermodynamic versus Kinetic Products", *J. Am. Chem. Soc.*, Vol. 137, 25, pp. 7947–7966, 2015.

128. L. D. Marks and L. Peng, "Nanoparticle shape, thermodynamics and kinetics", *J. Phys. Condens. Matter*, Vol. 28, 5, p. 053001, 2016.

129. Y. Wang, J. He, C. Liu, W. H. Chong, and H. Chen, "Thermodynamics versus Kinetics in Nanosynthesis", *Angew. Chemie Int. Ed.*, Vol. 54, 7, pp. 2022–2051, 2015.

130. R. Ferrando, J. Jellinek, and R. L. Johnston, "Nanoalloys: From theory to applications of alloy clusters and nanoparticles", *Chemical Reviews*, Vol. 108, 3. American Chemical Society, pp. 845–910, 2008.

131. C. J. DeSantis, R. G. Weiner, A. Radmilovic, M. M. Bower, and S. E. Skrabalak, "Seeding Bimetallic Nanostructures as a New Class of Plasmonic Colloids", *J. Phys. Chem. Lett.*, Vol. 4, 18, pp. 3072–3082, 2013.

132. Q. Li *et al.*, "New Approach to Fully Ordered fct-FePt Nanoparticles for Much Enhanced Electrocatalysis in Acid", *Nano Lett.*, Vol. 15, 4, pp. 2468–2473, 2015.

133. R. Ghosh Chaudhuri and S. Paria, "Core/shell nanoparticles: Classes, properties, synthesis mechanisms, characterization, and applications", *Chemical Reviews*, Vol. 112, 4. American Chemical Society, pp. 2373–2433, 2012.

134. S. E. Skrabalak, L. Au, X. Lu, X. Li, and Y. Xia, "Gold nanocages for cancer detection and treatment", *Nanomedicine*, Vol. 2, 5, pp. 657–668, 2007.

135. X. Yang, M. Yang, B. Pang, M. Vara, and Y. Xia, "Gold Nanomaterials at Work in Biomedicine", *Chem. Rev.*, Vol. 115, 19, pp. 10410–10488, 2015.

136. S. E. Skrabalak *et al.*, "Gold Nanocages: Synthesis, Properties, and Applications", *Acc. Chem. Res.*, Vol. 41, 12, pp. 1587–1595, 2008.

137. J. Zeng, Q. Zhang, J. Chen, and Y. Xia, "A Comparison Study of the Catalytic Properties of Au-Based Nanocages, Nanoboxes, and Nanoparticles", *Nano Lett.*, Vol. 10, 1, pp. 30–35, 2010.

138. K. D. Gilroy, A. Ruditskiy, H. C. Peng, D. Qin, and Y. Xia, "Bimetallic nanocrystals: Syntheses, properties, and applications", *Chem. Rev.*, Vol. 116, 18, pp. 10414–10472, 2016.

139. S. Sun, "Recent Advances in Chemical Synthesis, Self-Assembly, and Applications of FePt Nanoparticles", *Adv. Mater.*, Vol. 18, 4, pp. 393–403, 2006.

140. R. D. Rutledge *et al.*, "Formation of FePt nanoparticles having high coercivity", *J. Am. Chem. Soc.*, Vol. 128, 44, pp. 14210–14211, 2006.

141. V. K. LaMer and R. H. Dinegar, "Theory, Production and Mechanism of Formation of Monodispersed Hydrosols", *J. Am. Chem. Soc.*, Vol. 72, 11, pp. 4847–4854, 1950.

142. X. Xia, Y. Wang, A. Ruditskiy, and Y. Xia, "25th Anniversary Article: Galvanic Replacement: A Simple and Versatile Route to Hollow Nanostructures with Tunable and Well-Controlled Properties", *Adv. Mater.*, Vol. 25, 44, pp. 6313–6333, 2013.

143. Y. Yang, J. Liu, Z. W. Fu, and D. Qin, "Galvanic replacement-free deposition of au on ag for core-shell nanocubes with enhanced chemical stability and SERS activity", *J. Am. Chem. Soc.*, Vol. 136, 23, pp. 8153–8156, 2014.

144. A. A. Balandin, "Modern State of the Multiplet Theor of Heterogeneous Catalysis", *Adv. Catal.*, Vol. 19, pp. 1–210, 1969.

145. K. Kravchyk *et al.*, "Monodisperse and inorganically capped Sn and Sn/SnO2 nanocrystals for high-performance Li-ion battery anodes", *J. Am. Chem. Soc.*, Vol. 135, 11, pp. 4199–4202, 2013.

146. F.-R. Fan *et al.*, "Epitaxial Growth of Heterogeneous Metal Nanocrystals: From Gold Nano-octahedra to Palladium and Silver Nanocubes", *J. Am. Chem. Soc.*, Vol. 130, 22, pp. 6949–6951, 2008.

147. S. Wang, M. He, M. Walter, F. Krumeich, K. V. Kravchyk, and M. V. Kovalenko, "Monodisperse CoSn2 and FeSn2 nanocrystals as high-performance anode materials for lithium-ion batteries", *Nanoscale*, Vol. 10, 15, pp. 6827–6831, 2018.